ΕΘΝΙΚΟ ΜΕΤΣΟΒΙΟ ΠΟΛΥΤΕΧΝΕΙΟ
Σχολή Αγρονόμων & Τοπογράφων Μηχανικών
ΓΕΩΠΛΗΡΟΦΟΡΙΚΗ
ΜΕΤΑΠΤΥΧΙΑΚΟ ΠΡΟΓΡΑΜΜΑ

NATIONAL TECHNICAL UNIVERSITY OF ATHENS
School of Rural & Surveying Engineering
GEOINFORMATICS
POST-GRADUATE PROGRAMME

INVESTIGATION OF REFRACTION CORRECTIONS IN LEVELLING BY USING REPEATABLE SHORT TERM HEIGHT READINGS AND THE DIRECT MEASUREMENT OF THE TEMPERATURE GRADIENT

Anastasios-Grammatas Kampouris

Rural and Surveying Engineer NTUA

Master Thesis

Supervisor:
Evangelia Lambrou
Professor NTUA

Athens October 2018

ΕΘΝΙΚΟ ΜΕΤΣΟΒΙΟ ΠΟΛΥΤΕΧΝΕΙΟ
Σχολή Αγρονόμων & Τοπογράφων Μηχανικών
ΓΕΩΠΛΗΡΟΦΟΡΙΚΗ
ΜΕΤΑΠΤΥΧΙΑΚΟ ΠΡΟΓΡΑΜΜΑ

NATIONAL TECHNICAL UNIVERSITY OF ATHENS
School of Rural & Surveying Engineering
GEOINFORMATICS
POST-GRADUATE PROGRAMME

INVESTIGATION OF REFRACTION CORRECTIONS IN LEVELLING BY USING REPEATABLE SHORT TERM HEIGHT READINGS AND THE DIRECT MEASUREMENT OF THE TEMPERATURE GRADIENT

Master Thesis

of

Anastasios-Grammatas Kampouris

Supervisor:
Evangelia Lambrou
Professor NTUA

Certified and approved by the three-member committee:

(Signature)	*(Signature)*	*(Signature)*
.....	.....	.....
Evangelia Lambrou Professor NTUA	George Pantazis Professor NTUA	Maria Tsakiri Professor NTUA

Athens October 2018

(Signature)

.....

ANASTASIOS-GRAMMATAS KAMPOURIS
Rural and Surveying Engineer NTUA
MSc Geoinformatics NTUA

ACKNOWLEDGEMENTS

After the elaboration of the present master thesis I would like to express my sincere thanks and deep gratitude to my supervisor Mrs. **Evangelia Lambrou** Professor of SRSE NTUA and my advisor Mr. **George Pantazis** Professor of SRSE NTUA. Beside their exceptional character, will and thoroughness they have always been resourceful, persistence and solution oriented to all the upcoming technical and theoretical difficulties of such a demanding topic and interdisciplinary procedure.

I would also like to thank Dr. **Konstantinos Nikolitsas** Rural and Surveying Engineer NTUA and post-doctoral fellow researcher at CERN for his outstanding scientific, technical and computational advices. Moreover my sincere thanks and appreciation go to the following, where without their assistance and support the final outcome of this thesis would not have been the same:

- Mr. **Jordan Galanis** Rural and Surveying Engineer and Special Technical Laboratory Staff of SRSE NTUA for the provision of the meteorological data as they were acquired by the meteorological station of SRSE.
- Dr. **Maria Karoglou** Chemical Engineer and Special Laboratory Teaching Staff of SChE NTUA and Mr. **Asimakopoulos Makis** Civil Engineer and Special Laboratory Teaching Staff of SCE NTUA for their technical support, advices and assistance regarding the air temperature sensor nodes.
- Mr. **Ioannis Gonos** Associate Professor of SECE NTUA and Mrs. **Nikoleta Ilia** Mechanical Engineer and Special Laboratory Teaching Staff of SECE NTUA for the demonstration and provision of the climate chamber device at the High Voltage laboratory of NTUA.

Finally I would like to express my deepest gratitude and thanks to my family and to my partner, as I am really grateful for their constant encouragement, motivation and patience throughout the course of my under and post-graduate studies. Lastly I want to thank all my close friends as well as my fellow students of the postgraduate program Geoinformatics.

TABLE OF CONTENTS

FIGURES

TABLES

LIST OF SYMBOLS

$\frac{dP}{dz}$	The vertical gradient of atmospheric pressure
$\frac{dT}{dz}$	The vertical temperature gradient
$\frac{de}{dz}$	The vertical gradient of water vapor pressure
$\frac{dn}{dz}$	The vertical gradient of the refraction index
a, b, c, f, g	The parameters of the temperature height functions
c	Velocity of light in vacuum
C_R	Vertical correction due to refraction
d	The change of the refractive index for change of 1°C in temperature
e	Water vapor pressure
f	The frequency of an electromagnetic wave
g	The gravitational acceleration
k	Geodetic refraction coefficient
M	The specific gas constant for dry air
n	Refractive index of a medium
N	Refractivity
n_0	Phase refractive index
N_0	The phase refractivity
N_{gr}	Group refractivity
P	Atmospheric pressure
R	The mean earth's radius
r	The radius of a curved light path due to refraction
s	The horizontal sighting distance
t	Temperature in Celsius
T	Temperature in Kelvin
z	The local vertical height above ground

α	The collimation error (sub-chapter 4.1)
α	The ground slope (sub-chapter 2.7)
α	The thermal expansion of air (sub-chapter 2.4)
β	The inclination angle of a sighting line
δ	The vertical refraction angle of a sighting line
θ	The angle between the normal of two mediums and a light ray
θ_c	The critical angle of an incident light ray
λ	The wavelength of an electromagnetic wave
ρ	The density of atmospheric air

ABBREVIATIONS

AEC	Architecture Engineering and Construction industry
ASTM	American Society for Testing and Material
ATR	Automatic Target Recognition
BIPM	Bureau International des Poids et Mesures/International Bureau of Weights and Measures
CCD	Charged Coupled Device
CERN	Conseil Européen pour la Recherche Nucléaire/ European Organization for Nuclear Research
DIN	Deutsches Institut für Normung/German Institute for Standardization
EDM	Electronic Distance Measurement
EURAMET	European Association of National Metrology Institutes
FFT	Fast Fourier Transform
GSI	The Leica Geo Serial Interface
IAG	International Association of Geodesy
IEC	International Electrotechnical Commission
ISO	International Organization for Standardization
ITS-90	International Temperature Scale of 1990
IUGG	The International Union of Geodesy and Geophysics
LHC	Large Hadron Collider
NATA	National Association of Testing Authorities
NIST	National Institute of Standards and Technology
NTUA	National Technical University of Athens
SCE	School of Civil Engineering
SChE	School of Chemical Engineering
SECE	School of Electrical and Computer Engineering
SRSE	School of Rural and Surveying Engineering

TC	Thermocouples
WSDA	Wireless Sensor Data Aggregator

ABSTRACT

The demand of high accuracy geodetic measurements for the needs of engineering, deformation and monitoring surveying is nowadays heightened. The intense technological improvement and development of geodetic instrumentation has broadened the capabilities and prospects in the applications of the surveying engineer.

Despite the fact of technological advantages the accuracy of engineering and geodetic type measurements, which are carried out either in the lower atmosphere and close to the ground or indoors and underground, is still limited because of refractive effects. The error of geodetic refraction, which bends the sighting line through any telescope, is in terms influenced by the fluctuations of the meteorological parameters that are causing air density inhomogeneity along the sighting path.

The aim of this master thesis is to address a generally applicable method, regarding as much as the instrumentation configuration and the data acquisition procedure as well as the post-processing computations, in order to compute refraction corrections in spirit levelling measurements. The determination of the refraction corrections is based on the direct measurement of the temperature gradient, which is the major influential factor.

Hence, both indoor and outdoor experimental tests were carried out by implementing a stand-alone set up of a high accuracy digital level and air temperature sensors nodes mounted on the barcoded invar staff. Thus, the additional time series were generated, containing repeatable short term measurements of height readings, air temperatures at certain heights and atmospheric pressure for a time period of several days and a time interval of 5 minutes.

The present master thesis is consisted of and summarized by the following 5 chapters:

- **The first chapter** introduces the effect of geodetic refraction and explains the different terminologies of the refraction among the surveyor's practices. Moreover there is a briefing of the existing refraction correction methods while the goal of this thesis is highlighted.
- **The second chapter** includes a thorough theoretical overview of the geodetic refraction starting from the Fermat's principle and Snell's law and leading to the equation of the local geodetic refraction coefficient k. Subsequently there is an analysis of the refraction correction by using the direct measurement of the temperature gradient and the corresponding temperature height functions. Lastly there is a detailed demonstration of the amplitudes of the temperature gradient and the geodetic refraction coefficient k with regard to past studies results.
- **The third chapter** presents the air temperature sensors nodes as well as the meteorological instrumentation. Additionally a calibration procedure of the air temperature sensors is being displayed by using a climate chamber device and

linear modeling in order to adjust the air temperature measurements to the same reference scale.

- **The fourth chapter** demonstrates analytically both the indoor and the outdoor experimental tests. Initially starts with the presentation of the geodetic instrumentation and the stand-alone set up and continues with the thorough illustration of the acquired datasets. Thereafter the evaluation of the temperature height functions curve fitting is introduced as well as the computations of the temperature gradient. In the end the calculated refraction corrections results are being illustrated.
- **The fifth chapter** consists of the final conclusions and deductions of the overall process and highlights proposals and recommendations that are in the need of further investigation.

In conclusion the calibration procedure of the air temperature sensors managed to improve the temperature readings by adjusting the measurements to the same reference scale. Moreover the dependence of the height readings with respect to their linear relationship of the measured meteorological parameters showed a poor and a moderate correlation with regard to atmospheric pressure and air temperature respectively.

Moreover when the temperature gradient had values greater than the measuring accuracy of air temperature sensors $0.4°C \cdot m^{-1}$ then all the temperature height functions seemed to work properly. Additionally when this value was limited to $0.2°C \cdot m^{-1}$ then the models failed to pass the statistical test of the parameters, or to fit the data, or over-fitted the data, except Huggershoff's model.

Lastly none of the computed refraction corrections managed to contribute to the smoothing of the height readings time series since there is a lot of noise contained therein the data. Nevertheless the signs and the amplitudes of the corrections were in line with the theoretical and past studies values. Thus, the geodetic refraction coefficient k took accepted values from 0 to +2.4 in the outdoor tests and from -1.6 to +3.2 in the indoor tests.

EXTENDED ABSTRACT IN GREEK

Η ζήτηση και η ανάγκη για γεωδαιτικές μετρήσεις υψηλής ακρίβειας και ποιότητας είναι σήμερα αυξημένη όσον αφορά στην παρακολούθηση της κινηματικής συμπεριφοράς και στον προσδιορισμό των παραμορφώσεων φυσικών και τεχνητών κατασκευών. Με τον τρόπο αυτό ενισχύεται η διαδικασία λήψης αποφάσεων για την παρέμβαση και την αποφυγή δυσμενών καταστάσεων και καταστροφών στο δομημένο ανθρωπογενές περιβάλλον.

Σε αυτό το γεγονός έχει συντελέσει η αλματώδης ανάπτυξη της τεχνολογίας και κατά συνέπεια η εξέλιξη του επίγειου, εναέριου και δορυφορικού γεωδαιτικού εξοπλισμού. Στο πλαίσιο αυτό ο Τοπογράφος Μηχανικός κρίνεται ο πλέον καταλληλότερος για την απόκτηση, διαχείριση και επεξεργασία της γεωχωρικής πληροφορίας και την εξαγωγή γεωμετρικών παραγώγων υψηλής αξιοπιστίας. Παράλληλα έχει δημιουργηθεί ένα νέο και ευρύ πεδίο εφαρμογών στο οποίο πρωταγωνιστεί ενώ δεν παρακάμπτεται.

Επιπλέον, όσο η επικινδυνότητα και η διακινδύνευση της εκάστοτε εφαρμογής αυξάνεται, τόσο κρίνεται περισσότερο απαραίτητη η ανάλυση και ο προσδιορισμός όλων των πιθανών πηγών σφαλμάτων που αφορούν στις γεωδαιτικές μετρήσεις. Έτσι, παρά την τεχνολογική εξέλιξη, τα γεωμετρικά παράγωγα ταλανίζονται ακόμα από την εισαγωγή σε αυτά τυχαίων και συστηματικών σφαλμάτων. Μία τέτοια πηγή σφάλματος σχετίζεται με το φαινόμενο της ατμοσφαιρικής διάθλασης.

Το φαινόμενο της διάθλασης είτε καμπυλώνει είτε καθυστερεί τη διάδοση ενός ηλεκτρομαγνητικού κύματος καθώς αυτό ταξιδεύει στα διαφορετικά στρώματα της ατμόσφαιρας, είτε αυτό αφορά σε μία οπτική μέτρηση με τη χρήση τηλεσκοπίου είτε ένα παλμό laser είτε κάποιο άλλο μέρος του ηλεκτρομαγνητικού φάσματος. Η επίδραση αυτή, προκαλείται από τις ανομοιογένειες στην πυκνότητα του ατμοσφαιρικού αέρα κατά τη διαδρομή διάδοσης, στις οποίες οφείλονται κατά συνέπεια οι μεταβολές του συντελεστή διάθλασης στα διαφορετικά στρώματα του μέσου.

Αντίστοιχα οι ανομοιογένειες αυτές, προκαλούνται από τις διακυμάνσεις των μετεωρολογικών παραμέτρων, δηλαδή της θερμοκρασίας, της πίεσης και της πίεσης των υδρατμών, λόγω εποχικών και δυναμικών φαινομένων και τη μηχανική της ατμόσφαιρας. Η "θεραπεία" του σφάλματος της ατμοσφαιρικής διάθλασης σε παρατηρήσεις απασχολεί τους τοπογράφους, τους γεωδαίτες, τους αστρονόμους καθώς και άλλους επαγγελματίες για περισσότερο από έναν αιώνα.

Ο σκοπός της παρούσας μεταπτυχιακής εργασίας αφορά στον προσδιορισμό διορθώσεων λόγω γεωδαιτικής διάθλασης σε ψηφιακές αναγνώσεις σε σταδίες, μέσω της απευθείας μέτρησης της κατακόρυφης θερμοβαθμίδας, η οποία αποτελεί και τον κύριο παράγοντα επιρροής. Για το λόγο αυτό, πραγματοποιήθηκαν πειράματα τόσο σε εσωτερικό όσο και εξωτερικό χώρο, υλοποιώντας ένα διασυνδεδεμένο σύστημα

που εξασφάλιζε την αυτόνομη λειτουργία ενός ψηφιακού χωροβάτη υψηλής ακρίβειας ενώ παράλληλα ειδικοί ασύρματοι ψηφιακοί αισθητήρες θερμοκρασίας τοποθετήθηκαν καθ ύψος, σε διακριτές θέσεις του χωροσταθμικού πήχη τύπου "invar".

Ταυτόχρονα εξασφαλίστηκε η καταγραφή της ατμοσφαιρικής πίεσης αξιοποιώντας τον μετεωρολογικό σταθμό που βρίσκεται τοποθετημένος στη Σχολή Αγρονόμων και Τοπογράφων Μηχανικών. Έτσι, δημιουργήθηκαν οι αντίστοιχες χρονοσειρές μετρήσεων, οι οποίες συμπεριλάμβαναν αναγνώσεις ύψους, θερμοκρασίες καθ ύψος της σταδίας και την ατμοσφαιρική πίεση, για περίοδο μερικών ημερών και χρονικό διάστημα 5 λεπτών μεταξύ των επαναλαμβανόμενων μετρήσεων.

Η παρούσα μεταπτυχιακή εργασία αποτελείται από τα εξής ακόλουθα 5 κεφάλαια:

- **Το πρώτο κεφάλαιο** παρουσιάζει αρχικά την έννοια της γεωδαιτικής διάθλασης και στη συνέχεια το διαχωρισμό μεταξύ αστρονομικής και επίγειας διάθλασης, όταν ο παρατηρητής είναι εντός της ατμόσφαιρας και ο στόχος αποτελεί ένα ουράνιο σώμα και αντίστοιχα όταν παρατηρητής και στόχος βρίσκονται εντός της γήινης ατμόσφαιρας.
  Ο όρος της γεωδαιτικής διάθλασης χρησιμοποιείται για παρατηρήσεις που διεξάγονται στα χαμηλά στρώματα της ατμόσφαιρας και κοντά στη φυσική γήινη επιφάνεια και διαχωρίζεται σε οριζόντια και κατακόρυφη. Ταυτίζεται συνήθως με αυτόν της κατακόρυφης από την ακαδημαϊκή κοινότητα και τη βιβλιογραφία, αφού η οριζόντια είναι ιδιαίτερα μικρή σε μέγεθος και θεωρείται αμελητέα.
  Στη συνέχεια, πραγματοποιείται μία σύντομη αναφορά σε όλες τις υπάρχουσες μεθόδους με τις οποίες υπολογίζονται διορθώσεις λόγω γεωδαιτικής διάθλασης ή ο συντελεστής γεωδαιτικής διάθλασης k, οι οποίες επιγραμματικά είναι οι εξής:
  - Η μέθοδος των αμοιβαίων και ταυτόχρονων παρατηρήσεων ζενίθιων γωνιών καθώς και άλλες συμμετρικές διατάξεις παρατηρήσεων.
  - Η μέθοδος της θερμοβαθμίδας ή αλλιώς η μετεωρολογική μέθοδος.
  - Η μέθοδος της τυρβώδης ατμοσφαιρικής ροής και της ανοδικής θερμικής ρευστότητας.
  - Η μέθοδος του διπλού μήκους κύματος.
  - Η μέθοδος της στατιστικής ανάλυσης μέσω της συνόρθωσης δικτύων.

  Τέλος παρουσιάζεται ο στόχος και το αντικείμενο της εργασίας ο οποίος αναφέρεται στην αναζήτηση μίας γενικά εφαρμόσιμης μεθόδου τόσο κατά τη διαμόρφωση και χρήση του εξοπλισμού, δηλαδή τη φάση της απόκτησης των δεδομένων, όσο και κατά τη φάση της επεξεργασία τους για τον υπολογισμό διορθώσεων.
- **Το δεύτερο κεφάλαιο** περιλαμβάνει αναλυτικά το θεωρητικό υπόβαθρο στο οποίο στηρίζεται ο ορισμός της γεωδαιτικής διάθλασης. Αρχικά παρουσιάζονται η αρχή του ελαχίστου χρόνου του Fermat και ο νόμος του Snell. Στη συνέχεια ορίζεται σχηματικά και ποσοτικά η γωνία διάθλασης δ, η οποία είναι η γωνία μεταξύ της χορδής και της εφαπτόμενης της καμπυλωμένης δέσμης, και ο συντελεστής γεωδαιτικής διάθλασης k, ως ο

λόγος της μέσης ακτίνας καμπυλότητας της γης προς την ακτίνα καμπυλότητας της δέσμης.

Ακολούθως παρουσιάζονται οι βασικές μετεωρολογικές παράμετροι της τροπόσφαιρας καθώς και η σχέση τους με το συντελεστή διάθλασης n και της διαθλασιμότητας N καθώς και της κατακόρυφης βαθμίδας του συντελεστή διάθλασης (dn/dz). Από αυτόν, στη συνέχεια ορίζεται και υπολογίζεται η εξίσωση του τοπικού συντελεστή γεωδαιτικής διάθλασης k σε σχέση με τις μετεωρολογικές παραμέτρους και ο τρόπος χρήσης της.

Ακολούθως προσδιορίζεται αναλυτικά ο τρόπος υπολογισμού των διορθώσεων λόγω διάθλασης όπως αρχικά παρουσιάστηκε από τον Φιλανδό Γεωδαίτη "Kukkamaki". Ο οποίος αφού μελέτησε την ατμοσφαιρική φυσική κατασκεύασε μια εκθετική εξίσωση μεταξύ της θερμοκρασίας και του κατακόρυφου ύψους. Έτσι, η τελική διόρθωση δίνεται από ένα ορισμένο ολοκλήρωμα της διαφοράς θερμοκρασιών από το ύψος του οργάνου έως το ύψος της ανάγνωσης. Η μέθοδος που ανάπτυξε βασίζεται στις ακόλουθες υποθέσεις:

- Η επίδραση της υγρασίας θεωρείται αμελητέα για τη διάδοση κυμάτων που εμπίπτουν στο οπτικό φάσμα.
- Η διαστρωμάτωση του αέρα θεωρείται πως πραγματοποιείται σε ισόθερμα επίπεδα παράλληλα στο έδαφος.
- Η κλίση του εδάφους μεταξύ χωροβάτη και σταδίας θεωρείται ενιαία.

Μία αντίστοιχη προσέγγιση δίνεται από την επίλυση της εικονικής εξίσωσης του Moritz ενώ ο "Remmer" προσδιόρισε έπειτα από στατιστικές επιλύσεις τη διόρθωση για μια ενδιάμεση στάση του χωροβάτη ως προς τη 2^{η} και 4^{η} παράγωγο της κατακόρυφης θερμοβαθμίδας. Επιπλέον παρουσιάζονται και άλλα μοντέλα της κατακόρυφης θερμοβαθμίδας που συναντούνται στη βιβλιογραφία. Τέλος δίνονται οι τιμές του συντελεστή γεωδαιτικής διάθλασης k και της θερμοβαθμίδας όπως υπολογίστηκαν από παλαιότερες έρευνες με το k να λαμβάνει τιμές από -4 έως +16.

- **Το τρίτο κεφάλαιο** εμπεριέχει την παρουσίαση των τεχνικών χαρακτηριστικών των αισθητήρων θερμοκρασίας καθώς και του μετεωρολογικού εξοπλισμού. Παράλληλα παρουσιάζεται μια διαδικασία βαθμονόμησης των αισθητήρων θερμοκρασίας χρησιμοποιώντας μια συσκευή κλιματικού θαλάμου.

  Σύμφωνα με την εφαρμοζόμενη μεθοδολογία, οι αισθητήρες τοποθετήθηκαν στον κλιματικό θάλαμο ενώ τους ασκήθηκαν συγκεκριμένα φορτία θερμοκρασίας και σχετικής υγρασίας ώστε να προσομοιάζουν τις πραγματικές συνθήκες λειτουργίας τους. Στη συνέχεια προσδιορίστηκε το γραμμικό μοντέλο των διορθώσεων στις μετρήσεις του κάθε αισθητήρα, σε σχέση με τις μετρήσεις του ενσωματωμένου θερμομέτρου του θαλάμου με τη μέθοδο των ελαχίστων τετραγώνων. Με τη διαδικασία αυτή οι αναγνώσεις της θερμοκρασίας των αισθητήρων βελτιώνονται διότι ανάγονται στην ίδια κλίμακα αναφοράς ενώ προσεγγίζεται η αβεβαιότητα μέτρησης τους, η οποία είναι της τάξης ±0.1°C.
- **Το τέταρτο κεφάλαιο** παρουσιάζει αναλυτικά τη διαδικασία των πειραμάτων και των αποτελεσμάτων. Αρχικά προβάλλεται ο γεωδαιτικός εξοπλισμός που χρησιμοποιήθηκε, ο οποίος αποτελείται από το ψηφιακό χωροβάτη υψηλής ακρίβειας Leica DNA03 και τις αντίστοιχες σταδίες γραμμικού κώδικα τύπου "invar". Επιπλέον γίνεται αναφορά στον τρόπο επίτευξης της αυτόνομης

λειτουργίας μέτρησης του χωροβάτη αξιοποιώντας έναν καλώδιο ύψιλον και ένα λογισμικού σειριακής σύνδεσης RS232.

Στο επόμενο υποκεφάλαιο παραθέτονται όλα τα δεδομένα των τεσσάρων πειραματικών διαδικασιών, δηλαδή των 2 εσωτερικών πειραμάτων σε αποστάσεις σκόπευσης 25m και 50m και των 2 εξωτερικών σε απόσταση σκόπευσης 40m, όπως αυτά προέκυψαν κατά τη φάση συλλογής. Αυτό που αξίζει να τονιστεί σε αυτό το σημείο είναι πως υπολογίστηκαν μετριοπαθής θετικές γραμμικές συσχετίσεις μεταξύ της θερμοκρασίας και της ανάγνωσης ύψους.

Στη συνέχεια παρουσιάζονται τα αποτελέσματα από την προσαρμογή των 5 επιλεγμένων μοντέλων της θερμοβαθμίδας, τα οποία αφορούν 5 διαφορετικές καμπύλες που συνδέουν τη θερμοκρασία του αέρα σε σχέση με το τοπικό κατακόρυφο ύψος, στα δεδομένα της θερμοκρασίας καθώς και ο υπολογισμός του μεγέθους της. Έτσι, όταν η θερμοβαθμίδα λαμβάνει τιμές μεγαλύτερες από την ακρίβεια μέτρησης των αισθητήρων, δηλαδή μια τάξη μεγέθους $\approx 0.4°C \cdot m^{-1}$, τότε όλα τα μοντέλα δείχνουν να λειτουργούν σωστά.

Αντίθετα όταν αυτή η τιμή μειώνεται και λαμβάνει τιμές κοντά στην ακρίβεια μέτρησής τους, τότε τα μοντέλα είτε αποτυγχάνουν να προσαρμοστούν στα δεδομένα, είτε οι παράμετροί τους είναι στατιστικά μη σημαντικοί, είτε υπερπροσαρμόζονται στα δεδομένα (μοντέλο Reissmann2). Το μοντέλο που κατάφερε κατά πλειοψηφία να επιτύχει στο στατιστικό έλεγχο των παραμέτρων του για επίπεδο εμπιστοσύνης 68% και να δώσει ρεαλιστικά αποτελέσματα σε σχέση με το a-posteri ori τυπικό σφάλμα ήταν αυτό του "Huggershoff".

Τέλος προβάλλονται τα αποτελέσματα από τους υπολογισμούς των διορθώσεων στην ανάγνωση ύψους λόγω της διάθλασης καθώς και η ποσοτικοποίηση και μετάφρασή τους σε συντελεστές γεωδαιτικής διάθλασης k. Από αυτά σε κανένα από τα πειράματα και τα μοντέλα δεν φαίνεται να επιτυγχάνεται η γραμμική εξομάλυνση της χρονοσειράς των αναγνώσεων ύψους, γεγονός που οφείλεται στο θόρυβο που εμπεριέχεται στα δεδομένα και στην υψηλή αβεβαιότητα μέτρησης τόσο του χωροβάτη όσο και των αισθητήρων.

Παρόλα αυτά τόσο τα πρόσημα των διορθώσεων και του συντελεστή k όσο και το εύρος των τιμών τους συμφωνεί με τη θεωρητική ανάλυση και τη βιβλιογραφία.. Επίσης υπολογίστηκε ο τοπικός συντελεστής γεωδαιτικής διάθλασης k, όπου οι τιμές ήταν σε συμφωνία με μια μικρή θετική συστηματική διαφορά που οφείλεται στην ενσωμάτωση της βαθμίδας της ατμοσφαιρικής πίεσης. Το πιο θετικό γεγονός αφορά στο δεύτερο εξωτερικό πείραμα, όπου οι διορθώσεις δείχνουν να αντισταθμίζουν την τάση και το εύρος των αναγνώσεων.

- **Το πέμπτο κεφάλαιο** προβάλλει όλα τα συμπεράσματα που προέκυψαν από την υλοποίηση της παρούσας μεταπτυχιακής εργασίας και τη διεξαγωγή των πειραμάτων καθώς και προτάσεις οι οποίες χρήζουν περεταίρω μελλοντικής έρευνας. Έτσι, η εξέλιξη του εξοπλισμού θερμομέτρησης διευκολύνει και βελτιστοποιεί τη φάση συλλογής των δεδομένων, ενώ η βαθμονόμηση των αισθητήρων βελτιώνει τις μετρήσεις. Επιπλέον τα μοντέλα θερμοκρασίας τοπικού ύψους είναι ευαίσθητα σε σχέση με την ακρίβεια μέτρησης των αισθητήρων και κατά συνέπεια του εύρους των τιμών της θερμοβαθμίδας.

  Για το λόγο αυτό προτείνεται μια σε βάθος ανάλυση της αβεβαιότητας των διαφόρων παραμέτρων που μετρούνται καθώς και η εκτέλεση αντίστοιχων

πειραμάτων με υψηλότερη ακρίβεια μέτρησης της θερμοκρασίας. Επίσης προτείνεται να τοποθετηθούν αισθητήρες θερμοκρασίας σε περισσότερα οριζόντια τμήματα της σκοπευτικής γραμμής και όχι μόνο στη σταδία. Με τον τρόπο αυτό θα συμπεριληφθούν οι διακυμάνσεις κατά μήκος της διαδρομής διάδοσης της οπτικής δέσμης.

Συμπερασματικά, παρόλο που η γραμμική εξομάλυνση των χρονοσειρών των ψηφιακών αναγνώσεων ύψους δεν επιτεύχθηκε, τα πρόσημα των διορθώσεων και τα εύρη των τιμών τους ήταν τα αναμενόμενα. Έτσι ο συντελεστής γεωδαιτικής διάθλασης k που υπολογίστηκε λαμβάνει αποδεκτές τιμές από 0 έως +2.4 στα εξωτερικά πειράματα και από -1.6 έως +3.2 στα εσωτερικά πειράματα.

Τέλος, ενώ η τεχνολογία των αισθητήρων θερμοκρασίας βελτιστοποιεί τη φάση συλλογής των δεδομένων, αυτό που παραμένει ένα κρίσιμο ζήτημα αφορά στην αβεβαιότητα μέτρησης και στην ευαισθησία τους στις κλιματικές συνθήκες. Έτσι, δημιουργούνται περιορισμοί τόσο στους τελικούς υπολογισμούς όσο και στον τρόπο χρήσης τους σε σχέση με το περιβάλλον που χωροθετούνται και τις μετεωρολογικές συνθήκες που επικρατούν σε αυτό.

INTRODUCTION

Today's era is characterized by the extreme technological evolution and the rapid information propagation while the impacts of the climate change have become evident. The Internet of Things, big data analysis and artificial intelligence innovations appear more on everyday life while a lot of social and economic activities have migrated online. Additionally geoinformatics have come to play an important role in the solution of modern urban, rural and environmental problems and the meeting of current human needs.

Furthermore the Architecture Engineering and Construction (AEC) industry is increasingly oriented to the sustainability, monitoring and maintenance of the existing structures, projects and infrastructures. This fact reasonably takes place in order to facilitate the decision making procedures and the risk management situations and as well as to contribute to the avoidance of technical failures, construction collapses and disasters with respect to the built environment.

Technical geodesy, industrial geodesy and engineering surveying, as a part of the broadened concept of geoiformatics, provide the only valid and reliable methodologies for the determination of displacements and deformations of natural formations and man-made structures. The uniqueness of deformation and monitoring surveying is that the measurements are correlated and the extracted geometric information in the 3D space, by means of amplitude and direction, is unified in the same reference system and can be statistically tested.

The importance of these geodetic derivatives, especially when the upcoming impacts and risks are increased, is in terms interpreted to high quality and high accuracy measurements. Thus, the thorough investigation of all possible and plausible error sources is a necessary and demanding task to overcome. One of these error sources that have been agonizing geodesists and other practitioners for over a century is detected on the refraction effects.

CHAPTER 1
ABOUT THE GEODETIC REFRACTION

1.1 Generally

The evolution of modern geodetic instrumentation has been significant especially in the past three decades. Initiating with the integration of EDM (Electronic Distance Measurement) and CCD sensors and leading to today's instrumentation, which has become smart, automated and robotic with new capabilities like remote control, motor driven operations and automatic target recognition (ATR).

Moreover there has been a high level of accuracy achieved by using compensator correction techniques and auto calibration processes, while a remarkable reliability has been developed. These new potentials offer a great advantage in a multitude of applications, where terrestrial, airborne and satellite measurements have to be taken place, as well as in multiple fields like geodesy, photogrammetry and remote sensing.

Additionally the need of high accuracy geodetic measurements is now extended and thus the thorough investigation of all possible and plausible error sources is necessary. Though, despite the fact of technological improvement the precision of geodetic measurements and geometric derivatives is still limited mainly due to the unpredictable propagation of electromagnetic waves through the different layers of the earth's atmosphere. In most cases the elimination of these errors is based on techniques of reciprocal neutralization of such effects.

The major cause of these errors are identified and concentrated on the effect of atmospheric refraction, which either deforms or curves the electromagnetic wave path and alternates its velocity. This means that the atmospheric parameters influence curves the path of the sighting line through a telescope.

As it is well known atmospheric refractive effects are caused due to air density fluctuations or otherwise due to inhomogeneity of the propagation medium. The treatment of atmospheric refraction effects has been agonizing geodesists, astronomers and other practitioners for over a century.

1.2 Existing Refraction Correction Methods Review

Atmospheric refraction, as it was aforementioned, is responsible for the curvature and the delay of an electromagnetic wave's propagation path through the atmosphere. This master thesis is focusing on the curvature refractive effects of the lower atmosphere and more specifically for the visible electromagnetic spectrum. So, the curvature of the light path of an optical observation is usually divided in bibliography into two categories.

The first category is addressed by the term of astronomical refraction. This term is used in order to describe the bending of the sighting path, when an astronomical

observation is carried out from the earth's surface to celestial bodies [Young, 2006]. In addition, when both the target and the observer are inside the earth's atmosphere the ray bending effect is described as terrestrial refraction [Brocks, 1939; Hirt et al, 2010; Hübner, 1977].

Moreover if the observations are taken place in the lower atmosphere, meaning close to the ground, then the effect is also called as geodetic refraction [Thomas and Joseph, 1996].

The geodetic refraction is in terms divided into two subcategories:

- The lateral refraction, when the atmospheric refraction affects horizontal angles and directions [Korritke, 1992; Wilhelm, 1994].
- The levelling refraction, when it affects vertical directions.

However, geodetic and levelling refraction are identified as the same since the main amount of the refraction error yields in the vertical dimension.

Subsequently, a brief review of the refraction correction methods on geodetic measurements is presented. All methodologies that address the levelling or the geodetic refraction corrections, aim to the determination either of the refraction angle, meaning the angular deviation, or the linear spread due to refraction at a certain distance. A short resume of the refraction correction methods is the following:

1. The most common method to compute geodetic refraction corrections is the reciprocal and simultaneously zenith observations [Hirt et al., 2010; Mavridis and Papadimitriou, 1973; Tsoulis et al., 2008;]. The geodetic refraction coefficient is computed as a result of this method, and yields true line averages of micrometeorological parameters [Brunner and Kukuvec, 2011]. Other special measuring procedures of mutual or symmetrical observations are based on the same fundamental principles.
2. The measurement of the temperature gradient, which is the major influential parameter of the levelling refraction error, by using air temperature sensors [Gottwald. 1985; Hennes, 1999]. The main assumptions of this method is
    - the constant inclination of the ground below the sight line and
    - the isothermal stratification of the atmospheric air parallel to the ground [Kakkuri, 1984].

    It is also known as a direct meteorological method, which takes into account the measured temperature gradient [Breznikar & Aksamitauskas, 2012; Kharaghani, 1987].

3. Turbulence based methods using the upward sensible heat flux in order to indirectly model the temperature gradient [Brunner & Fraser, 1977; Flach, 2000]. The propagation of the electromagnetic waves is influenced by the turbulence (optical turbulence) of the atmosphere whereas thermally produced

eddies as well as mechanically produced eddies influence the beam [Böckem et al., 2000; Ingensand, 2008]. The turbulence parameters can derive either by measuring the effect of image dancing, using image analysis and a CCD sensor or by the determination of intensity fluctuation of a laser beam using a scintillometer [Weiss, 2002].

4. The dual-wavelength dispersion method, which uses the dispersive property of the atmosphere (meaning the wavelength dependence of the refractive index) in order to determine the angle of refraction. A dispersometer measures the angle difference between two arriving light beams of different wavelengths, which is called the dispersion angle and is approximately proportional to the refraction angle [Böckem et al., 2000; Ingensand, 2008].
5. The last method refers to the statistical analysis of refraction effects in geodetic operations [Breznikar & Aksamitauskas, 2012]. This can be done by the integration of refraction effects into the adjustment of geodetic networks [Remmer, 1980b].

1.3 Master's Thesis Goal and Concept

This master thesis aims to the determination of the refraction corrections through the direct measurement of the temperature gradient, during spirit levelling measurements. The major concept is to develop a generally applicable and easy to use method for the computation of refraction corrections, which can be interpreted as geodetic refraction coefficients k, in high precision geodetic levelling procedures for the purposes of engineering, monitoring and deformation surveying.

For the purpose of this research both indoor and outdoor experiments of repeatable levelling readings were carried out for a time period of several days and a time interval of five minutes, by using a high accuracy digital level and special temperature sensors nodes. Hence the additional time series were generated wherein the hitherto temperature height models were tested and evaluated.

The first goal of this thesis is to address a generalized method in terms of instrumentation configuration, in order to accommodate the data acquisition process of high precision engineering surveying observations.

The second goal is to develop and assess the post processing computations in order to determine refraction corrections with a limited number of measured and modeled factors.

Lastly the short term fluctuations of the refraction coefficient k are being investigated.

This is a matter of high significance especially for projects, which require accuracy of some μm and that are being developed either indoor or underground or with stable meteorological conditions, where atmospheric physics and the heat flux effects are not applied and are no consistent.

CHAPTER 2
THEORETICAL OVERVIEW OF GEODETIC REFRACTION

2.1 Fermat's Principle

The main influences on an electromagnetic wave due to refraction are expressed as retarding and bending effects. These two effects of the propagation of an electromagnetic wave through different mediums are based on Fermat's principle from which the Snellius law is derived [Katz et al 2013].

Fermat's principle defines that the travel path (s) taken by an optical ray between two points is always the path that can be traversed in the least time (Δt) [Moritz and Hofmann-Wellenhof, 1993; Schuster, 1904; Torge, 2001], which is the reason why it is also known as the principle of least time (equation 2.1).

$$\Delta t = \int dt = \int \frac{1}{v}\frac{ds}{dt}dt \; = \int \frac{1}{v}ds = min \tag{2.1}$$

As it is well known the velocity of a wave along the electromagnetic spectrum in vacuum equals to c=299792.458 km·s^{-1}, and the frequency (f) is inversely proportional to the wave length (λ) as it is presented in equation 2.2.

$$f = \frac{c}{\lambda} \tag{2.2}$$

Additionally the velocity (v) of an electromagnetic beam through a medium differs and is always smaller than c.

The refractive index (n) of a medium is a dimensionless physical property and is defined as the ratio of the velocity of light in vacuum (c) to the phase velocity of light in the medium (v) (equation 2.3). This presupposes that refraction index in vacuum is unitary and at the same time the minimal, while the wave's propagation velocity is maximized.

$$n = \frac{c}{v} \tag{2.3}$$

Inserting equation (2.3) into (2.1) yields:

$$\Delta t = \int dt = \frac{1}{c}\int \frac{c}{v}\frac{ds}{dt}dt \; = \int \frac{n}{c}ds = \frac{1}{c}\int nds = min \tag{2.4}$$

And by setting $n \cdot ds = \overline{ds}$ then according to eq. 2.4 the optical path can be expressed as a minimum:

$$\bar{s} = \int_0^{\bar{s}} \overline{ds} = \int_0^{\bar{s}} n \cdot ds = min \tag{2.5}$$

Thus, the refraction effect can be expressed by the difference between the optical path (or else the actual path or the electromagnetic path) and the geometric path (or else the straight path or the vacuum path) is given by:

$$\bar{s} - s = \int_0^{\bar{s}} n \cdot ds - \int_0^{s} ds = \int_0^{s} (n-1) \cdot ds + \left[\int_0^{\bar{s}} n \cdot ds - \int_0^{s} n \cdot ds \right] \quad (2.6)$$

Hence, the principle of least time shows that the optical path is different from the geometrical path and the knowledge of the refractive index along it is required in order to compute retarding and bending effects.

The first term of equation 2.6, which includes the parenthesis, corresponds to the difference of the refracted and the linear optical ray, known as bending and the second term in the brackets corresponds to the excess of the optical length due to the atmospheric delay also known as retarding [Janes et al,1991; Mendes and Pavlis, 2002; Torge, 2001].

2.2 Snell's Law

Snell's law of refraction is a widely accepted formula that describes the relationship between the angle of incidence (θ_1) and angle of refraction (θ_2) when a light ray, or namely an electromagnetic wave, passes through the boundary of different isotropic mediums.

Snellius law states that the ratio of the sines of the angles is equivalent to the ratio of the phase velocities and reverse equivalent to the ratio of the refractive indexes (eq. 2.7). Alternatively the refraction law states that the multiplication of the refractive index and the angle of incidence is constant (eq. 2.8).

$$\frac{\sin(\theta_1)}{\sin(\theta_2)} = \frac{v_1}{v_2} = \frac{n_2}{n_1} \quad (2.7)$$

$$n_i \cdot \sin(\theta_i) = constant \quad (2.8)$$

Thus when an incident light ray travels from a medium with a lower refractive index to a medium with a higher refractive index ($n_1 < n_2$, $v_1 > v_2$,) the refracted light ray is bended towards the normal ($\theta_1 > \theta_2$,), as it is presented in figure 2.1 a.

On the contrary when an incident light ray travels from a medium with a higher refractive index to a medium with a lower refractive index ($n_1 > n_2$, $v_1 < v_2$,) the refracted light ray is bended away from the normal ($\theta_1 < \theta_2$,); as it is presented in figure 2.1 b.

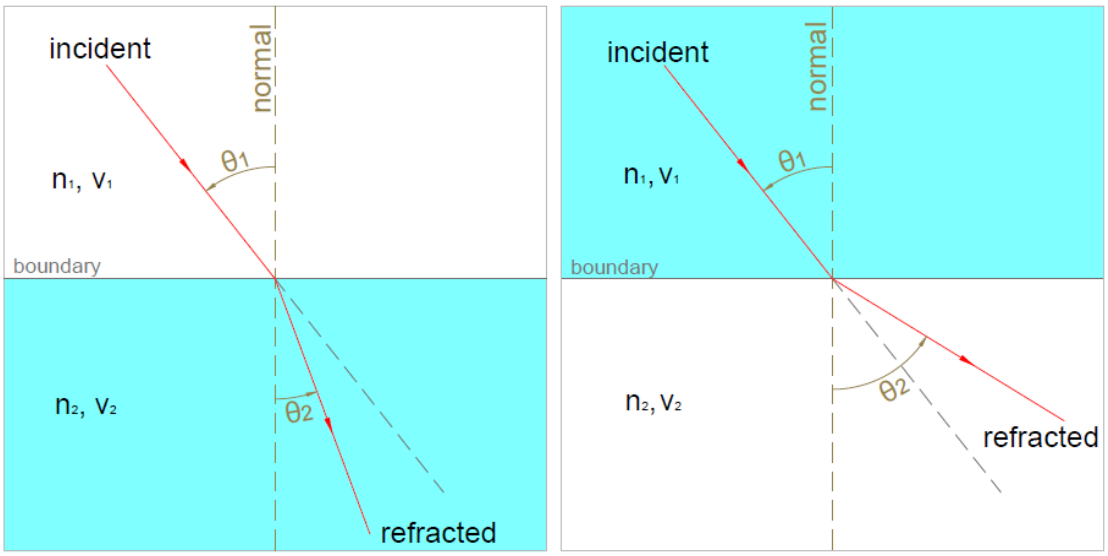

(a) $n_1 < n_2$ (b) $n_1 > n_2$

Figure 2.1 Refraction of a light ray that passes through the boundary between mediums of different refraction indexes, (a) when $n_1 < n_2$ and (b) when $n_1 > n_2$.

2.2.1 Total Internal Reflection

Moreover Snell's law indicates a crucial occasion when light travels from mediums of higher refractive index to a medium of lower refractive index ($n_1 > n_2$). While the incident angle is gradually increasing there is a critical angle (θ_c, eq. 2.9) where the refracted ray is bended parallel to the boundary, or alternatively the angle of the refracted ray is right (so $\sin 90^o = 1$).

Hence, when the angle of the refracted ray becomes greater than the critical angle, then the light is completely reflected by the boundary (figure 2.2). This phenomenon is known as total internal reflection.

$$\sin(\theta_c) = \frac{n_2}{n_1} \tag{2.9}$$

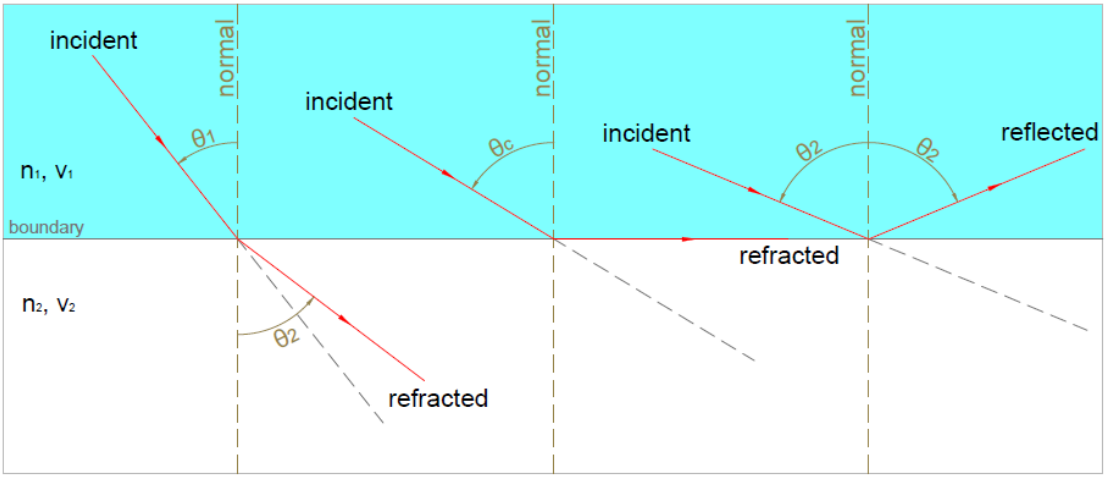

Figure 2.2 The phenomenon of total internal reflection where $\theta_1 < \theta c < \theta_2$.

2.3 The Definition of the Geodetic Refraction Coefficient k

Assuming that the atmospheric air is stratified horizontally, in respect to the local vertical (z), in layers of varying refractive indexes then the refraction effect on wave's curvature (1/r) can be estimated by using Snell's law [Torge, 2001]. Thus, by differentiating equation (2.8) with respect to the local vertical z and considering the geometric relations presented in figure (2.3) then the curvature of the bended ray is obtained:

$$\frac{\partial}{\partial\theta}\cdot\frac{d\theta}{dz}+\frac{\partial}{\partial n}\cdot\frac{dn}{dz}=0\rightarrow n\cdot\cos(\theta)\cdot d\theta+\sin(\theta)\cdot dn=0\rightarrow$$
$$d\theta=-\frac{dn\cdot\sin(\theta)}{n\cdot\cos(\theta)}\rightarrow\frac{1}{r}=-\frac{1}{n}\cdot\frac{dn}{dz}\cdot\sin(\theta) \qquad (2.10)$$

Where the curvature of the bended ray is obtained as $\frac{1}{r}=\frac{d\theta}{ds}$ and $\cos(\theta)=\frac{dz}{ds}$.

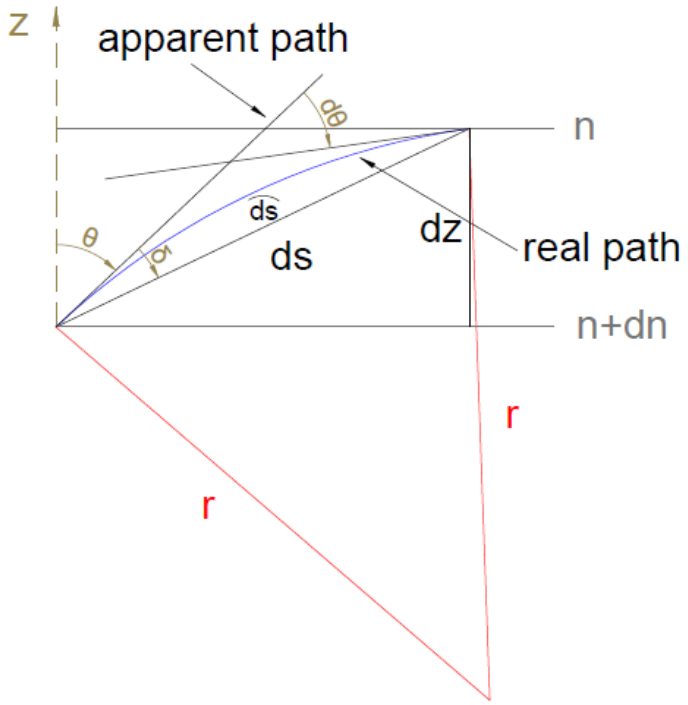

Figure 2.3 Ray bending in atmospheric air.

In most common terrestrial geodetic measurements the refractive index can be assumed as unitary (n≈1) and the incidence angle as right (θ≈90^{o}), which leads to the following relation (eq. 2.11) between the curvature due to refraction and the vertical gradient of the refraction index [Torge, 2001]:

$$\frac{1}{r}=-\frac{dn}{dz} \qquad (2.11)$$

The well-known to geodesists coefficient of refraction k, is defined as the ratio between the Earth's radius (R) to the radius of the curved light path (r) [Brocks, 1950; Hirt et al, 2010; Kahmen and Faig, 1988; Shaw and Smietana,1983; Torge, 2001].

The coefficient of refraction k is a convenient way to represent and quantify the refraction effects in geodesy, even though the refraction influence on the sight line curvature is more complex than a simplified circle's arc. According to equation 2.11 the coefficient of refraction equals to:

$$k = \frac{R}{r} = -R \cdot \frac{dn}{dz} \tag{2.12}$$

Hence, in the simple case the vertical refraction angle δ (figure 2.3 and 2.5), which is the angle between the chord and the tangent of the optical path or else the angle between the apparent and the real position of a target (figure 2.5), along a curved line of sight with length s and by assuming a constant coefficient k along the light path, can be simply obtained as an arc length:

$$\delta = \frac{1}{2} \cdot \frac{s}{r} = \frac{k \cdot s}{2 \cdot R}$$
$$\text{or by substituting equation 2.10} \rightarrow \delta = \frac{d\theta}{2} = -\frac{1}{2 \cdot n} \cdot \frac{dn}{dz} \cdot s \tag{2.13}$$

Additionally the vertical deviation of the light beam due to refraction or the refraction correction (C_R) of a curved light beam from the real vertical position is computed as:

$$C_R = -s \cdot \delta = -\frac{k \cdot s^2}{2 \cdot R} = \frac{1}{2 \cdot n} \cdot \frac{dn}{dz} \cdot s^2 \tag{2.14}$$

The above equations (2.12, 2.13 and 2.14) show that the refraction correction, which is the distance between the real vertical position and the apparent position, is proportional to the square of the sight length s (figure 2.4).

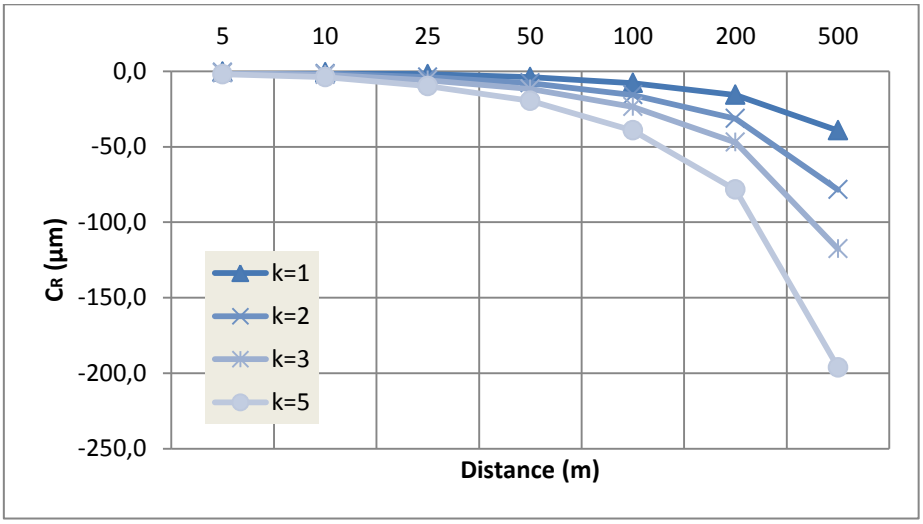

Figure 2.4 Refraction corrections along distances for certain coefficients k.

What needs to be mentioned is that equations 2.13 and 2.14 are only valid under the assumptions that:

- the stratified layers are perpendicular to the local vertical and
- the vertical gradient of the refractive index is constant.

Nevertheless these assumptions cannot be precisely supported in field practice [Flach, 2000]. Otherwise the refractive index gradient should be determined as function of the propagation path which is mainly influenced by the temperature gradient as it is discussed later in this thesis. However these geometrical components are useful for the quantification of refraction influences in applied geodesy [Flach, 2000].

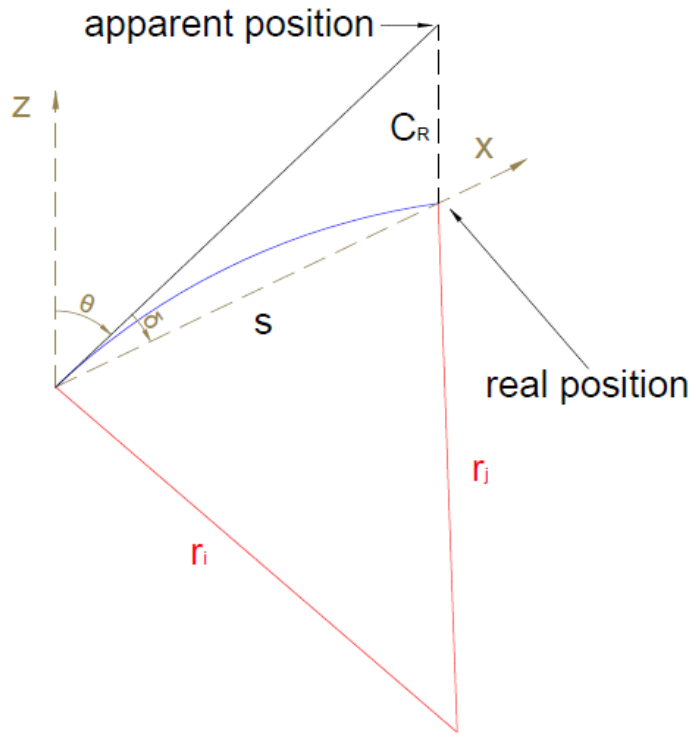

Figure 2.5 Vertical refraction angle and correction due to refraction.

Moreover, the refraction angle can be generated, in terms of the unified theory of geodetic refraction [Heer and Neiemer, 1985], by the eikonal equation for the path of the light wave according to Moritz [Brunner and Angus-Leppan, 1976; Moritz 1962, 1967].

Thus, figure 2.5 states that the vertical refraction angle δ results from integrating the curvature due to refraction (eq. 2.10) and respectively the vertical refraction index gradient, along the path [Torge, 2001]:

$$\delta = \frac{1}{s} \cdot \int_0^s \frac{1}{r} \cdot (s - x) \cdot dx = -\frac{\sin(\theta)}{s} \cdot \int_0^s \frac{1}{n} \cdot \frac{dn}{dz} \cdot (s - x) \cdot dx$$
$$if \;\; \sin(\theta) = 1 \;\; and \;\; \frac{dn}{dz} = const. \;\; then \;\; \rightarrow \delta = -\frac{1}{2 \cdot n} \cdot \frac{dn}{dz} \cdot s \qquad (2.15)$$

Then the refraction correction is simply given by:

$$C_R = -s \cdot \delta = \int_0^s \frac{1}{r} \cdot (s - x) \cdot dx = \sin(\theta) \cdot \int_0^s \frac{1}{n} \cdot \frac{dn}{dz} \cdot (s - x) \cdot dx$$
$$if \;\; \sin(\theta) = 1 \;\; and \;\; \frac{dn}{dz} = const. \;\; then \;\; \rightarrow C_R = \frac{1}{2 \cdot n} \cdot \frac{dn}{dz} \cdot s^2 \tag{2.16}$$

The above equations (2.15 and 2.16) show, that with the corresponding assumptions, the formulae yields the same results as the in the equations 2.13 and 2.14.

2.4 Basic Meteorological Parameters in the Troposphere

The troposphere is the lowest atmospheric layer with a width of about 18km at the equator, where all weather procedures take place. The index of refraction is directly related to the meteorological parameters of temperature, pressure and humidity. It is considered that the troposphere behaves as a dispersive medium regarding visible light and near infrared amplitude of the electromagnetic spectrum [Torge, 2001].

This means that the refraction index n is also dependent on the wavelength, while the wave's frequency remains constant, for certain meteorological conditions, in addition to microwaves. In general the refractive index decreases with height and becomes unitary at a height of 40km [Torge, 2001].

Temperature, pressure and humidity are also strongly related to height as well as latitude, masses distribution, vegetation, topography and local conditions. The alterations of these parameters produce long term as much as short term fluctuations on the refractive index with respect to season and daytime. The short term fluctuations mainly influence the first 30m above the ground [Torge, 2001].

At a large scale examination temperature (T) decreases linearly to altitude, which means that the temperature gradient is negative (equation 2.17) and is also known as the adiabatic temperature gradient. Of course the temperature gradient can be inverted in specific circumstances and locations, close to the ground and during the night.

$$\frac{dT}{dz} = -6.5°K \cdot km^{-1} \tag{2.17}$$

The vertical gradient of atmospheric pressure (P) is also negative and is decreasing exponentially with height. It is approximated as [Bomfort, 1980; Torge, 2001]:

$$\frac{dP}{dz} = -\rho \cdot g = -\frac{g}{M} \cdot \frac{P}{T} = -0.0342 \cdot \frac{P}{T} = -0.12mb \cdot m^{-1} \tag{2.18}$$

Where g is the gravitational acceleration
M is the specific gas constant for dry air and
ρ is the density of atmospheric air at sea level and
the last term is valid at standard air conditions (T=288°K, P=1013mb).

Lastly humidity, which is irregularly distributed and is concentrated in the first few km of the troposphere, is measured in terms of water vapor pressure (e) with a range of 10-20mb close to the ground [Torge, 2001]. The vertical gradient of water vapor pressure has a decreasing tendency with a mean value of:

$$\frac{de}{dz} = -0.0035mb \cdot m^{-1} \tag{2.19}$$

2.5 Definition of the Refraction Index Gradient

In most common atmospheric applications refractivity (N) is frequently used instead of the refractive index (n) and is expressed as $N=(n-1)\cdot 10^6$. Considering atmospheric air as the propagation medium, the alterations on the refractive index is caused on variation of the air density, which is in turn a function of the major meteorological parameters such us temperature, pressure and humidity.

The International Association of Geodesy adopted the following formula for the refractive index in 1960 in terms of temperature (t in °C), pressure (P in mb) and partial water vapor pressure (e in mb) [Bomfort, 1980; Karaghani, 1987]:

$$N = (n-1)\cdot 10^6 = (n_0 - 1)\cdot \frac{1}{1 + a \cdot t}\cdot \frac{P}{1013.25} - \frac{4.2 \cdot e}{1 + a \cdot t} 10^{-2} \tag{2.20}$$

Where α is the thermal expansion of air and equals to $\frac{1}{273} = 0.00366$ and

n_o is the phase refractive index of light in standard air meteorological conditions.

The phase refractive index (n_o), for standard air conditions (temperature 273.15°K, pressure 1013.25mb, water vapor pressure 0mb and a carbon dioxide content of 0.0375%) [Ciddor 1996; Ciddor and Hill 1999; IUGG, 1999] can be computed through the phase refractivity, which is considered as:

$$N_0 = (n_0 - 1)\cdot 10^6 = 287.6155 + \cdot \frac{1.6288}{\lambda^2} + \frac{0.0136}{\lambda^4} \tag{2.21}$$

Where λ is the wavelength (in μm) of monochromatic light, for visible and near infrared amplitude of the electromagnetic spectrum in vacuum.

Additionally if the signal refers to a modulated group of waves with different frequencies then the group refractivity is computed as follows, again for standard air conditions:

$$N_{gr} = \left(n_{gr} - 1\right)\cdot 10^6 = 287.6155 + \cdot \frac{4.8866}{\lambda^2} + \frac{0.068}{\lambda^4} \tag{2.22}$$

Another empirical relation, which has sufficient accuracy with equation 2.20, that has been derived between the index of refraction and the meteorological parameters for visible light and near infrared waves, which are different from these of the standard air, is the following [Ciddor 1996; Ciddor and Hill 1999; IUGG, 1999; Torge, 2001]:

$$N = (n-1)\cdot 10^6 = N_0 \cdot \frac{273.15}{1013.25}\cdot\frac{P}{T} - 11.27\cdot\frac{e}{T} \tag{2.23}$$

Where T is the temperature in °K
P is the atmospheric pressure in mb
e is the water vapor pressure in mb and
N_0 the phase refractivity (eq. 2.21).

It has to be mentioned that equation 2.23 can be used equivalent for monochromatic light as well as for modulated light and the corresponding group refractivity (eq. 2.22). Substituting an average wavelength of 0.565μm for visible light in equation 2.21 then the phase refractivity is computed about 293 and equation 2.23 yields:

$$N = (n-1)\cdot 10^6 = 78.9\cdot\frac{P}{T} - 11.27\cdot\frac{e}{T} \tag{2.24}$$

Differentiating equation 2.24 in terms of the refraction index with respect to the local vertical z yields the dependence of the gradient of the refraction index to the meteorological parameters:

$$\frac{dn}{dz} = \frac{\partial n}{\partial T}\cdot\frac{dT}{dz} + \frac{\partial n}{\partial P}\cdot\frac{dP}{dz} + \frac{\partial n}{\partial e}\cdot\frac{de}{dz} \rightarrow \frac{dn}{dz} = -78.9\cdot 10^{-6}\cdot\frac{P}{T^2}\cdot\left(0.0342 + \frac{dT}{dz}\right) \tag{2.25}$$

In the above equation the minor effects of the water vapor pressure (less than 1/20 of temperature effects) as well as its gradient are considered negligible and so are not included, whereas the effect of the carbon dioxide content is even smaller [Breznikar and Aksamitauskas, 2012].

Additionally the equation 2.25 shows that a lapse rate of -0.0342°K·m^{-1} is necessary in order to compensate the decrease of atmospheric pressure in correspondence to height [Karaghani, 1987], which is also known as the auto-convective lapse rate [Shaw and Smietana, 1982].

2.6 The Local Geodetic Refraction Coefficient k

Inserting equation 2.25 into equation 2.12 and assuming a mean earth's radius of about 6371000m then the local coefficient of refraction k is given in terms of the meteorological parameters, the absolute temperature (T in °K), pressure (P in mb) and the temperature gradient (dT/dz in °K·m^{-1}) as it is presented below [Bahnert, 1972, 1978; Joeckel et al, 2008]:

$$k = 502.7 \cdot \frac{P}{T^2} \cdot \left(0.0342 + \frac{dT}{dz}\right) \quad (2.26)$$

The above equation implies that in order to achieve a relative accuracy of ±1% in the determination of the coefficient of refraction then the absolute temperature has to be determined with an accuracy of ±2°K, the atmospheric pressure with ±6mb and the temperature gradient with ±0.002°K·m^{-1} [Torge, 2001].

Moreover it demonstrates that the coefficient of refraction is slightly dependent on the absolute temperature and pressure but is strongly dependent on the temperature gradient and is also directly related to it [Brocks, 1939; Hirt et al, 2010; Torge, 2001; Wunderlich, 1985].

Moreover in typical meteorological conditions (T=288°K, P=1000mb) and considering the adiabatic temperature gradient (eq. 2.17) the local refraction coefficient is computed at +0.16 according to equation 2.26. This means that the radius of the sight line is six times the mean earth's radius r≈6R.

Because of the difficulty to model the refraction coefficient k or the index of refraction along the light path due to seasonal and daytime fluctuations, geodesists have adopted a universal average value of +0.13, also known as the Gaussian coefficient of refraction [Brunner 1984; Hirt et al, 2010; Reiterer, 2012].

The Gaussian refraction coefficient shows that the light ray is bent with radius that is eight times the mean earth' s radius r≈8R and can be used for average daytime conditions with a clear sky and for heights between 40m and 100m above the ground [Hirt et al 2010; Torge, 2001].

Nevertheless, supported by various researchers, the Gaussian k is not representative for the lower atmosphere, which is close to the ground (0-30m) where most of engineering type measurements take place and heating effects predominate [Bahnert 1972; Baselga et al, 2013; Brocks, 1939, 1950a, 1950b; Bomfort, 1980; Dodson and Zaher, 1985; Eschelbach 2009; Flach 2000; Hirt et al. 2010; Reiterer, 2012; Weiss 2002; Wunderlich 1985].

The positive sign of the refraction coefficient, according to the conventional definition, indicates a convex shape of the curved light ray regarding the earth's surface (follows the earth's curvature) [Hirt et al, 2010] as it is presented in figures 2.3 and 2.4. Thus, a negative height correction occurs between the apparent and the real geometric position (figure 2.3). Additionally the negative sign of k indicates a concave curvature of the optical path regarding the earth's surface and a positive height correction.

Certainly these height corrections are referred to cases of target positions and additionally figures 2.3 and 2.5 represent the real and the apparent position of a target. The whole concept of the height corrections is totally inversed with regard to spirit levelling height readings.

As it is presented in figure 2.6 the correct reading on a staff is located at the apparent position and not the real position that an observer reads from the level's telescope. As a result the height readings corrections due to refraction have the same sign with the geodetic refraction coefficient k.

2.7 Refraction Correction in Spirit Levelling by Using the Temperature Gradient

2.7.1 Kukkamaki's Approach

The first theoretical vertical temperature profile model that was developed in order to compute refraction corrections for the needs of geodetic levelling is traced back in the 19th century [Lallemand, 1896]. Lallemand in 1896 developed a logarithmic model between temperature (t) and the local vertical (z):

$$t = a + b \cdot \log(z + c) \tag{2.27}$$

Where a, b, c are the parameters of the model
t is the temperature in °C and
z is the height above the ground in meters.

Although his results were not applied in practice [Angus-Leppan, 1984], because of the fact that there were greater errors involved [Karaghani, 1987], it took about forty years later since Kukkamaki's refraction studies. Kukkamaki's approach [Kukkamaki, 1938, 1939] is based on the following assumptions [Karaghani, 1987]:

- The refraction coefficient of air depends mainly on the temperature since humidity effects are negligible small for optical propagation.
- The atmospheric air is stratified in isothermal layers which are parallel to the ground.
- The slope terrain among a single observation between the level and the staff is constant.

Thus, Kukkamaki developed an exponential temperature profile model with respect to height, which is convenient for manual computations and a limited number of air temperature sensors (2 or 3), as it is demonstrated below:

$$t = a + b \cdot z^{c} \tag{2.28}$$

Where a, b, c are the parameters of the model,
t is the temperature in °C and
z is the height above the ground in meters.

Since the refraction correction depends on the temperature gradient, the intercept (a) of the model is insignificant. The constants of the model (b & c) for a specific time can easily be computed if three temperature sensors are used (t_1, t_2 & t_3) with the corresponding height configuration (z_1, z_2 & z_3) so that:

$$\frac{z_1}{z_2} = \frac{z_2}{z_3}, \qquad \Delta t_{12} = b \cdot (z_2^c - z_1^c), \qquad \Delta t_{23} = b \cdot (z_3^c - z_2^c)$$

$$ln\left(\frac{\Delta t_{23}}{\Delta t_{12}}\right) = ln\left(\frac{z_3^c - z_2^c}{z_2^c - z_1^c}\right) = ln\left(\frac{\left(\frac{z_3}{z_2}\right)^c - 1}{1 - \left(\frac{z_1}{z_2}\right)^c}\right) = ln\left(\frac{\left(\frac{z_2}{z_1}\right)^c - \left(\frac{z_1}{z_1}\right)^c}{\left(\frac{z_2}{z_2}\right)^c - \left(\frac{z_1}{z_2}\right)^c}\right)$$

$$= \ln\left(\frac{\frac{z_2^c - z_1^c}{z_1^c}}{\frac{z_2^c - z_1^c}{z_2^c}}\right) = c \cdot ln\left(\frac{z_2}{z_1}\right)$$

Hence, the following relationships hold:

$$c = \frac{ln\left(\frac{\Delta t_{23}}{\Delta t_{12}}\right)}{ln\left(\frac{z_2}{z_1}\right)} \tag{2.29}$$

$$b = \frac{\Delta t_{12}}{z_2^c - z_1^c} = \frac{\Delta t_{23}}{z_3^c - z_2^c} \tag{2.30}$$

Figure 2.6 demonstrates a single measurement of a spirit leveling set up in an inclined terrain with slope a. The line of sight starts out horizontal at the levell and at a distance x the optical ray is inclined at an angle β. This happens due to refractive index alterations along the sight line, while a vertical deviation (C_R) occurs at the staff.

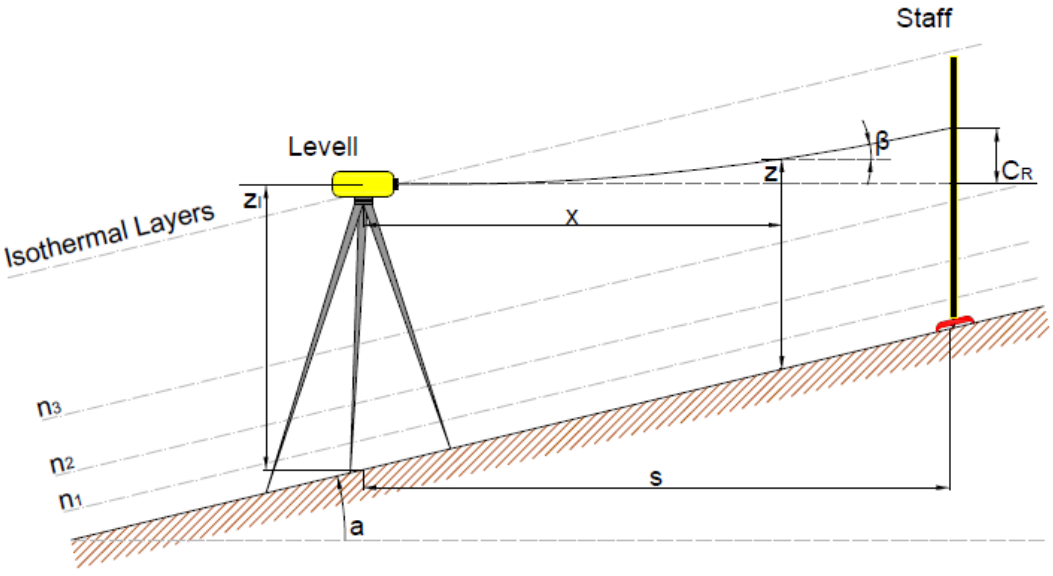

Figure 2.6 Refraction correction on a single measurement ($n_3 > n_2 > n_1$).

This means that the line of sight starts intersecting the isothermal boundaries with an angel of incidence (a). Thus by taking into account the Snellius law (eq. 2.8) and by

differentiating with respect to the refractive index (n), as it was discussed later, the following relationship holds [Kukkamaki, 1938]:

$$da = -\frac{dn}{n} \cdot \cot(a) \tag{2.31}$$

Hence the angle of refraction (β), which happens at a distance x, is given by integration along the line of sight [Angus-Leppan, 1984; Karaghani, 1987]:

$$\beta = -\int_{n_0}^{n} \frac{\cot(a)}{n} \cdot dn = -\cot(a) \cdot ln\left(\frac{n}{n_0}\right) \tag{2.32}$$

Or with sufficient accuracy [Kukkamaki, 1938]:

$$\beta = -\cot(a) \cdot \left(\frac{n - n_0}{n_0}\right) \tag{2.33}$$

Where n, n_0 are the refractive indexes at the distance x and at the level respectively.

Equation 2.33 shows that the angle of refraction depends on the ground's slope and the two refraction indexes of the sight line [Karaghani, 1987]. The differentiation of equation 2.20 with respect to temperature (t), where the un-modulated phase refractivity is considered as $N_0 \approx 293$, and neglecting the effects of the water vapor pressure (e) yields [Karaghani, 1987]:

$$dn = -\frac{293 \cdot 0.00366}{(1 + 0.00366 \cdot t)^2} \cdot \frac{P}{1013.25} \cdot 10^{-6} \cdot dt \tag{2.34}$$

Or with sufficient accuracy [Kukkamaki, 1938]

$$dn = -[0.931 - 0.0064 \cdot (t - 20)] \cdot \frac{P}{1013.25} \cdot 10^{-6} \cdot dt \tag{2.35}$$

Where t is the temperature in °C and
P is the pressure in mb.

Additionally with sufficient accuracy to the equations 2.34 and 2.35, the corresponding differentiation of equation 2.23 can be used:

$$dn = -78.9 \cdot \frac{P}{T^2} \cdot 10^{-6} \cdot dt \tag{2.36}$$

Where T is the temperature in °K.

Considering that $dt \approx \Delta t$ and that the following quantities are infinitely small increments:

$$dt = t - t_0 \;\; and \;\; dn = n - n_0$$

then by substituting equation 2.30 into equation 2.35, yields:

$$n - n_0 = d \cdot (t - t_0) \rightarrow n - n_0 = d \cdot b \cdot (z^c - z_I^c) \tag{2.37}$$

With d the change in the refractive index n, for a change of 1°C in temperature:

$$d = -[0.931 - 0.0064 \cdot (t - 20)] \cdot \frac{P}{1013.25} \cdot 10^{-6} \tag{2.38}$$

According to figure 2.6 the deviation due to refraction or the refraction correction (C_R) can be determined by integrating angle β along the line of sight. Thus, by substituting equations 2.33 and 2.37 gives:

$$\begin{aligned} C_R = \int_0^S \beta \cdot dx &= -\frac{\cot(a)}{n_0} \cdot \int_0^S (n - n_0) \cdot dx \\ &= -d \cdot b \cdot \frac{\cot(a)}{n_0} \cdot \int_0^S (z^c - z_I^c) \cdot dx \end{aligned} \tag{2.39}$$

Moreover according to figure 2.6 the following relationships hold:

$$\begin{gathered} x = (z - z_I) \cdot cot(a) \rightarrow dx = cot(a) \cdot dz \\ S = (z_b - z_I) \cdot cot(a) \end{gathered} \tag{2.40}$$

Assuming that the refractive index of atmospheric air is almost unitary (n_0=1) and by substituting the relationships of equation 2.40, then equation 2.39 yields:

$$\begin{gathered} C_R = -d \cdot b \cdot \frac{\mathrm{S}^2}{(z_b - z_I)^2} \cdot \int_{z_I}^{z_b} (z^c - z_I^c) \cdot dz \rightarrow \\ C_R = -\frac{d \cdot b \cdot \mathrm{S}^2}{(z_b - z_I)^2} \cdot \left[\frac{1}{c+1} \cdot z_b^{c+1} - z_I^c \cdot z_b + \frac{c}{c+1} \cdot z_I^{c+1}\right] \end{gathered} \tag{2.41}$$

Where S is the horizontal distance between the level and the staff
z_b is the height from the ground on the initial staff reading
z_i is the instrument height
b, c are the parameters of Kukkamaki's temperature profile model

More generally the refraction correction on a single staff reading can be determined by integrating the temperature difference of any applicable vertical temperature profile model as it is presented in the following equation:

$$C_R = -\frac{d \cdot \mathrm{S}^2}{(z_b - z_I)^2} \cdot \int_{z_I}^{z_b} \Delta t \cdot dz \tag{2.42}$$

2.7.2 The General Equation for Refraction Correction

The general equation that is going to be discussed in this chapter is based on the unified theory of geodetic refraction [Heer and Neimer, 1985] where the path of a light ray is described by the eikonal equations as it was introduced by Moritz [Moritz 1962, 1967]. The eikonal equation is a non-linear partial differential equation, which is encountered in problems of wave propagation and provides a link between physical and geometric optics.

Thus, as it was discussed later in this thesis, starting from the eikonal equation of a light wave [Moritz, 1967] then the vertical refraction angle δ, which is the angle between the chord and the tangent, can be derived by integrating the refraction index gradient along the line of sight, over a length s [Moritz, 1962; Brunner and Angus-Leppan, 1976].

Subsequently the refraction correction on a staff reading is simply determined by the multiplication of the vertical refraction angle (C_R=s·δ) and the horizontal length s [Angus-Leppan, 1984]. Assuming that the refraction index of atmospheric air is n≈1 and sin(θ)=1 and taking under consideration figure 2.6 then equation 2.16 gives:

$$C_R = -\int_0^s \frac{dn}{dz} \cdot (s - x) \cdot dx = \int_0^s \frac{dn}{dz} \cdot (x - s) \cdot dx \tag{2.43}$$

What should be denoted is that in the publication of Moritz [Moritz, 1962] the factor x is used instead of s-x in the integral. The factor s-x is correct if the vertical angle of refraction is defined on the staff, while the factor x-s is correct when it is defined at the level [Flach, 2000].

The refraction index gradient can be expressed in terms of pressure and temperature gradients by neglecting moisture effects, where the pressure spatial variations can be accurately modeled, while the temperature gradient is more complex [Angus-Leppan, 1979, 1984]. So by substituting equation 2.25 into equation 2.43 yields:

$$C_R = -78.9 \cdot 10^{-6} \cdot \frac{P}{T^2} \cdot \int_0^s \left(0.0342 + \frac{dT}{dz}\right) \cdot (x - s) \cdot dx \tag{2.44}$$

Where P is the atmospheric pressure in mb,
T is the temperature in °K,
dT/dz is vertical temperature gradient and
C_R,s,x are in meters and defined in figure 2.6.

According to the figure 2.6 and the relationships of equation 2.40, then equation 2.44 is reformed as:

$$C_R = -78.9 \cdot 10^{-6} \cdot \frac{P}{T^2} \cdot \cot^2 a \cdot \int_{Z_I}^{Z_b} \left(0.0342 + \frac{dT}{dz}\right) \cdot (z - z_b) \cdot dz \rightarrow$$

$$C_R = -78.9 \cdot 10^{-6} \cdot \frac{P}{T^2} \cdot \frac{s^2}{(z_b - z_I)^2} \cdot \left[-\frac{0.0342 \cdot (z_b - z_I)^2}{2} + \int_{Z_I}^{Z_b} \frac{dT}{dz} \cdot (z - z_b) \cdot dz \right] \quad (2.45)$$

The first term of the above equation equals to the element d (eq. 2.38), which is the change in the refractive index n, for a change of 1°C in temperature, as it was discussed later (equations 2.34, 2.35 and 2.36). By substituting d and the temperature gradient as it was introduced by the vertical temperature profile function of Kukkamaki then equation 2.45 yields:

$$C_R = -\frac{d \cdot s^2}{(z_b - z_I)^2} \cdot \left[\frac{0.0342 \cdot (z_b - z_I)^2}{2} + b \cdot \left(\frac{z_b^{c+1}}{c+1} - Z_I^c \cdot Z_b + \frac{c \cdot z_I^{c+1}}{c+1} \right) \right] \quad (2.46)$$

$$C_R = -0.0171 \cdot d \cdot s^2 - \frac{d \cdot s^2 \cdot b}{(z_b - z_I)^2} \cdot \left(\frac{z_b^{c+1}}{c+1} - Z_I^c \cdot Z_b + \frac{c \cdot z_I^{c+1}}{c+1} \right)$$

Equation 2.46 states that the refraction correction is equal to the Kukkamaki's approach but it also encompasses the influence of the pressure gradient. If the influence of the atmospheric air pressure is neglected as it is suggested by Brocks [Brocks, 1948] then the general equation for levelling refraction is identical to the correction as it was introduced by Kukkamaki [1938, 1939].

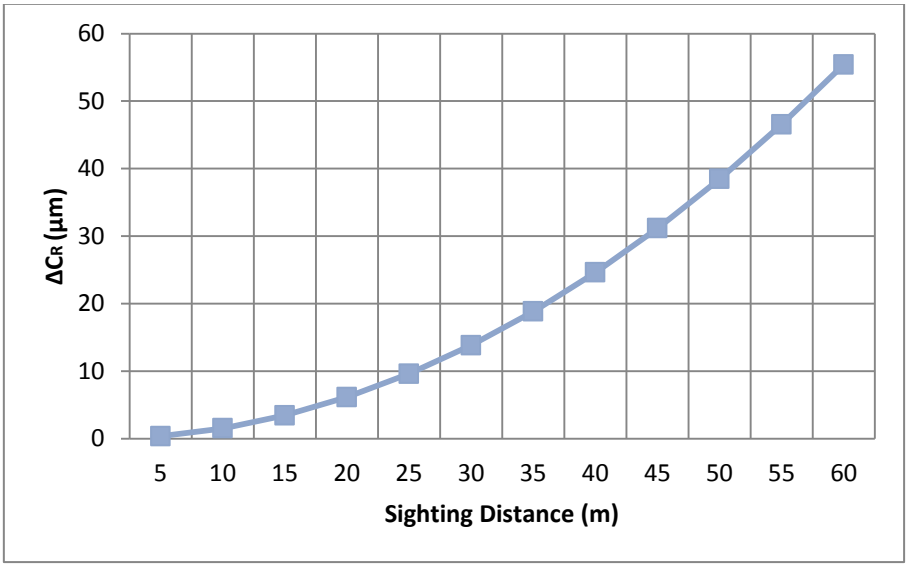

Figure 2.7 The difference between the levelling refraction correction of the general equation and the Kukkamaki's approach.

Otherwise the general equation introduces an additive part (eq. 2.46) to the height reading correction proportional to the square of the sighting distance as the quantity d is negative and typically ranges from $-8 \cdot 10^{-7}$ to -10^{-6}. Figure 2.7 demonstrates the difference between the two methods, when d equals to $-9 \cdot 10^{-7}$.

2.7.3 Remmer's Equation for Refraction Correction

Remmer has strongly advocated that the computation of the levelling refraction depends on the second and forth derivatives of the vertical temperature profile functions instead of the temperature gradient [Remmer, 1975, 1980a, 1980b]. In his studies he determined the refraction correction by means of stochastic analysis through adjustments [Angus-Leppan, 1984].

The major comment about Remmer's investigations is that as the refraction parameters are deduced from statistical modeling, which might not be positive proof. This means that other factors, which influence the measurements with the same functional form, can be the cause instead of refraction [Angus-Leppan, 1984].

Even though his results are promising, it is difficult to grasp the meaning of the second and fourth derivative in reality. His formula, which is an adaption of equation 2.42 given by Kukkamaki, for a single set up, is the following:

$$\Delta C_R = C_{R_f} - C_{R_b} = \frac{s^2}{6} \cdot \frac{dn}{dt} \cdot \left[\frac{d^2t}{dz^2} \cdot \left(z_f - z_b\right) + \frac{1}{8} \cdot \frac{d^4t}{dz^4} \cdot \left(z_f - z_b\right)^3 \right] \quad (2.47)$$

Where ΔC_R is the difference between the refraction corrections on a foresight and back-sight measurement and
s is the horizontal distance between the two rods

In the above equation the gradient of the index of refraction to temperature, can be replaced with the quantity d (eq. 2.38). Moreover it should be denoted that not all the hitherto temperature height functions are able to generate high order derivatives, as it will be discussed later on in this thesis. This is the reason why Remmer remarks Kukkamaki for the form of his equation, which is reasonable since it was considered carefully in relevance to atmospheric physics [Angus-Leppan, 1984].

2.7.4 Vertical Temperature Height Models Review

There are two temperature height functions that have already been mentioned earlier. The first one was a logarithmic model that was developed by Lallemand in 1896 [Angus-Leppan, 1984]:

$$t = a + b \cdot \log(z + c) \quad (2.48)$$

The second one was developed by the monumental investigations of Kukkamaki [Kukkamaki, 1938], which takes the following exponential form as it has already been denoted:

$$t = a + b \cdot z^c \tag{2.49}$$

Other vertical temperature height models that have been developed and tested by various researchers are the following [Heer, 1983; Heer and Neimeier, 1985; Karaghani, 1987]:

Huggershoff(1908) $$t = a + b \cdot z^2 \tag{2.50}$$

Reissmann1(1954) $$t = a + b \cdot z + c \cdot z^2 \tag{2.51}$$

Reissmann2(1954) $$t = a + b \cdot z + c \cdot z^2 + f \cdot z^3 \tag{2.52}$$

Reissmann3(1954) $$t = a + b \cdot z + c \cdot z^2 + f \cdot z^3 + g \cdot z^4 \tag{2.53}$$

Heer(1984) $$t = a + b \cdot \mathrm{e}^{c \cdot z} \tag{2.54}$$

Karaghani(1987) $$t = a \cdot z + b \cdot z^c \text{ , } z>0 \tag{2.55}$$

Where t is the temperature,
z is the local height above the ground and
a, b, c, e, f and g are the models' parameters.

According to Heer and Neimeier [Heer and Neimeier, 1985] the polynomials greater than second degree failed to work properly. Moreover Karaghani [Karaghani, 1987] mentions that the extrapolation by using the presented models is not recommended for the first 30 centimeters above the ground in field practice.

2.8 Amplitudes of the Refraction Coefficient k and the Temperature Gradient of the Lower Troposphere

As it has already been discussed earlier the refraction coefficient is mainly influenced by the amplitude and the alterations of the temperature gradient (eq. 2.26). In order to understand refraction effects thoroughly at the different parts of the atmosphere, the frequently used simplification that divides the atmosphere into higher, intermediate and lower atmosphere is followed [Brocks, 1948; Hirt et al, 2010; Wunderlich, 1985].

2.8.1 Intermediate and Higher Atmosphere

According to this concept model, the higher atmosphere corresponds for altitudes of some 100m above the ground and higher. In this region the vertical temperature gradient is independent of the earth's surface temperature and the adiabatic

temperature gradient is valid ($-0.0065°K \cdot m^{-1}$) [Bomfort,1980; Torge, 2001]. Additionally the local refraction coefficient yields values of +0.16 and +0.17.

The intermediate atmosphere refers to altitudes from 20 or 30 or 40m to some 100m above the ground [Webb, 1984; Wunderlich, 1985]. In this region the refraction coefficient is slightly influenced of surface's temperature and is mostly characterized by negative temperature gradients of about $-0.01K \cdot m^{-1}$, which equates to the value of +0.15 for k [Hirt et al, 2010]. Also the Gaussian coefficient of refraction (k=+0.13) corresponds to the region of the intermediate atmosphere and the additional dry adiabatic conditions [Hirt et al, 2010; Torge, 2001].

The majority of the studies, which observed the refraction coefficient of the intermediate and higher atmosphere, converged to the same amplitudes and indicated small variability in these regions. Mavridis and Papadimitriou [Mavridis and Papadimitriou, 1973] determined coefficient refraction values between +0.12 and +0.20 by measuring zenith angles among two hills in Thessaloniki. This is the reason why Greek geodesists use an average value of k=+0.16 instead of the Gaussian mean value [Lambrou & Pantazis, 2010].

By performing additional measurements in Athens Giannakopoulos [Giannakopoulos, 2007] and Molyvas [Molyvas, 2007] computed values of k varying from -0.05 to 0.25 and -0.25 to +0.27 respectively and Gaifillia et al [Gaifillia et al, 2016] from 0.05 to 0.12.Additionally Brocks [Brocks, 1949] computed k values varying from +0.10 to +0.12 based on temperature gradients in Nanga Parbat region of Himalaya Mountains [Hirt et al, 2010].

2.8.2 The Lower Atmosphere

In contrast to the higher and intermediate atmosphere the lower atmosphere, which corresponds to the first 30m above the ground, intense fluctuations of the temperature gradient have been computed due the varying thermal properties of the earth's surface [Angus-Leppan, 1969]. Typical values for the refraction coefficient that have been reported in previous examinations in this region are between the amplitude of -4 to +16 [Bahnert 1972, Brocks 1939, Eschelbach 2009, Flach 2000, Hirt et al. 2010, Reiterer, 2012; Weiss 2002, Wunderlich 1985].

It is generally accepted that the air temperature in an open-space decreases in addition to height, which agree with negative temperature gradient [Georgakakis et al, 2010]. This is happening because the sun's radiation that is being absorbed by the earth's surface warms the terrain. Subsequently the warm terrain heats up the lowest layers of atmospheric air, which results to turbulent motions of air due to convection. This kind of phenomenon is known as image dancing or scintillation when terrestrial optical geodetic measurements are carried out [Hirt et al, 2010].

However, the morning temperature gradient inversion is noticed in air masses that are adjacent to the ground, until the ground-level radiation budget becomes positive.

Additionally, just after sunset, the surface budget becomes negative and the terrain cooling reestablishes the temperature's inversion [Georgakais et al, 2010; Oke, 1987], resulting strong positive temperature gradients [Angus-Leppan, 1969].

Certainly there are other factors, which can contribute to temperature inversion or sun's radiation attenuation, like cloud cover, smoke, fog, wind and warm and cold air advection [Jenne, 1957]. Especially when referring to cities which their built environment is developed in valleys and are surrounded by mountains like Athens and Los Angeles.

Hence, regarding the first few meters above the ground and a ground clearance from 1 to 3m the refraction coefficient may exhibit extreme values. Thus according to Brocks [Brocks, 1950b], who used temperature measurements to compute the local coefficient of refraction; these values can vary between -3.5 and +3.5. Additionally Angus-Leppan [Angus-Leppan, 1969] by utilizing temperature measurements and a special reciprocal leveling setup obtained values between -0.5 and -4 over grass and asphalt surfaces.

Moreover, Hubner [Hubner, 1977] deployed a laser beam setup to determine the refraction coefficient values between -4 and +6 at a height of 1.5m above the ground, on a sunny day and grass land cover. Karaghani [Karaghani, 1987] by utilizing temperature measurements determined temperature gradients with a magnitude from -0.4°K·m^{-1} to +0.2°K·m^{-1} and the corresponding refraction coefficient between -2 and +1, at a height of 1.5m and different surface types.

Hirt et al [Hirt et al, 2010] investigated the short term fluctuations of the refraction coefficient on sunny days in summer. Thus they performed reciprocal vertical angle measurements with an instrument and a target height of 1.8m respectively, above a grassland surface. They presented refraction coefficient values varying from -4 to +16 and the corresponding temperature gradients from -0.5 to -0.1°K·m^{-1} during the day and from +1 to +2°K·m^{-1} after sunset.

Furthermore, Nikolitsas [Nikolitsas, 2018] computed values of the geodetic refraction coefficient k varying from 0.99 to 1.56 by performing precise geodetic levelling procedures and the temperature gradient method, underground in the tunnel of LHC accelerator at CERN.

Additionally, when the parameters of interest are investigated at a height below 1m, then their absolute values are increased. This is happening because the heat transfer is stronger closer to the ground and hence the stratified air layers become steeper.

Thus, Brocks [Brocks, 1950b] computed possible values of the refraction coefficient between -47 and +20 directly above ground, Hubner [Hubner, 1977] demonstrated corresponding values of -8 and +16 at a height of 50cm and Karaghani [Karaghani, 1987] presented values of -10 to -6 at a height of about 30cm. Subsequently this is the

reason why optical field measurements at a target height of below 50cm are generally not recommended.

Lastly, another crucial occasion is noted when the surface is consisted of water or ice, because the thermal storage of these surfaces behaves much differently [Hirt et al, 2010]. Past studies have indicated as much as a temperature inversion as an amplification of the refractive effects.

Strober [Strober, 1995] demonstrated values of the refraction coefficient between 0 and +2, by utilizing vertical angle observations at the corresponding heights from 0.5 to 4m over ice in Greenland. Additionally Angus-Leppan [Angus-Leppan, 1969] showed values varying from -14 to +10 at a height of 1.6m over ice in Alaska. Kabashi [Kabashi, 2003] computed refraction coefficient values from +1 to +18 by using reciprocal vertical angles measurements at a height of about 5m over water.

CHAPTER 3
CALIBRATION OF THE AIR TEMPERATURE SENSORS

3.1 Air Temperature Sensors

In order to measure the local temperature gradient a modification of the LORD MicroStrain TC-Link-LXRS sensors nodes (figure 3.1) was used. More specifically the compatible input sensors had been modified so as to acquire simultaneously air temperature measurements as well as relative humidity measurements while two extra channels have been added.

Figure 3.1 The LORD MicroStrain TC-Link-LXRS sensor node [http://www.microstrain.com/wireless/tc-link-1ch].

The major advantage of these sensors is that they can easily be mounted on the bar-coded invar staffs. Moreover they offer many sampling options and can be wirelessly controlled through a WSDA (Wireless Sensor Data Aggregator) network-ready gateway (figure 3.2) and the corresponding software.

These nodes can be used with multiple input compatible sensors in order to measure air temperature as well as different physical quantities like relative humidity. The technical specifications of the LORD MicroStrain TC-Link-LXRS sensors nodes are presented to the following table 3.1. Because of the modification made to the input sensors the measuring accuracy of the air temperature is questionable, while the resolution and the repeatability mentioned can be ensured (table 3.1).

Sensor Node	TC-Link-LXRS
Dimensions	58mm x 63mm x 21mm
Data Storage Capacity	2MB (up to 1 million data points)
Weight	42grams
Periodic Sampling Rate	32Hz to 4096Hz
Synchronization Between Nodes	±32µsec
Environmental Rating	Indoor use IP65/66
Power Source	Internal: 3.7V dc, 250mAh Lithium ion rechargeablebattery External:+3.2 to +9.0V dc
Operating Temperatures	-20°C to +60°C
Environmental Rating	Indoor use (IP65/66)
Measurement Range	-210°C to 1820°C (depending on the thermocouple type)
Accuracy	±0.1% of full scale or ±2°C, whichever is greater (does not include error from sensor or wire)
Resolution	0.0625°C, 24bit
Repeatability	±0.1°C (does not include error from sensor or wire)
Compatible Sensors	Type J, K, N, R, S, T, E and B thermocouples

Table 3.1 The technical specifications of the LORD MicroStrain TC-Link-LXRS sensor node [LORD MicroStrain, 2015a].

Figure 3.2 The WSDA-1500 network-ready gateway [http://www.microstrain.com/wireless/wsda-1500].

3.2 Calibration of the Air Temperature Sensors Scale

Thermocouple sensors exploit the thermoelectric effect in order to measure temperature as they produce temperature dependent voltage with exceptional linearity. The measured voltage can be then interpreted to temperature measurement by using the reference tables of the international standard [IEC, 1995] that correspond to the international temperature scale ITS-90 [BIPM, 1990].

This procedure is conducted through the calibration of the sensors' electronics via an electronic simulation. The calibration of the sensors' electronics, which is not an objective of this master thesis interests, is implemented by the manufacturer. The calibration coefficients of the TC-Link-LXRS sensor nodes (system calibration) were not available and so the sensors are assumed that are just manufactured to a standard sensitivity.

In this case (or if the calibration is considered outdated) the manufacturer suggests to perform a calibration process in a controlled environment that is typically traceable to an industry standard, such as NIST or ASTM.

Fixed loads are applied to the sensors and to a calibrated reference device, while their outputs are recorded. Then calibration coefficients (slope and offset) are calculated by applying a linear model [LORD MicroStrain, 2015b].

In this section a calibration procedure of the sensors' temperature reference scale that was carried out is being discussed. Nevertheless by this process the sensors' calibration cannot be supported due to limiting factors that are demonstrated below. However, what is being achieved is the verification of the sensors' measuring reliability, accuracy, behaviour, repeatability, hysteresis as well as the scale unification.

The scale calibration of 8 electronic air temperature sensors is attempted by using a climate chamber device, as it is presented in figure 3.3. The climate chamber Voetsch VC^3 4034, which was used, is sighted in the High Voltage Laboratory of the NTUA and is able to control the temperature and relative humidity parameters with high accuracy and at a wide range.

As reported by EURAMET [EURAMET, 2011] the calibration of thermocouples can hold in thermally stabilized baths or furnaces (like climatic chambers and dry-wells) with the use of reference or standard thermometers. The main characteristics of these devices is the temperature (and additionally for the relative humidity) deviation in time and the temperature spatial homogeneity, which for the Voetsch VC^3 4034 range from **$\pm 0.1^{o}C$ to $\pm 0.5^{o}C$** and **$\pm 0.5^{o}C$ to $\pm 1^{o}C$** respectively [Vötsch, 2016]. These parameters are annually calibrated and checked by the High Voltage Laboratory.

According to the method followed the climatic chamber is set to the desired test temperature (and relative humidity) while the 8 air temperature sensors are placed into the chamber. The chamber's temperature inhomogeneity is encountered with the

configuration of the sensors on the same immersion depth and at a limited area. Thereafter the sensors' readings are compared to the readings of the chamber's built-in thermometer, which is used as a reference device. There were also extra sensors and thermometers for cross reference purposes.

Figure 3.3 The Voetsch VC^3 4034 climatic chamber and the sensors configuration.

The disadvantage of this method is that the overall accuracy is limited to the corresponding calibrated accuracy of the climatic chamber's built-in thermometer. This is the major limiting factor in order to support an integrated calibration process.

Because as stated by NATA [NATA, 2018] the uncertainty of the reference device cannot be greater than $1/5^{th}$ of the uncertainty of the calibration required. Alternatively one sensor could be taken as fixed and corrections for the other sensors would be then calculated from it [Sirůčková, 2016].

There were five temperature set points selected (0°C, 10°C, 20°C, 30°C, 40°C) with respect to the relative humidity that was set inversely proportional to the air temperature values (80%, 65%, 50% & 40%, 35%, 20%), in order to reproduce realistic conditions of use. The following table 3.2 represents the climate chamber's built-in thermometer measurements statistics for the five different air temperature nominal values:

Set Points	Mean	St. Dev.	n
1	-0.04°C	±0.05°C	26
2	10.00°C	±0.05°C	111
3	20.01°C	±0.07°C	106
4	29.99°C	±0.08°C	41
5	40.00°C	±0.06°C	42

Table 3.2 The climatic chamber's built-in thermometer readings statistics.

The temperature readings were acquired with 1min and 5min time interval respectively for the chamber's thermometer and the sensors. Moreover the chamber requires some time to stabilize the internal temperature when a new test value is set as well as the sensors' readings present a lag time along the temperature variation. This is the reason why the 1^{st} nominal temperature value (0°C) was excluded from the

procedure since the sensors didn't manage to compensate the rapid temperature alteration at the response time that was initially forecasted.

The sensors temporal hysteresis is confronted by trimming the generated temperature time series in order to obtain the profitable part of the measurements. The following table 3.3 represents the trimmed air temperature sensors' readings statistics respectively for the four different air temperature nominal values (10°C, 20°C, 30°C, 40°C). Every sensor is coded by the last two digits of its serial number.

	Tnominal= 10°C			Tnominal= 20°C		
Sensor	**Mean**	**St. Dev.**	**n**	**Mean**	**St. Dev.**	**n**
69	10.38°C	±0.05°C	19	20.27°C	±0.07°C	18
73	10.05°C	±0.08°C	19	20.00°C	±0.09°C	18
79	9.99°C	±0.06°C	19	19.90°C	±0.10°C	18
80	10.14°C	±0.10°C	19	20.03°C	±0.12°C	18
81	10.51°C	±0.05°C	19	20.29°C	±0.07°C	18
82	10.23°C	±0.06°C	19	20.08°C	±0.09°C	18
83	10.09°C	±0.07°C	19	20.02°C	±0.06°C	18
84	10.14°C	±0.06°C	19	20.06°C	±0.06°C	18
	Tnominal= 30°C			Tnominal= 40°C		
Sensor	**Mean**	**St. Dev.**	**n**	**Mean**	**St. Dev.**	**n**
69	30.11°C	±0.03°C	5	40.01°C	±0.03°C	5
73	29.79°C	±0.03°C	5	39.71°C	±0.03°C	5
79	29.61°C	±0.03°C	5	39.39°C	±0.03°C	5
80	29.64°C	±0.05°C	5	39.41°C	±0.06°C	5
81	30.09°C	±0.06°C	5	39.99°C	±0.03°C	5
82	29.95°C	±0.05°C	5	39.88°C	±0.00°C	5
83	29.86°C	±0.03°C	5	39.79°C	±0.06°C	5
84	29.81°C	±0.06°C	5	39.64°C	±0.03°C	5

Table 3.3 The sensors readings statistics for the four nominal temperature values.

Sens./T_{nom}	**10°C**	**20°C**	**30°C**	**40°C**
69	-0.38°C	-0.25°C	-0.12°C	-0.01°C
73	-0.05°C	0.01°C	0.21°C	0.29°C
79	0.01°C	0.11°C	0.38°C	0.61°C
80	-0.15°C	-0.02°C	0.36°C	0.59°C
81	-0.51°C	-0.28°C	-0.09°C	0.01°C
82	-0.23°C	-0.07°C	0.04°C	0.13°C
83	-0.09°C	-0.01°C	0.13°C	0.21°C
84	-0.14°C	-0.04°C	0.18°C	0.36°C

Table 3.4 The deviations of the sensors mean values with respect to the mean nominal values of the chamber's built-in thermometer

The chamber's built-in thermometer readings mean values for the four nominal temperatures are subtracted to the corresponding mean values of its sensor. The

alterations obtained, which are represented to the following table 3.4, seem to have an incrementing tendency that is proportionate to the temperature increase.

Thus, the temperature deviation of each sensor is linearly modeled with respect to its readings. Hence the models that are generated below can then be used as temperature correction formulas to its sensor's readings. As presented below for every sensor there is a chart with the scattered temperature deviations and the fitted linear models with red lines (figure 3.4).

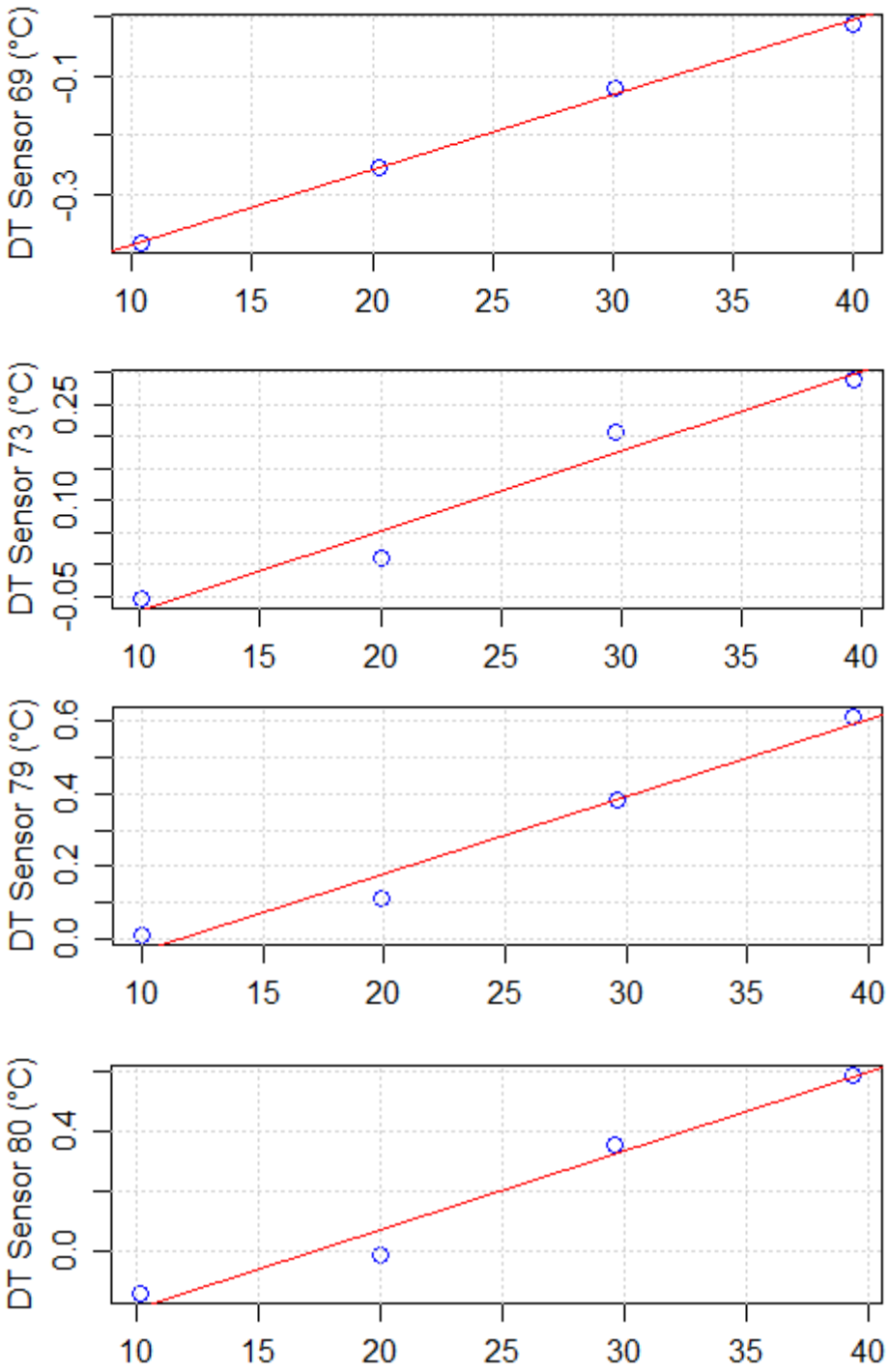

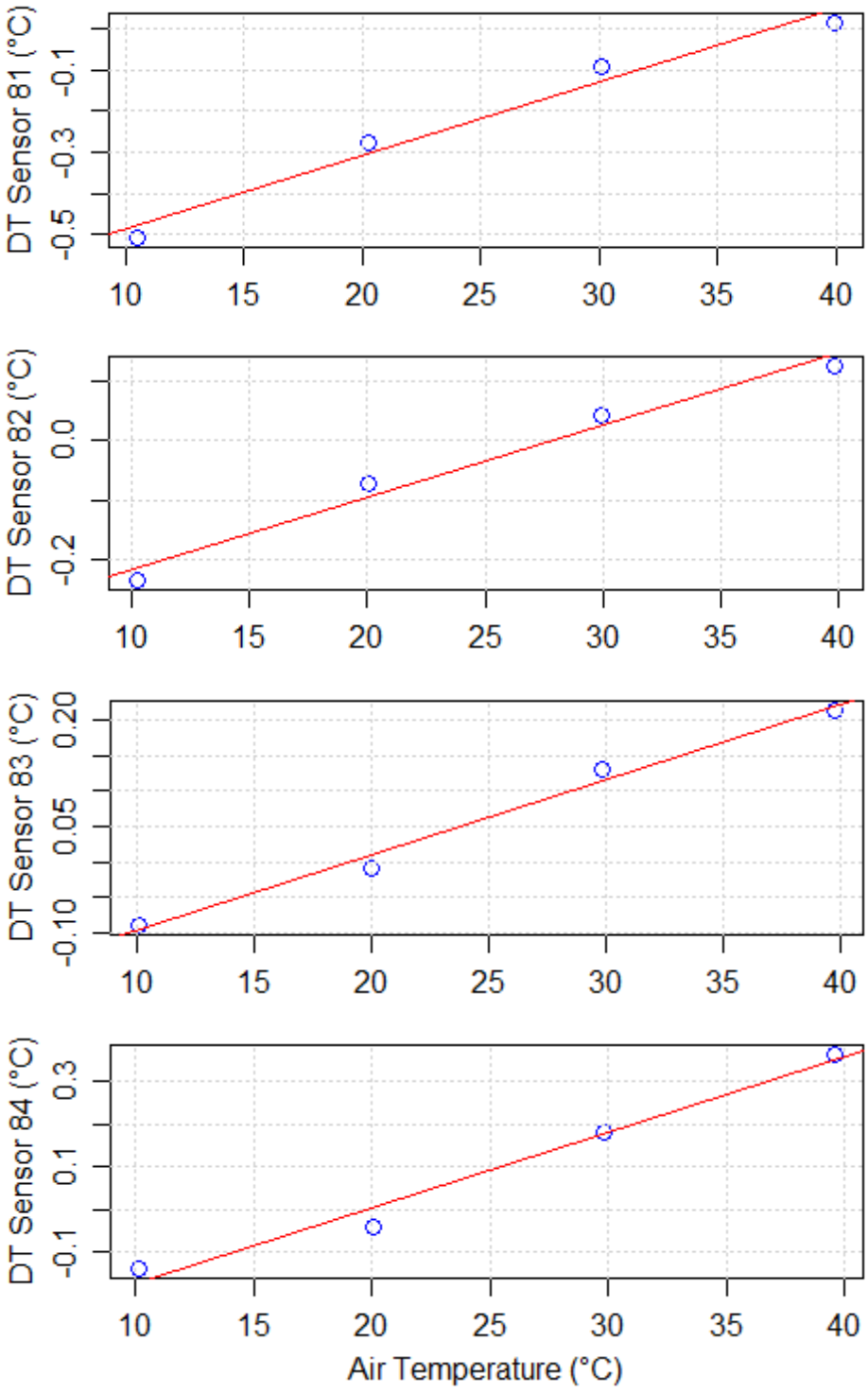

Figure 3.4 The mean temperature deviations for the four nominal values with respect to the mean values of the sensors readings and the fitted linear models.

Table 3.5 demonstrates two crucial values of the summary reports of the linear models regression analysis of the eight sensors nodes the residual standard error and the multiple R-squared. Moreover the models coefficients are statistically significant for a confidence level of 92% by performing a t-test.

Sensor	σ	R^2
69	±0.01°C	1.00
73	±0.04°C	0.96
79	±0.06°C	0.97
80	±0.07°C	0.97
81	±0.04°C	0.98
82	±0.03°C	0.98
83	±0.02°C	0.99
84	±0.04°C	0.98

Table 3.5 Linear models statistics.

The generated correction formulas for the 8 air temperature sensors readings are the following:

$$\boldsymbol{DT_{69} = 0.0127 \cdot T_{69} - 0.511} \quad (3.1)$$

$$\boldsymbol{DT_{73} = 0.0124 \cdot T_{73} - 0.196} \quad (3.2)$$

$$\boldsymbol{DT_{79} = 0.0213 \cdot T_{79} - 0.248} \quad (3.3)$$

$$\boldsymbol{DT_{80} = 0.0264 \cdot T_{80} - 0.459} \quad (3.4)$$

$$\boldsymbol{DT_{81} = 0.0178 \cdot T_{81} - 0.666} \quad (3.5)$$

$$\boldsymbol{DT_{82} = 0.0121 \cdot T_{82} - 0.337} \quad (3.6)$$

$$\boldsymbol{DT_{83} = 0.0106 \cdot T_{83} - 0.203} \quad (3.7)$$

$$\boldsymbol{DT_{84} = 0.0176 \cdot T_{84} - 0.349} \quad (3.8)$$

Since the sensors' scale calibration is over the readings are corrected according to the generated formulas. Then the alterations of the corrected values with respect to the chamber's built-in thermometer of table 3.4 are recalculated.

Hence, the corrected deviations do not indicate any trend and their absolute mean value is limited to 0.02°C or alternatively their standard deviation is calculated to ±0.03°C.

In the chamber there were also placed 4 Tinytag TGP 4017 air temperature sensors for cross reference reasons. These sensors achieve a measuring accuracy of ±0.5°C and better at this range [https://au.rs-online.com/web/p/data-loggers/5096949/]. The additional deviations calculated were in the same order of magnitude as the LORD Microstrain sensors.

The goal of this master thesis experiments is to detect the smallest possible temperature differences. Thus, there are neither any statistical tests taken place during the calibration nor any cover factor used.

The air temperature sensors measuring accuracy is intentionally limited and considered as much as their repeatability at ±0.1°C. Hence, any temperature difference that will be greater than ±0.1°C·√2=±0.14°C will be considered statistically significant for a confidence level of 68%.

3.3 Meteorological Instrumentation

The acquisition of the atmospheric pressure measurements during the experimental tests was conducted by the use of Davis Vantage Vue weather station. The particular weather station, which is presented in figure 3.5, is sighted on the rooftop of SRSE. The station's readings have a resolution of 0.1mb and the measuring accuracy is estimated at ±1mb [Davis, 2018].

Figure 3.5 The Davis Vantage Vue weather station sighted on the rooftop of the SRSE.

The Davis Vantage Vue atmospheric pressure readings are referred to the mean sea level. Thus, in order to convert the weather station's pressure readings to the desired altitude an ALMEMO 2290-8 mobile weather station (figure 3.6) was used by implementing sampling measurements.

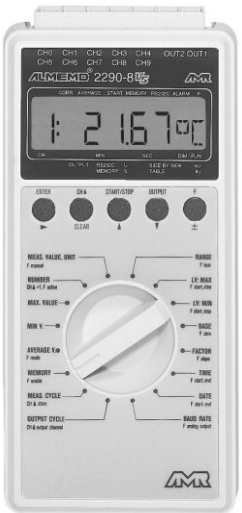

Figure 3.6 The ALMEMO 2290-8 Version 5 mobile weather station [AHLBORN, 1999]

CHAPTER 4
EXPERIMENTAL PROCEDURES AND RESULTS

4.1 Instrumentation

4.1.1. Digital Level

The digital level that was used in order to carry out the experimental tests and generate the corresponding time series was Leica DNA03 (figure 4.1). This kind of instrumentation, except of the large automation that it offers, was selected because of the high precision and resolution of a single measurement.

Figure 4.1 The Leica DNA03 digital level
[http://hds.leica-geosystems.com].

Moreover there is an advantage based on its capability to be commanded serially via RS232 interface. Thus, an automatic stand-alone operation can hold, that will be discussed later on in this section. The following table summarizes the technical specifications of Leica DNA03 digital level [Leica 2006a, 2006b].

Leica DNA03 digital level is able to perform electronic height readings on a bar coded calibrated staff by exploiting a ccd sensor and the corresponding matching techniques. Additionally the distance measurement is calculated through the image scale since the bar code dimension is standard at a maximum range of 60m.

The resolution of a single height reading comes up with 5 decimal of meter units (±10μm), while the standard deviation of a height difference of 1km double run geodetic levelling line by using invar staffs is computed to ±0.3mm, according to ISO 17123-2.

Accuracy	Standard deviation height measurement per 1km double run (ISO 17123-2)
Electronic Measurements:	
with invar staffs	±0.3mm
with standard staffs	±1.0mm
Optical measurements	±2.0mm
Distance Measurements	±5mm/10m (Standard Deviation)
Single Measurement Time	Typically 3 seconds
Telescope	
Magnification	24x
Free objective diameter	36mm
Opening angle	2^{o}
Field of view	3.5m at 100m
Minimum target distance	0.6m
Multiplication constant	100
Addition constant	0
Circular Level Sensitivity	8'/2mm
Compensator	
Type	Pendulum compensator with magnetic damping
Slope range	~ ±10'
Setting accuracy	±0.3" (Standard Deviation)
Weight	2.85kg (including battery GEB111)
Measured Values Corrections	
Collimation error correction	automatically
Earth curvature correction	on/off switch; level probe with correction (R=6378km)
Data Record	
Internal memory	~6000 measurements or ~1650 stations
Serial interface RS232	GSI-8/16 format
Data buckup	PCMCIA-card (flash, SRAM), up to 32MB capacity
Enviromental Conditions	
Working temperature	-20^{o}C to +50^{o}C
Storage temperature	-40^{o}C to +70^{o}C
Dust/water proof (IEC60529)	IP53
Humidity	up to 95% no condensation
Magnetic Field Sensitivity	Line-of-sight difference in horizontal constant magnetic field at a field strength of 0µT up to ±400µT [4 Gauss] ≤ 1"

Table 4.1 Technical specifications of Leica DNA03 digital level [Leica 2006a, 2006b].

These two aforementioned values are not representative for the repeatability of a measurement or else the standard deviation of a single height reading. Pellegrinelli et al have demonstrated an empirical relationship in order to define the standard deviation of a single height reading with respect to the sighting distance (eq. 4.1), by developing a motorization of DNA03 [Pellegrinelli et al, 2013].

$$St.Dev.(mm) = 0.001 \cdot Dist.(m) + 0.005 \quad (4.1)$$

Where St.Dev. is the standard deviation of a height reading on an invar staff in mm and
Dist. is the horizontal distance between the level and the staff in m.

Thus they performed an automatic stand-alone set up which measured continuously for 8 days in an indoor tunnel. The time interval was defined at 5 to 6 minutes, while five invar staffs were mounted in different distances. Hence they generated about 2000 readings per sighting distance and a linear model was then fitted to the computed standard deviation values. The results of this experimental test are represented in figure 4.2.

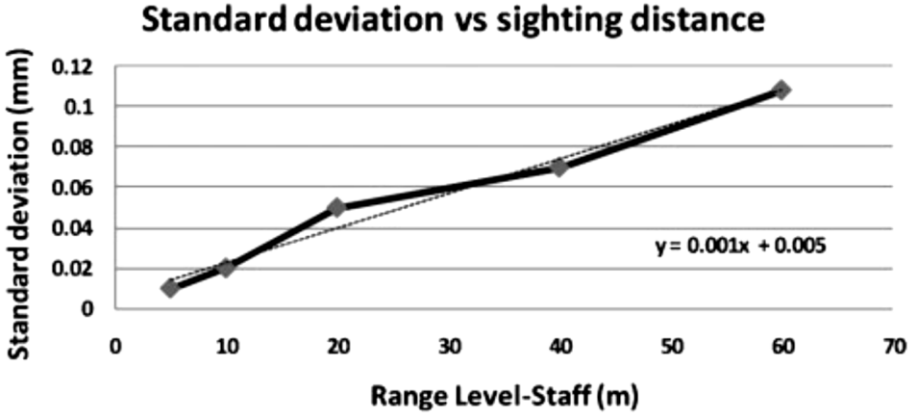

Figure 4.2 The standard deviation of the staffs readings with respect to the sighting distance [Pellegrinelli et al, 2013].

Additionally the manufacturer denotes that the standard deviation of the height readings average has to be less than ±700μm at a sighting distance of 20m [Leica, 2006b]. This means that the repeatability of the Leica DNA03 digital level is not static but is depended on the micrometeorology of the terrain, the environmental and lighting conditions.

Apodouliankis in his diploma thesis [Apodoulianakis, 2011] performed additional experimental tests with the Leica DNA03 at different lighting conditions and varying sighting distances. He showed that the slope of the linear model of equation 4.1 can range between 0.0038 and 0.0007, while the intercept can take either positive or negative sign values.

4.1.2. Bar Coded Invar Staffs

The bar coded staffs selected were the GPCL2 (figure 4.3) and GPCL3 invar staffs. The main body of this equipment consists of aluminum, while the bar coded tape consists of invar. This kind of equipment was selected because of its remarkable graduation and calibration results and its extremely low thermal expansion.

The bar code elements are engraved with an interferometrically controlled laser beam, ensuring superior graduation accuracy and edge sharpness. The calibration of the levelling rods is based on a CCD technique described by DIN18717 [Wasmeier & Foppe, 2006]. Thus the bar code elements positions of the GCPL invar staffs are determined with an accuracy of about ±20μm [Leica, 2007].

Figure 4.3 The GPCL2 invar staff
[http://accessories.leica-geosystems.com]

The following table (4.2) represents the technical specifications of the GPCL2 and GCPL3 bar coded invar staffs [Leica, 2007].

Total Length (L_{total})	2m & 3.05m resp.
Valid Measurement Range L_{scale}	0.035-1.94m & 0.035-2.98m
Weight	4.2kg & 4.9kg
Thermal Expansion	<1ppm/^{o}C
ΔL (DIN18717)	±(0.02mm+L·2·10^{-5})
Verticality Deviation	±5'
Circular Bubbles Accuracy	12'/2mm
Bar Code Unit Element Width	2.025mm
Operating Temperatures	-20^{o}C + 50^{o}C

Table 4.2 Technical specifications of Leica GPCL2 & GCPL3 invar staffs
[Leica, 2007].

4.1.3. Digital Level Check

The Leica DNA03 digital level was checked by the local comparator of Metrica SA, which is the official distributor of Leica Geosystems AG in Greece, in order to secure the instrumentation's functionality. Moreover before the experimental tests have taken place a classic check and adjust field procedure was carried out in order to define the collimation error correction.

The collimation error (α in arc secs, eq. 4.2) is the vertical angle between the actual line of sight and the ideal horizontal line (figure 4.4 a), where 1" = 0.1mm/20m [Leica, 2006b]. The collimation error was determined by developing the classic from the center procedure "AxBx" (figure 4.4 b), where four height readings are carried out (A_1, B_1, A_2 and B_2) from two different instrument stations (1 and 2). The distance between the staffs (a) is defined at about 30m.

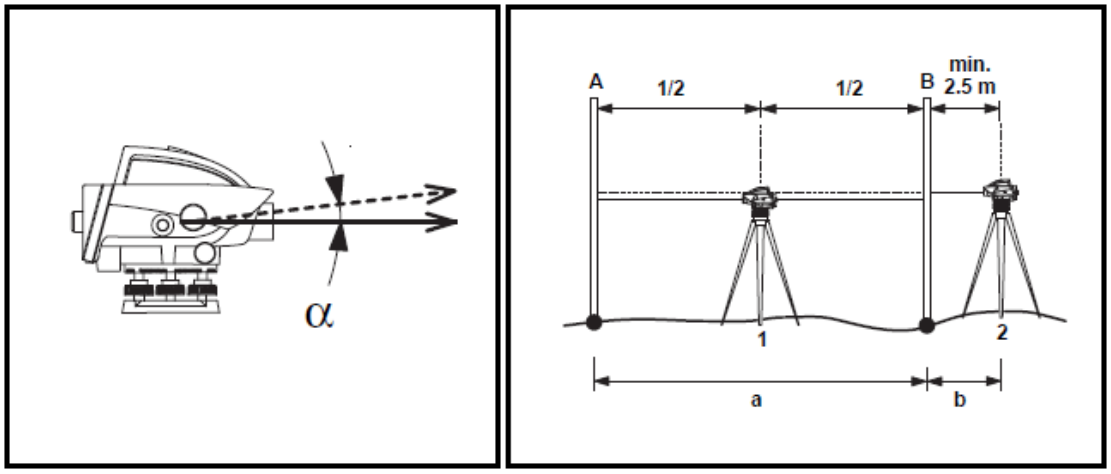

(a) (b)

Figure 4.4 The collimation angle error (a) and the classic check and adjust configuration set up (b) [Leica, 2006b].

$$a = \arctan\left[\frac{A_1 - B_1 + B_2 - A_2}{d_1 - d_2 + d_3 - d_4}\right] \tag{4.2}$$

Where α is the collimation error in arc secs,
A_i, B_i the level's readings at the corresponding staff's positions and
d_i the corresponding distances between the level and the staff.

After developing the aforementioned procedure the collimation error was computed at **2.9 arc secs** and was stored in the level's memory as a corrective value. The spatial resolution of this value corresponds to about 844μm at a distance of 60m.

4.1.4. Stand Alone Set Up

In order to obtain time series of continuous digital height readings, a programmable and automatic stand-alone set up of the digital levell needed to be implemented. The issues to overcome and succeed such an operation had to do with the uninterrupted power supply of the digital level, while a seamless data transfer had to be

accomplished. Thus a GEV 186 Y cable (figure 4.5) was selected as it is capable of integrating an external 12V battery and an RS232 serial laptop communication, with the use of the corresponding adaptors.

Figure 4.5 Leica GEV 186 Y cable
[https://leica-geosystems.com].

The height readings acquisition was conducted with the use of executable automatic recording software that was pre-purposely written in Visual Basic 6 [Nikolitsas K., 2015].

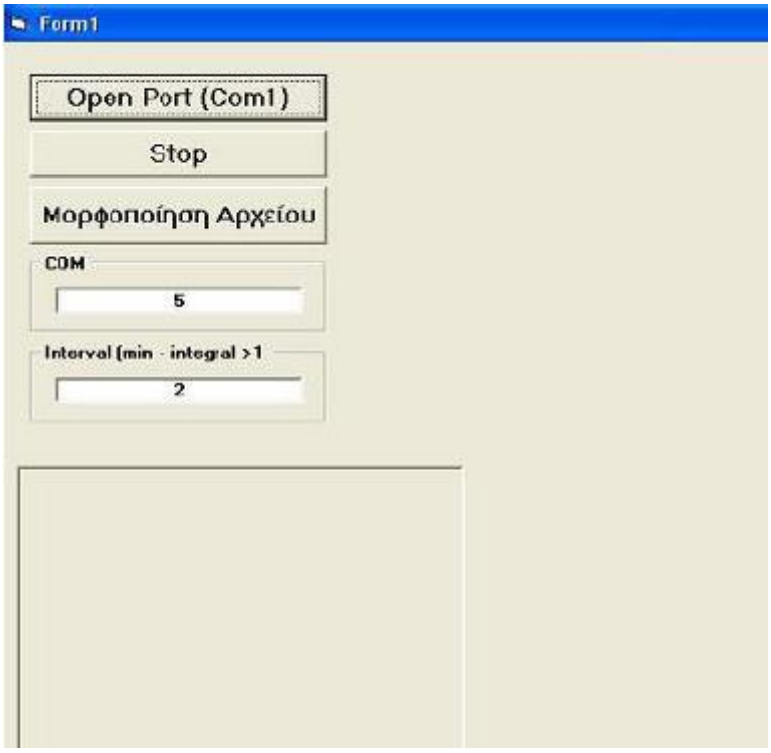

Figure 4.6 The Graphical User Interface of the automatic recording software.

The software used utilizes the communication parameters (baudrate, data bits, parity, stop bit) of the digital level via the RS232 serial interface [Leica, 2006b] as well as the GSI-8 format [Leica, 2002] in order to online command and data transfer between

the computer and the instrument. The communication portal and the time interval are defined on the Graphical User Interface (figure 4.6) of the software while the measuring procedure initializes by pressing the “Open Port” button.

Hence, a “txt” file is created, where every measurement is recorded by three lines (figure 4.7). The first two lines, which are included in hash quotation, correspond to date and system’s time respectively. The third line consists of two alphanumerical values in double quotes that represent the measured distance and the height reading in GSI- 8 data format.

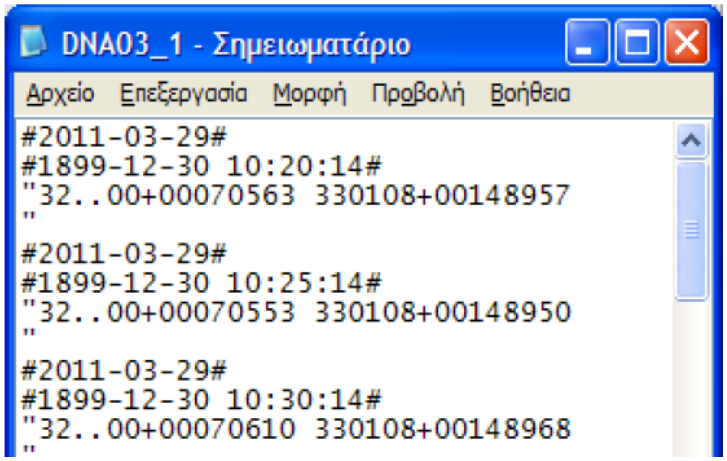

Figure 4.7 The txt data file configuration.

The only disadvantage of the software is that the initialization of the measuring process cannot be automated and has to be started manually. As a result the synchronization of the different datasets is on the order of some seconds. More photographic documentation of the whole instrumentation set up will be represented later in this chapter.

4.2 Experimental Set Ups and Generated Time Series

There were three experimental tests that were carried out at the School of Rural and Surveying Engineering of the National Technical University of Athens in order to compute refraction corrections and subsequently the refraction coefficients (k) along time in spirit leveling measurements.

The aim of this thesis is to investigate the refraction affection and its amplitude in optical geodetic measurements so as to obtain a correction method to high accuracy geodetic measurements.

Thus an automatic, stand alone and controlled set up of a digital level was deployed that was observing a bar coded invar staff. The height readings acquisition had a time scale of 5 minutes at a period of some days.

Simultaneously to the height readings there were air temperature measurements taken place by using air temperature sensors mounted on different height positions on the

bar coded staff. The refraction correction was then computed by using the direct measurement of the temperature gradient and the corresponding temperature height models.

4.2.1. Indoor Set up at 25m

The first two experimental tests conducted indoors at the basement tunnel of SRSE (figure 4.8), which is used for the metrological check and calibration of geodetic instrumentation. The tunnel has a total length of about 50m. During the experiments the heating and the ventilation of the tunnel was switched off in order to minimize air turbulence and thus air temperature fluctuations.

Figure 4.8 The instrumentation set up of the indoor experimental test at 25m.

The instrumentation configuration is presented in the above photos (figure 4.8), where the horizontal distance between the level and the staff was approximately defined at 25m.

The generated time series of the DNA03 readings (heights and distances) as it was finally trimmed started at 2017-09-22 15:45:00 and ended at 2017-09-25 11:00:00 forming a total period of 2days 19hours and 15minutes with a 7hours gap due to a technical failure. The digital level's readings statistics are presented in table 4.3, where the n symbol represents the number of the measurements and the NA (Not Available) the number of the measurements that failed to be acquired.

DNA Reading	Range	Mean	St. Dev.	n/NA
Height	1.32001m - 1.32022m [210μm]	1.320096m	±29μm	808/102
Distance	25.290m - 25.317m [27mm]	25.305m	±5mm	808/102

Table 4.3 The digital level's reading statistics for the indoor experimental test at 25m.

Additionally the instrument height was configured and measured at 1.35 m, so according to the mean values of table 4.3 the tunnels mean inclination is computed at -1.2‰. The height readings of the first experimental test are illustrated in figure 4.9. The chart demonstrates a slight cyclicality of the height readings while they seem stationary.

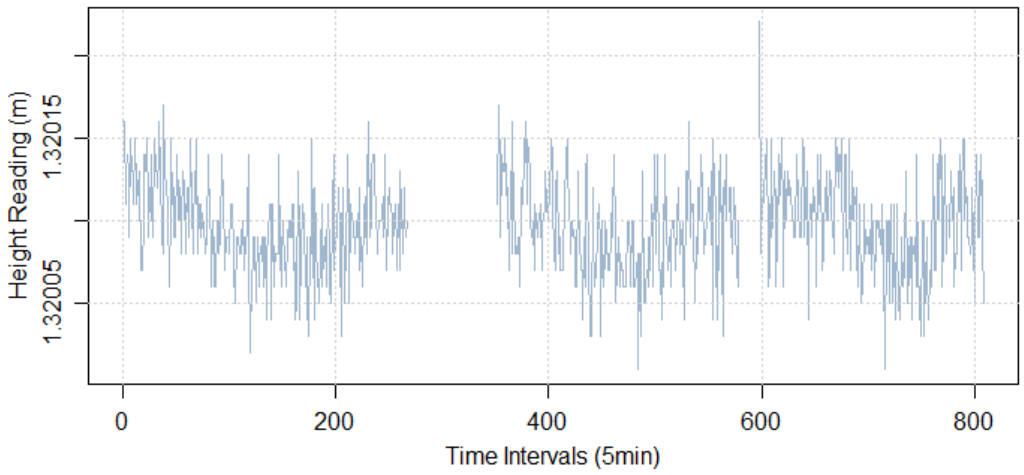

Figure 4.9 The height readings chart of the indoor experimental test at 25m as a line.

An effective way to illustrate the distribution of the height readings is by using a kernel density plot figure 4.10. The algorithm used disperses the mass of the empirical distribution function over a regular grid of 512 equally spaced points.

The fast Fourier transform (FFT) is used to convolve this approximation with a discretized version of the kernel. Then a linear approximation is used in order to evaluate the density at the specified points [http://stat.ethz.ch/R-manual/R-devel/library/stats/html/density.html]. The specific kernel function uses the Gaussian distribution and the smoothing bandwidth computation is based on the normal reference rule.

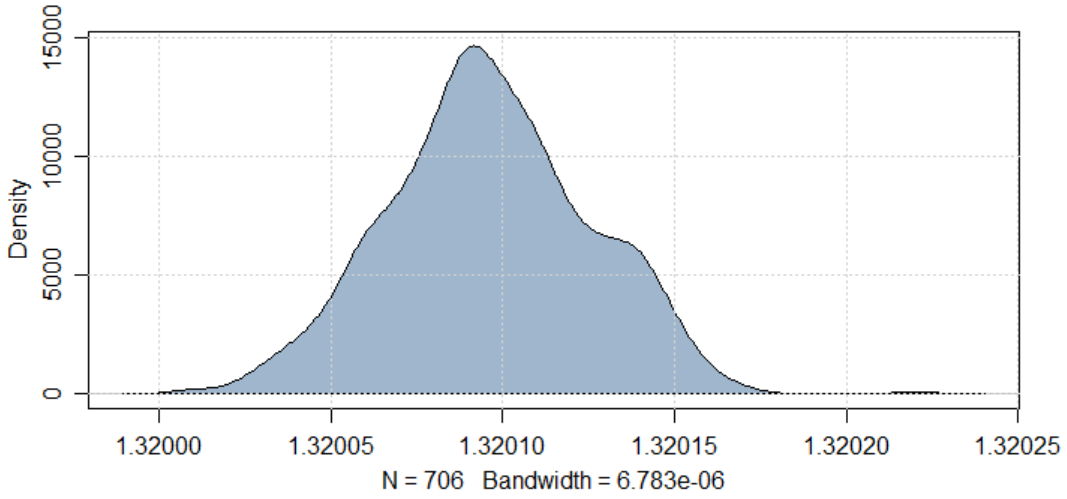

Figure 4.10 The height readings distribution of the indoor experimental test at 25m via a kernel density plot.

The density plot of the height readings (figure 4.10) of the first indoor experimental test indicates one main value, which corresponds to the height measurements mean value. This fact is in addition to the observed cyclicality of the charts in figure 4.9 and shows the noise contained therein the data.

Sensor	Range	Mean	St. Dev.	n/NA	Height
69	24.81°C - 24.93°C [0.13°C]	24.84°C	±0.04°C	808/0	0.09m
73	25.11°C - 25.24°C [0.13°C]	25.12°C	±0.02°C	808/0	0.47m
80	25.39°C - 25.59°C [0.19°C]	25.46°C	±0.01°C	808/0	0.81m
82	25.22°C - 25.41°C [0.19°C]	25.29°C	±0.05°C	808/0	1.20m
83	25.44°C - 25.57°C [0.13°C]	25.54°C	±0.03°C	808/0	1.58m
84	25.86°C - 25.98°C [0.13°C]	25.87°C	±0.03°C	808/0	2.09m

Table 4.4 The air temperature readings statistics of the indoor experimental test at 25m.

The temperature gradient was measured by using 6 LORD Microstrain air temperature sensor nodes mounted on approximately equal vertical segments of the 2 meter bar coded invar staff. The air temperature readings statistics are presented in table 4.4 above.

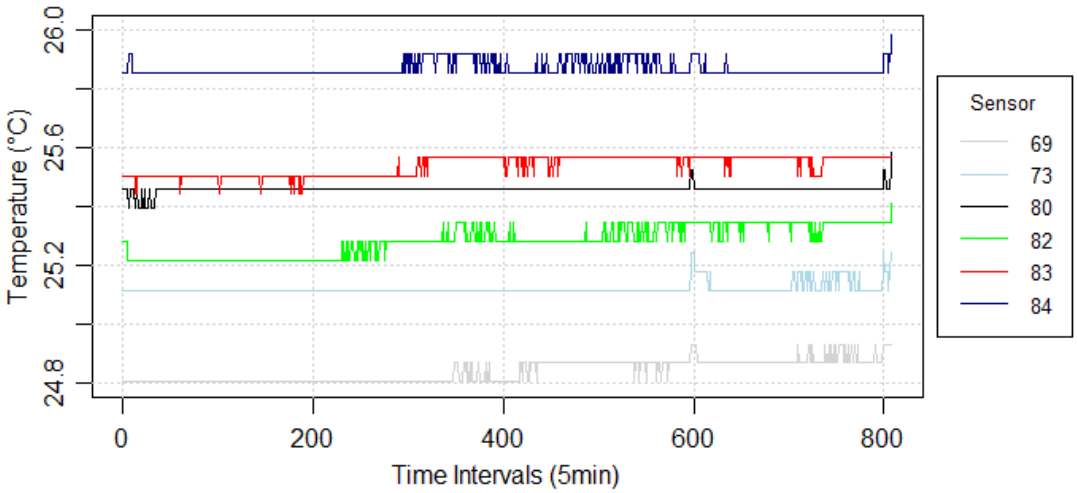

Figure 4.11 The air temperature sensors readings for the indoor experimental test at 25m.

The air temperature time series are presented in figure 4.11 where they seem complete stationary while they demonstrate neither a trend nor cyclicality. What needs to be highlighted is that some observed air temperature differences are not statistically significant even if the air temperature sensors measuring accuracy is optimistically limited to ±0.1°C.

Range	Mean	St. Dev.	n/NA
998.1mbar - 1003.8mbar [5.7mbar]	1001.5mbar	±1.6mbar	808/0

Table 4.5 The pressure readings statistics of the indoor experimental test at 25m.

The pressure readings as they were acquired from the weather station and converted to the tunnels altitude are presented in figure 4.12, while their statistics in table 4.5. It is noticed that the local maxima and minima points between the pressure and the height readings appear to be opposite in most cases.

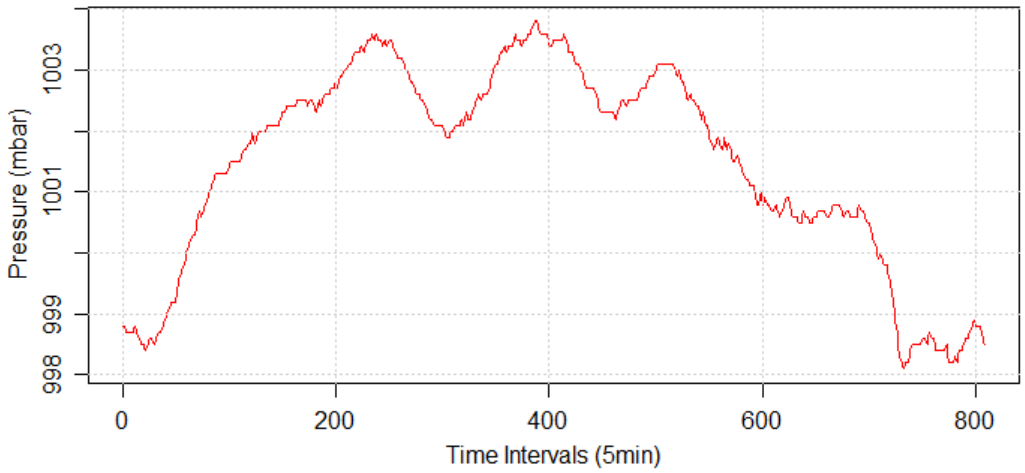

Figure 4.12 The pressure readings time series of the indoor experimental test at 25m.

The matrix below (table 4.6) contains the Pearson correlation coefficients between all the measured parameters of the discussed dataset. The correlation matrix does not indicate any strong correlation but weak and mainly downhill linear relationships.

	Height	Distance	Temperature (80)	Pressure
Height	1.00	0.36	-0.04	-0.09
Distance	0.36	1.00	-0.05	-0.04
Temperature (80)	-0.04	-0.05	1.00	0.14
Pressure	-0.09	-0.04	0.14	1.00

Table 4.6 The Pearson correlation coefficients of the measured values of the indoor experimental test at 25m.

4.2.2. Indoor Set up at 50m

The second indoor experimental test had the same instrumentation set up as it was previously presented in figure 4.8. The only difference is that the horizontal distance between the level and the staff was configured at about 50m.

The digital level's measurements started at 2017-12-21 16:00:00 and ended at 2017-12-25 23:50:00, which is namely a total period of 4 days 7hours and 50 minutes. The level's readings statistics are presented in table 4.7.

DNA Reading	Range	Mean	St. Dev.	n/NA
Height	1.11194m - 1.11236m [420μm]	1.112146m	±65μm	1247/23
Distance	49.510 m - 49.548m [38mm]	49.529m	±7mm	1247/23

Table 4.7 The digital level's reading statistics for the indoor experimental test at 50m.

The instrument height was now developed and measured at 1.27m. Thus, the mean inclination of the tunnel at this distance is computed at -3.2‰ according to the mean values of table 4.7. The height readings of the second indoor experimental test are represented by a grey line in figure 4.13.

The height readings appear a slight cyclicality while they demonstrate a decreasing trend.

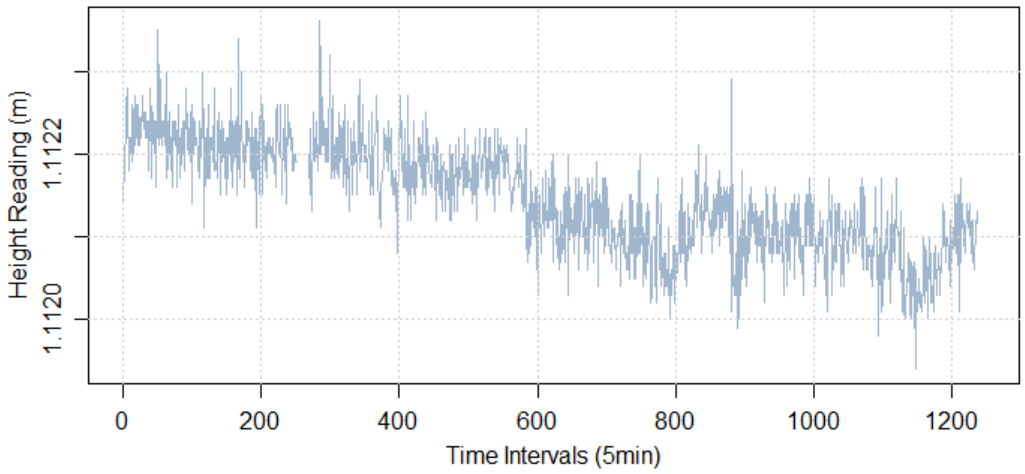

Figure 4.13 The height readings chart of the indoor experimental test at 50m as a line.

Additionally the kernel density plot, which is presented in figure 4.14, indicates that there are two main values in the height readings time series.

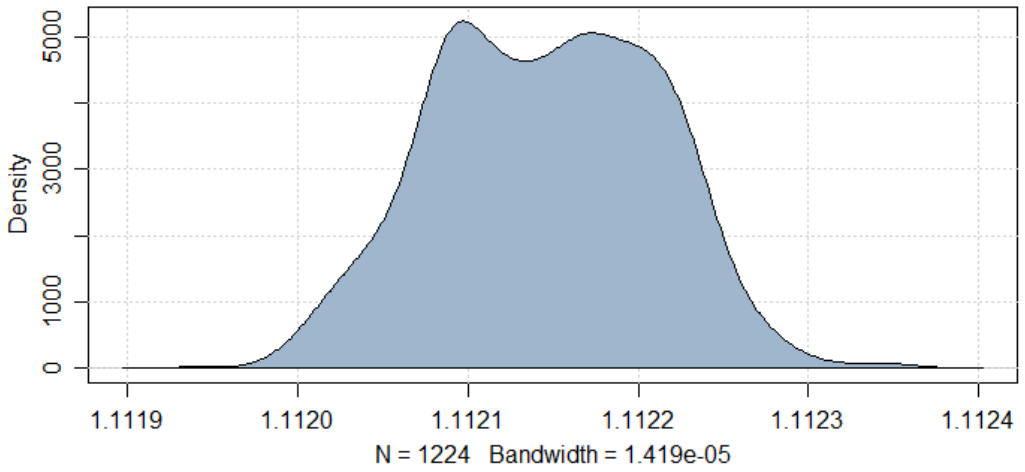

Figure 4.14 The height readings distribution of the second experimental test at 50m via a kernel density plot.

In this experimental test there were seven air temperature sensors used that were mounted on equal vertical segments on the staff. The sensors heights above the tunnel's ground floor as well as their readings statistics are contained in table 4.8.

Sensor	Range	Mean	St. Dev.	n/NA	Height
69	17.84°C - 18.35°C [0.51°C]	18.05°C	±0.17°C	1247/0	0.10m
73	17.96°C - 18.53°C [0.57°C]	18.20°C	±0.16°C	1247/0	0.35m
79	18.01°C - 18.58°C [0.57°C]	18.29°C	±0.16°C	1247/0	0.63m
80	18.02°C - 18.53°C [0.51°C]	18.24°C	±0.17°C	1247/0	0.93m
82	17.63°C - 18.20°C [0.57°C]	17.88°C	±0.17°C	1247/0	1.49m
83	17.61°C - 18.24°C [0.63°C]	17.86°C	±0.17°C	1247/0	1.77m
84	17.65°C - 18.29°C [0.64°C]	17.90°C	±0.17°C	1247/0	2.03m

Table 4.8 The air temperature readings statistics of the indoor experimental test at 50m.

Figure 4.15 illustrates the sensors air temperature readings where a decreasing tendency is noticed. The fact that causes concern is the multiple intersections among some sensors measurements due to the minor temperature differences that were occurred in addition to their dense arrangement.

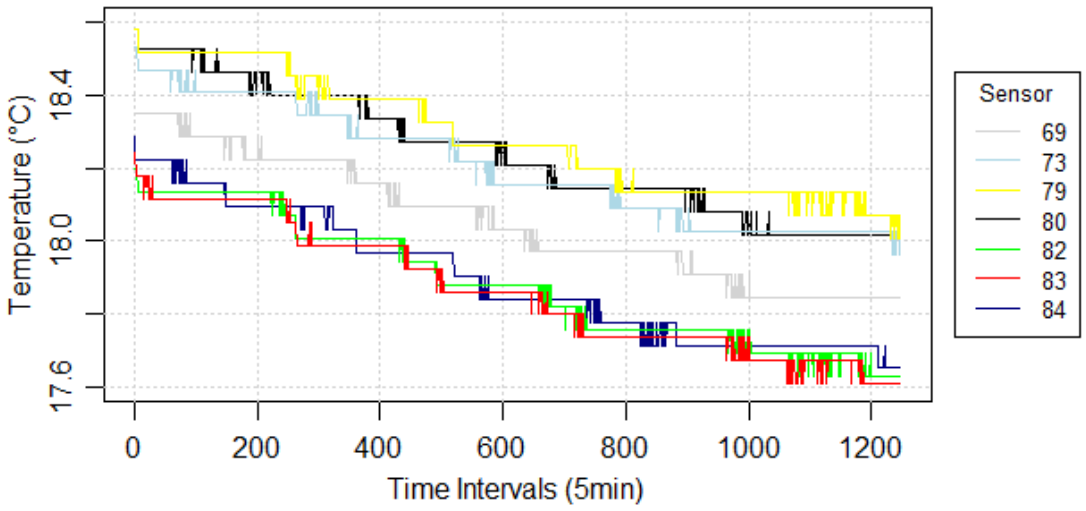

Figure 4.15 The air temperature sensors readings for the indoor experimental test at 50m.

The atmospheric pressure readings statistics are presented in table 4.9, while their time series are illustrated in figure 4.16. The atmospheric pressure is decreasing during the first day and is increasing thereafter.

Range	Mean	St. Dev.	n/NA
996.0mbar - 1011.1mbar [15.1mbar]	1004.88mbar	±4.18mbar	1247/0

Table 4.9 The pressure readings statistics of the indoor experimental test at 50m.

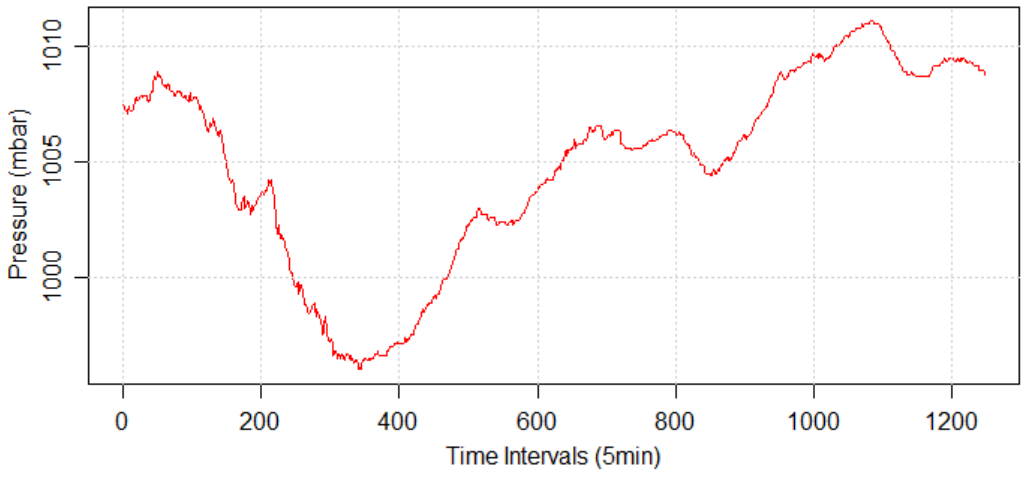

Figure 4.16 The pressure readings time series of the indoor experimental test at 50m.

Table 4.10 demonstrates the Pearson correlation coefficients among the measured values, where some strong and moderate correlations are noticed. This is not a general assumption but characterizes the particular dataset and is due to the trends among the different time series.

	Height	Distance	Temperature (80)	Pressure
Height	1.00	-0.45	0.78	-0.49
Distance	-0.45	1.00	-0.48	0.32
Temperature (80)	0.78	-0.48	1.00	-0.53
Pressure	-0.49	0.32	-0.53	1.00

Table 4.10 The Pearson correlation coefficients of the measured values of the indoor experimental test at 50m.

These correlations came up because the height readings along with the temperature measurements are decreasing, forming a strong uphill linear relationship. While atmospheric pressure is increasing indicating a moderate downhill linear relationship with respect to height.

4.2.3. First Outdoor Set up at 40m

The third and fourth experimental tests were carried out outdoors on the rooftop of SRSE. The only alteration to the previously conducted experiments is that a 3 meter bar coded invar staff was used. Moreover in order to secure proper lighting conditions during the night and assure the level's measuring ability a spotlight was used.

The spotlight was placed at safe distance so the air temperature sensors would not get heated, while an automatic operating mode was accomplished by using a timer switch. The overall instrumentation set up of the outdoor experimental tests is presented in the figures 4.17 and 4.18, where the horizontal distance between the level and the staff was a bit less than 40m.

The measurements of the first outdoor experimental test initiated at 2017-12-30 17:35:00 and ended 2018-01-02 18:30:00 forming a total period of 3 days and 55 minutes. The gaps occurred on the height readings time series happened when the level's telescope was slightly rotated due to lateral wind and when the test was paused because of rain.

Figure 4.17 The instrumentation set up of the outdoor experimental tests at 40m, the automatic online command of the digital level (left) and the level's focusing on the bar coded staff (right).

The first major concern, when performing outdoors optical measurements with unstable atmospheric conditions (during the day with a clear sky), is that the direct measurement of the temperature gradient becomes unreliable. This happens because atmospheric turbulence fluctuations are increased and are mainly affected by the heat flux due to solar radiation [Brunner & Kukuvec, 2011].

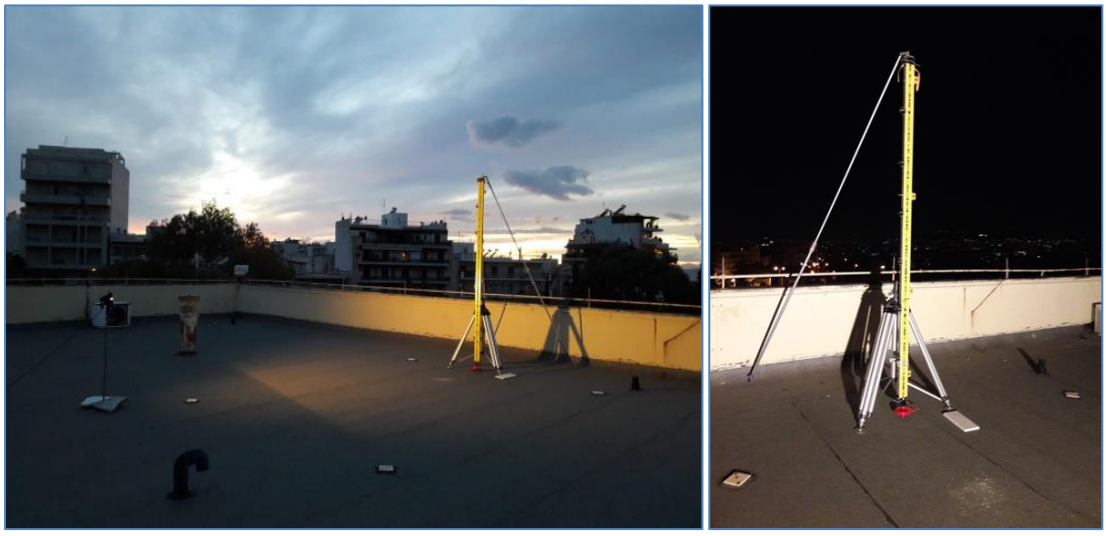

Figure 4.18 The spotlight and the3m invar bar coded staff after sunset (left) and the staff during the night (right).

Moreover when the air temperature sensors are directly radiated by the sun they get heated due to their thermal capacity. Thus the credibility of the air temperature measurements becomes questionable. Hence, because the heating effects dominate the parts of the time series just after sunrise (08:00) and just before sunset (17:00) were trimmed off and excluded from the computations.

The height readings statistics of the first outdoor experimental test at 40m are presented in table 4.11. The instrument height was defined and measured at 1.647m. Thus, according to the mean values of table 4.11 the mean inclination of the rooftop is computed at -0.4‰.

DNA Reading	Range	Mean	St. Dev.	n/NA
Height	1.63064m - 1.63176m [1.12mm]	1.631176m	±205μm	876/476
Distance	37.714m - 37.766m [52mm]	37.740m	±8mm	876/476

Table 4.11 The digital level's reading statistics for the first outdoor experimental test at 40m.

The following figure 4.19 represents the height readings of the digital level for the first outdoor experimental test. The trimmed part of the height readings time series is symbolized with red color. Again the height readings graphs display a slight cyclicality and an upward trend.

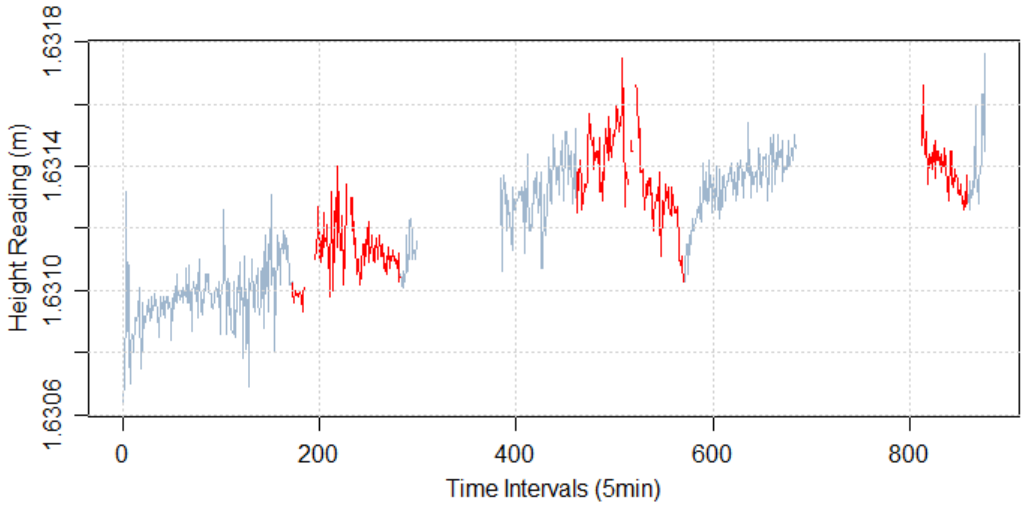

Figure 4.19 The height readings and the trimmed parts (red color) of the first outdoor experimental test at 40m as a line.

Additionally figure 4.20 demonstrates the initial as well as the trimmed height readings distribution with black and red color respectively, while the number of the observations (N) and the smoothing bandwidth are referred to the trimmed readings.

These two kernel density plots indicate that there are two main values contained in the height measurements. Moreover the red line shows that the amplitude of the height readings is slightly bigger during the day.

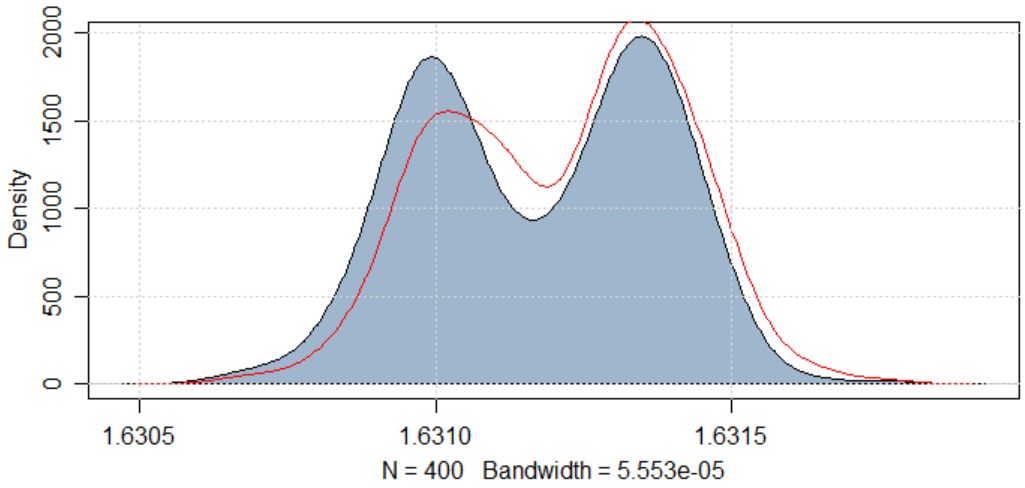

Figure 4.20 The initial (red color) and the trimmed height readings distribution of the first outdoor experimental test at 40m via a kernel density plot.

Sensor	Range	Mean	St. Dev.	n/NA	Height
69	3.29°C - 14.05°C [10.76°C]	8.05°C	±2.90°C	876/327	0.11m
73	3.85°C - 14.04°C [10.19°C]	8.22°C	±2.78°C	876/327	0.49m
79	3.97°C - 15.20°C [11.23°C]	8.40°C	±2.81°C	876/327	0.92m
80	4.03°C - 16.48°C [12.45°C]	8.43°C	±2.81°C	876/327	1.35m
82	4.22°C - 15.73°C [11.51°C]	8.45°C	± 2.67°C	876/327	2.20m
83	4.35°C - 15.71°C [11.37°C]	8.49°C	±2.69°C	876/327	2.64m
84	4.74°C - 15.93°C [11.19°C]	8.85°C	±2.64°C	876/327	3.06m

Table 4.12 The air temperature readings statistics of the first outdoor experimental test at 40m.

Table 4.12 demonstrates the 8 air temperature sensors readings statistics of the first outdoor experimental test at 40m. Additionally the plots below (figure 4.21) represents the air temperature sensors time series as they were initially acquired (figure 4.21 (a)), as they were finally trimmed (figure 4.21 (b)) and a zoom in the first 150 measurements (figure 4.21 (c)).

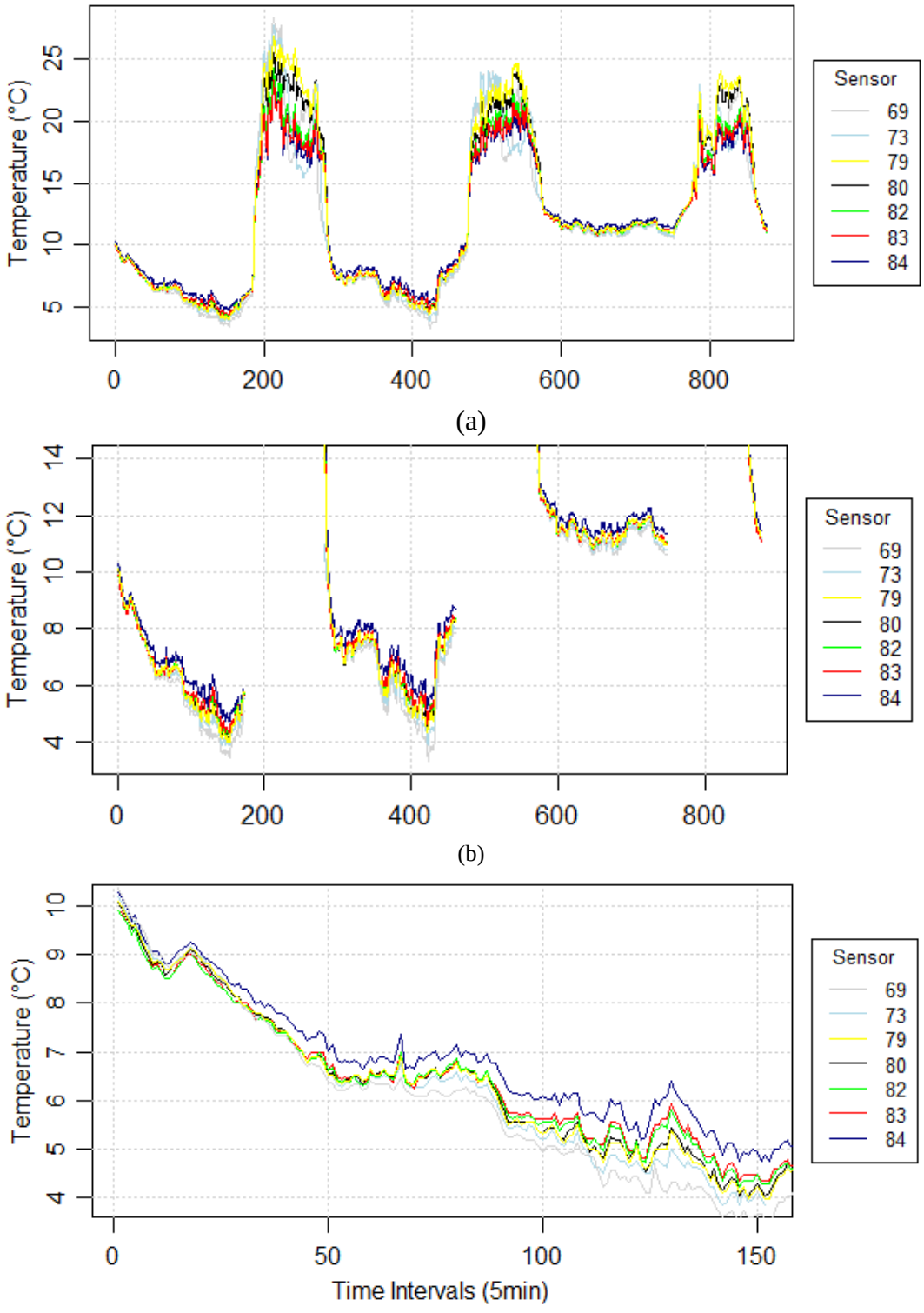

Figure 4.21 The initial (a), the trimmed (b) and the first 150 (c) air temperature sensors readings respectively of the first outdoor experimental test at 40m.

The plots yield evident cyclicality between days and nights. Furthermore it is observed that the vertical temperature gradient sign is mainly negative during the day while it takes positive values during the night as it was expected.

Range	Mean	St. Dev.	n/NA
989.4mbar - 1002.2mbar [12.8mbar]	997.0mbar	±3.8mbar	876/0

Table 4.13 The pressure readings statistics of the first outdoor experimental test at 40m.

The atmospheric pressure readings statistics are introduced in table 4.13 while the pressure time series are illustrated in figure 4.22, where there is an increasing trend during the first day and a decreasing for the rest two days.

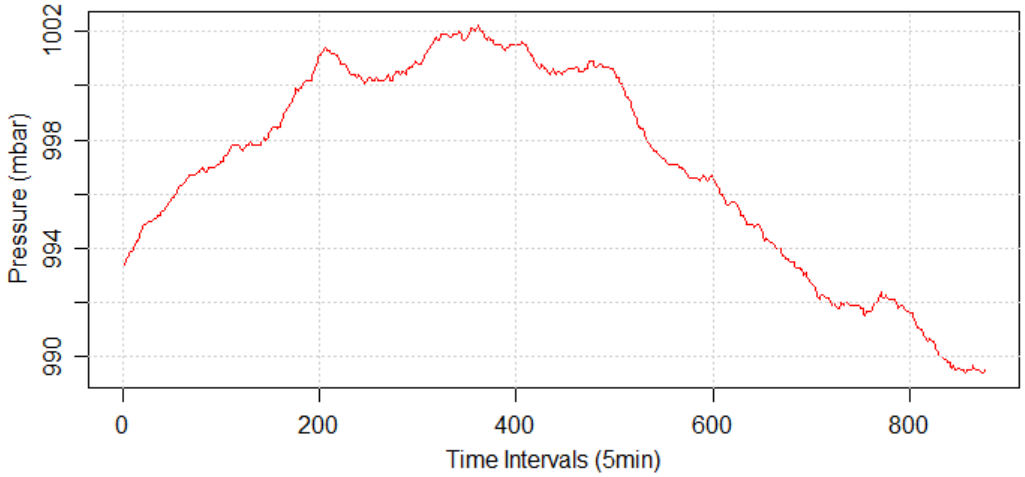

Figure 4.22 The pressure readings time series of the first outdoor experimental test at 40m.

The table 4.14 contains the Pearson correlation coefficients between all the measured values of the discussed dataset. There are not any strong correlations detected except the downhill linear relationship between temperature and distance. The moderate uphill correlation of temperature and height is because of their decreasing trend.

	Height	Distance	Temperature (80)	Pressure
Height	1.00	-0.37	0.46	-0.05
Distance	-0.37	1.00	-0.71	0.32
Temperature (80)	0.46	-0.71	1.00	-0.60
Pressure	-0.05	0.32	-0.60	1.00

Table 4.14 The Pearson correlation coefficients of the measured values of the first outdoor experimental test at 40m.

4.2.4. Second Outdoor Set up at 40m

Since there were considerable gaps in the height readings time series due to weather conditions the outdoor experimental test was re-performed. The DNA03 readings of the second outdoor experimental test started at 2018-01-04 19:25:00 and ended at 2018-01-08 23:50:00, which corresponds to a total period of 4 days, 4 hours and 35 minutes with minor gaps.

The height readings statistics, as they were finally trimmed, are presented in table 4.15. The instrument height was set and measured at 1.657m, which in accordance to the mean values of table 4.15 the rooftop's inclination is calculated at -0.6‰.

DNA Reading	Range	Mean	St. Dev.	n/NA
Height	1.63286m - 1.63406m [1.200mm]	1.633589m	±151μm	1206/440
Distance	37.930m - 37.976m [46mm]	37.949m	±6mm	1206/440

Table 4.15 The digital level's reading statistics for the second outdoor experimental test at 40m.

The following figure 4.23 demonstrates the height readings of the digital level for the second outdoor experimental test. The trimmed parts of the height readings time series are again plotted with red color. Moreover the height readings trend-line apparently shows cyclicality and an incrementing tendency.

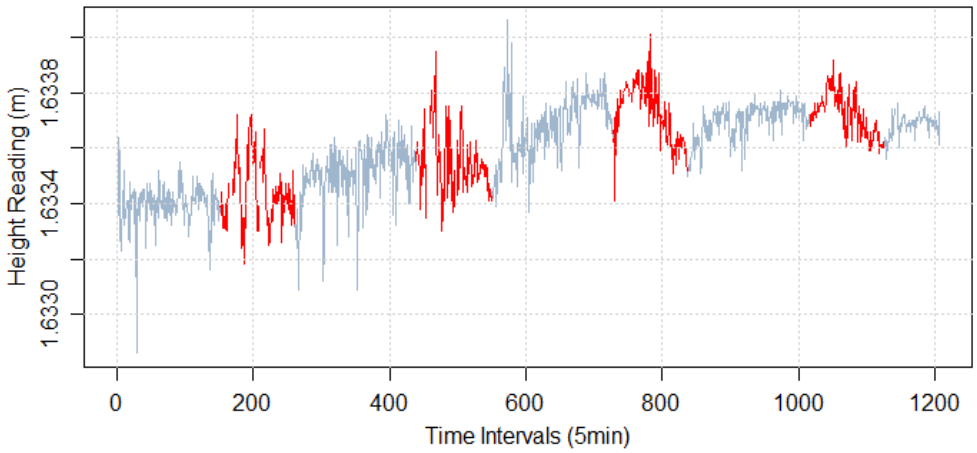

Figure 4.23 The height readings and the trimmed parts (red color) of the second outdoor experimental test as a line.

Additionally figure 4.24 presents as much as the initial as the trimmed height readings distribution with red and grey color respectively. The number of the readings (N) and the smoothing bandwidth are referred to the trimmed readings. These two kernel density plots indicate that there are two to three main values contained in the data.

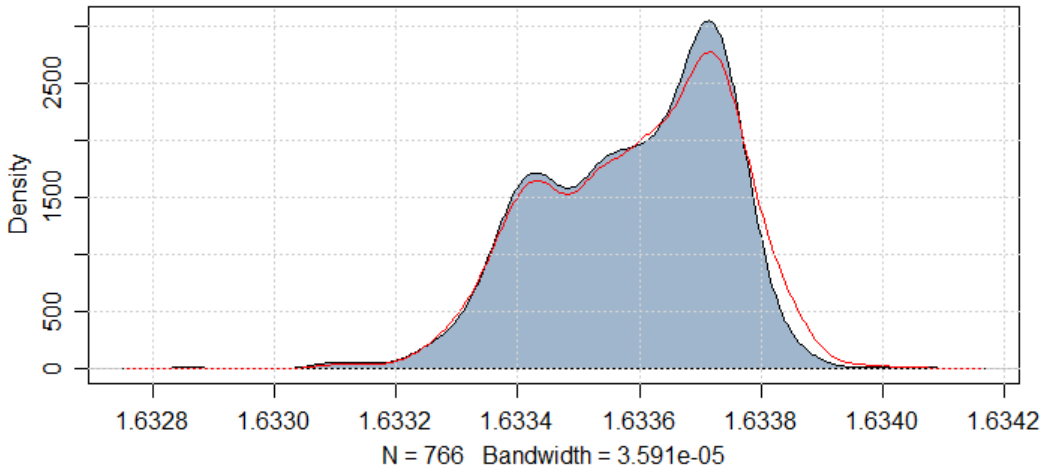

Figure 4.24 The initial (red color) and the trimmed (grey color) height readings distribution of the second outdoor experimental test at 40m via a kernel density plot.

Subsequently, table 4.16 contains the 8 air temperature sensors readings statistics of the second outdoor experimental test as well as the height above the rooftop floor that they were mounted on the bar-coded invar staff.

Sensor	Range	Mean	St. Dev.	n/NA	Height
69	3.79°C - 14.55°C [10.76°C]	9.08°C	±2.63°C	1206/437	0.11m
73	4.11°C - 14.55°C [10.44°C]	9.29°C	±2.54°C	1206/437	0.49m
79	4.22°C - 15.39°C [11.17°C]	9.42°C	±2.56°C	1206/437	0.92m
80	4.16°C - 16.99°C [12.83°C]	9.46°C	±2.57°C	1206/437	1.35m
82	4.22°C - 15.98°C [11.77°C]	9.46°C	±2.44°C	1206/437	2.20m
83	4.22°C - 15.71°C [11.50°C]	9.49°C	±2.44°C	1206/437	2.64m
84	4.61°C - 15.62°C [11.00°C]	9.79°C	±2.34°C	1206/437	3.06m

Table 4.16 The air temperature readings statistics of the second outdoor experimental test at 40m.

The three plots demonstrated in figure 4.25 represent the sensors temperature readings as they were initially acquired (figure 4.25 (a)), as they were finally trimmed (figure 4.25 (b)) and a zoom in the first 150 observations (figure 4.25 (c)). As much as the cyclicality as well as the temperature gradient's sign between the day (-) and the night (+) can easily be noticed in the following charts.

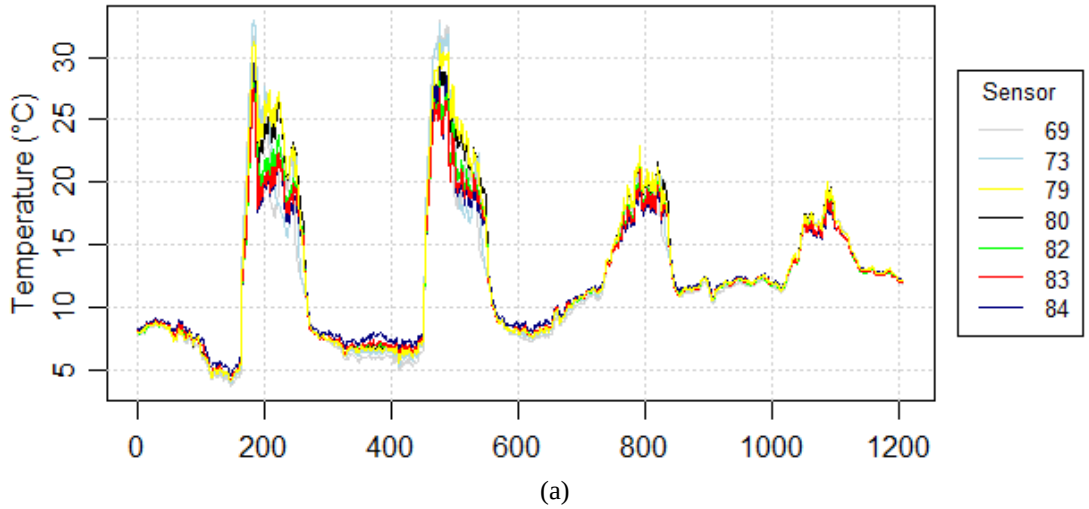

(a)

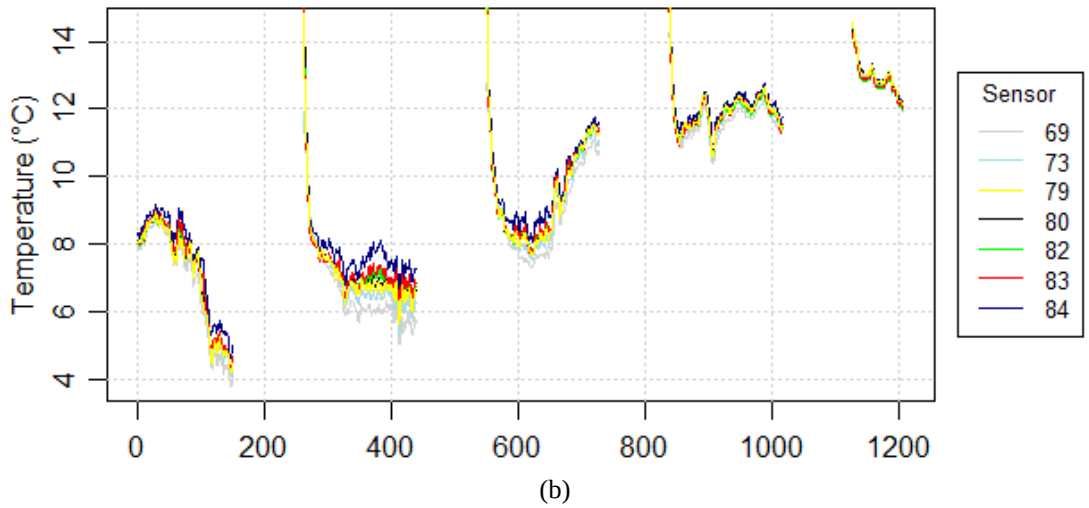

(b)

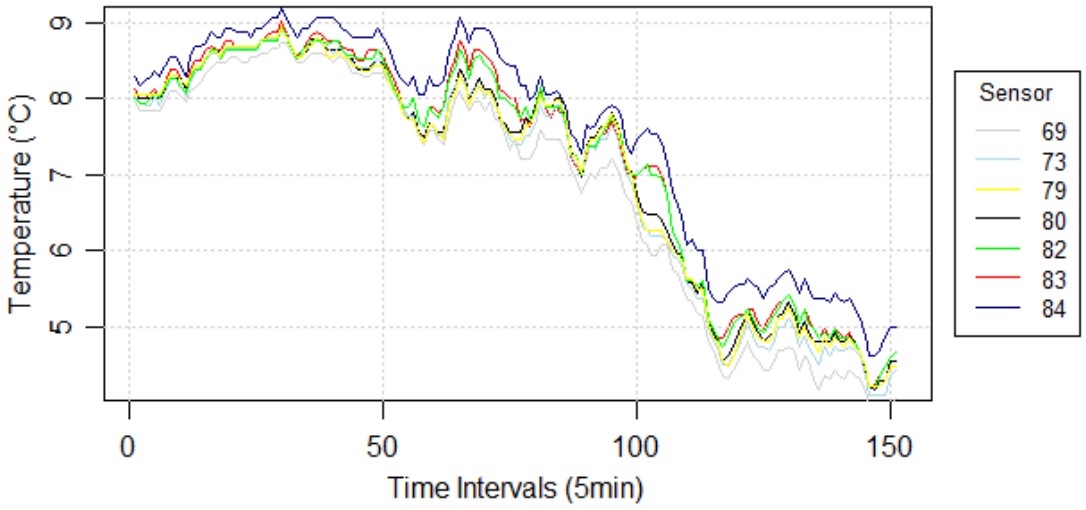

(c)

Figure 4.25 The initial (a), the trimmed (b) and the first 150 (c) air temperature sensors readings respectively of the second outdoor experimental test at 40m.

Table 4.17 contains the atmospheric pressure measurements statistics as they were acquired and converted to the rooftop's altitude.

Range	Mean	St. Dev.	n/NA
988.0mbar - 1012.7mbar [24.8mbar]	1002.9mbar	±6.7mbar	1206/0

Table 4.17 The pressure readings statistics of the second outdoor experimental test at 40m.

Additionally figure 4.26 represents the pressure readings where an upward trend is observed.

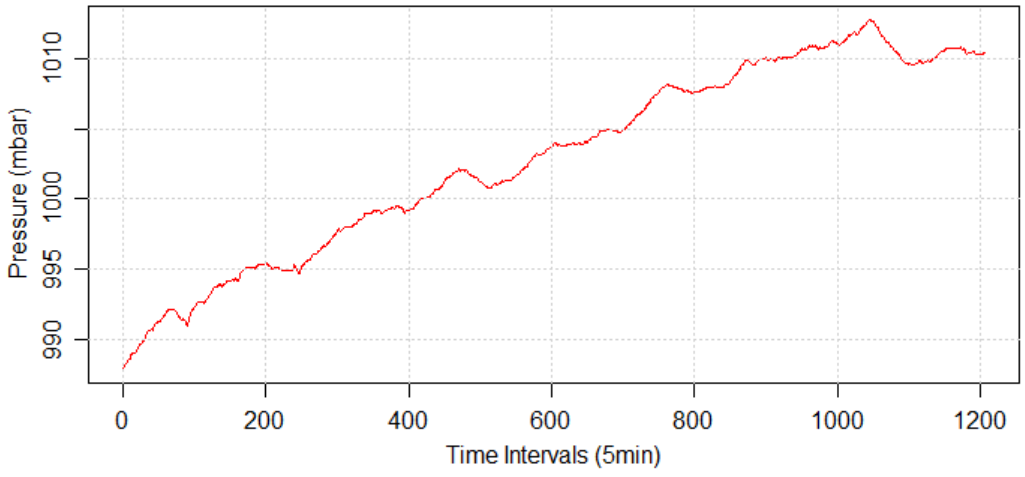

Figure 4.26 The pressure readings time series of the second outdoor experimental test at 40m.

The incrementing trends of the measured parameters, that have been noted earlier, explain the strong and moderate Pearson correlations values that occurred in table 4.18 as well as the uphill linear relationships between height, pressure and temperature.

	Height	Distance	Temperature (80)	Pressure
Height	1.00	-0.36	0.55	0.79
Distance	-0.36	1.00	-0.68	-0.52
Temperature (80)	0.55	-0.68	1.00	0.77
Pressure	0.79	-0.52	0.77	1.00

Table 4.18 The Pearson correlation coefficients of the measured values of the second outdoor experimental test at 40m.

4.3 Temperature Height Models Evaluation

There were 5 vertical temperature height models selected in order to fit the temperature measurements and compute the temperature gradient at the corresponding height reading among the discussed models of section 2.7.4.

These models are the Kukkamaki's temperature height function (eq. 2.49), the Huggershoff's (eq. 2.50), the Reissmann's 1 and 2 (eq. 2.51 and 2.52) and Heer's (eq. 2.54). Karaghani's model was not used since it is an alteration of Kukkamaki's model. As it has already been denoted polynomials greater than second degree fail to work properly.

Even though, the model Reissmann 2 was selected because it has the ability to adopt one inflection point with respect to the fitted data. The following equations demonstrate the first derivative of models that were used to compute the temperature gradient.

Kukkamaki $$\frac{dt}{dz} = b \cdot c \cdot z^{c-1} \quad (4.3)$$

Huggershoff $$\frac{dt}{dz} = 2 \cdot b \cdot z \quad (4.4)$$

Reissmann1 $$\frac{dt}{dz} = b + 2 \cdot c \cdot z \quad (4.5)$$

Reissmann2 $$\frac{dt}{dz} = b + 2 \cdot c \cdot z + 3 \cdot f \cdot z^2 \quad (4.6)$$

Heer $$\frac{dt}{dz} = b \cdot c \cdot e^{c \cdot z} \quad (4.7)$$

The fit of the data was accomplished by using nonlinear regression, which is initially evaluated optically by visualizing the data. The estimation of the parameters was tested in order to be greater than their standard errors, which corresponds to a statistical test for a confidence level of 68%.

Additionally a t-test could be used but it would force the errors to be enlarged. Thus a "pass" or "fail" value was given accordingly to each model for every time interval.

Moreover the goodness of fit is evaluated by the use of the residual standard error (σ) of every regression, which is affected by the degrees of freedom meaning that Reissmann2 model is expected to succeed higher values while Huggershoff model lower.

The σ value has to be close to the measuring accuracy of the air temperature sensors otherwise when the σ is much greater, then the goodness of fit is poor and when it is less, then the fit is not realistic (overfitting).

4.3.1 Indoor Experimental Test at 25m

Table 4.19 indicates a summary for the goodness of fit of the 5 temperature height models and the air temperature measurements of the first indoor experimental test at 25m. The following table represents the percentage of the pass values per model and the mean residual standard error (σ).

Model	Pass	σ
Kukkamaki	100%	±0.15°C
Huggershoff	100%	±0.18°C
Reissmann1	0%	±0.18°C
Reissmann2	100%	±0.14°C
Heer	100%	±0.15°C

Table 4.19 Summary of the goodness of fit of the 5 models and the indoor experimental test at 25m.

As it is demonstrated above the Huggershoff and the Reissmann1 models had the poorest data fit while Reissmann1 model failed the statistical test of the parameters. Figure 4.27 illustrates a screenshot of the fitted models and the measured temperatures and particularly at the 100 time interval.

The graphical examination of the models does not indicate a function that fit the data better. Kukkamaki, Reissmann1 and Heer models demonstrate a concave shape while Huggershoff has a convex shape and Reissmann2 has an inflection point.

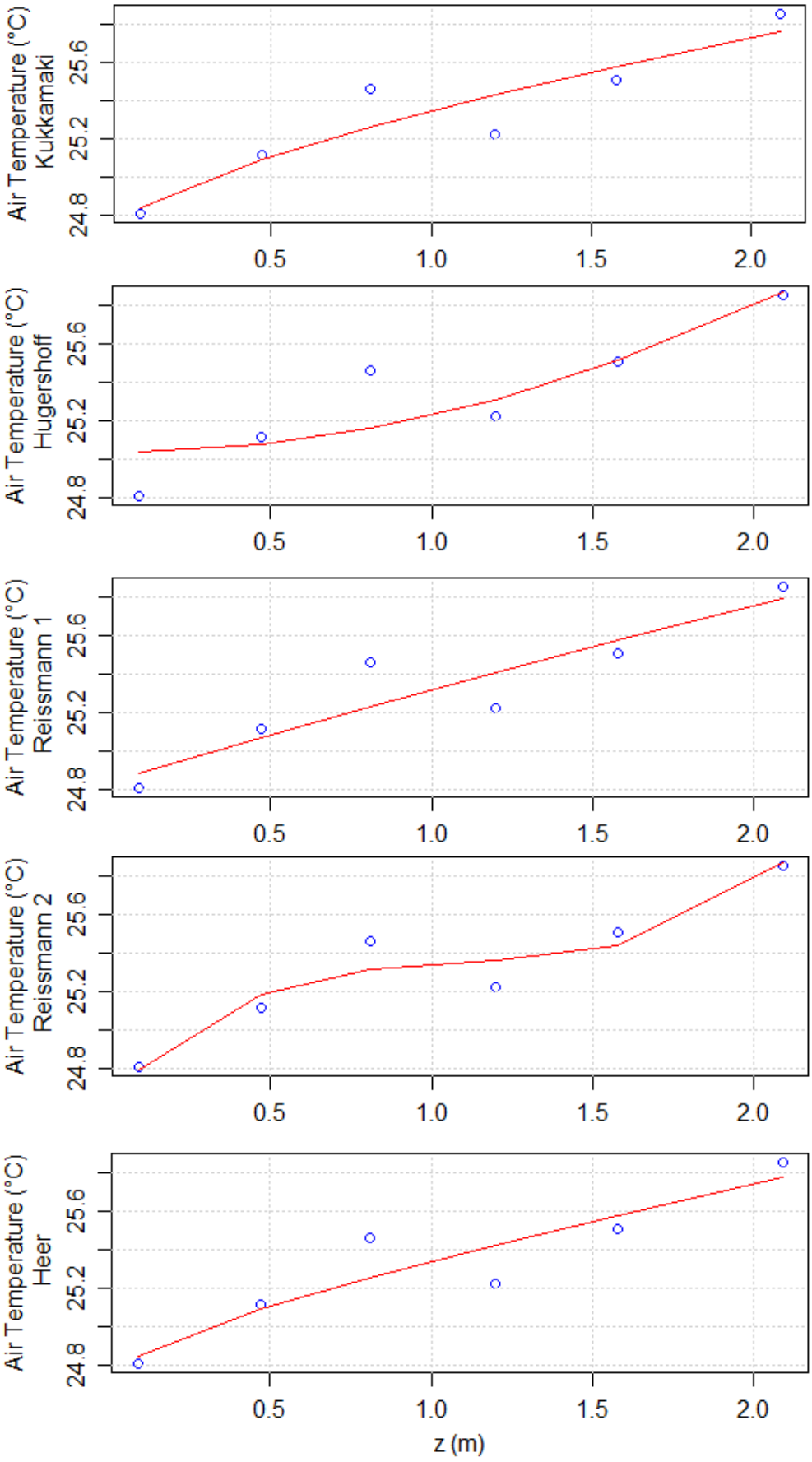

Figure 4.27 The fitted temperature height models at the 100 time interval of the indoor experimental test at 25m.

The following figure 4.28 shows the residual standard error along the time intervals.

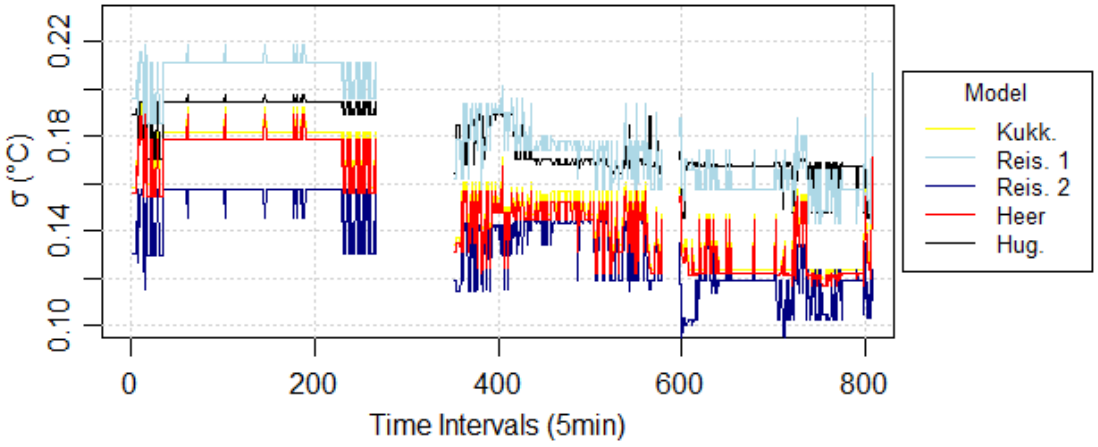

Figure 4.28 The residual standard error of the fitted models for the indoor experimental test at 25m.

Table 4.20 and figure 4.29 represent the statistics and the visualization of the temperature gradient respectively, by using the first derivative of the temperature height functions. In general the temperature gradient is positive.

Model	Range	Mean	St. Dev.
Kukkamaki	0.35 - 0.47°C·m^{-1}	0.40°C·m^{-1}	±0.02°C·m^{-1}
Huggershoff	0.45 - 0.55°C·m^{-1}	0.50°C·m^{-1}	±0.02°C·m^{-1}
Reissmann1	0.36 - 0.49°C·m^{-1}	0.40°C·m^{-1}	±0.03°C·m^{-1}
Reissmann2	0.09 - 0.26°C·m^{-1}	0.19°C·m^{-1}	±0.04°C·m^{-1}
Heer	0.23 - 0.36°C·m^{-1}	0.27°C·m^{-1}	±0.02°C·m^{-1}

Table 4.20 The temperature gradient statistics of the fitted models for the indoor experimental test at 25m.

The temperature gradient amplitude differences between the models occurred because of the regression's sensitivity among the 5 functions.

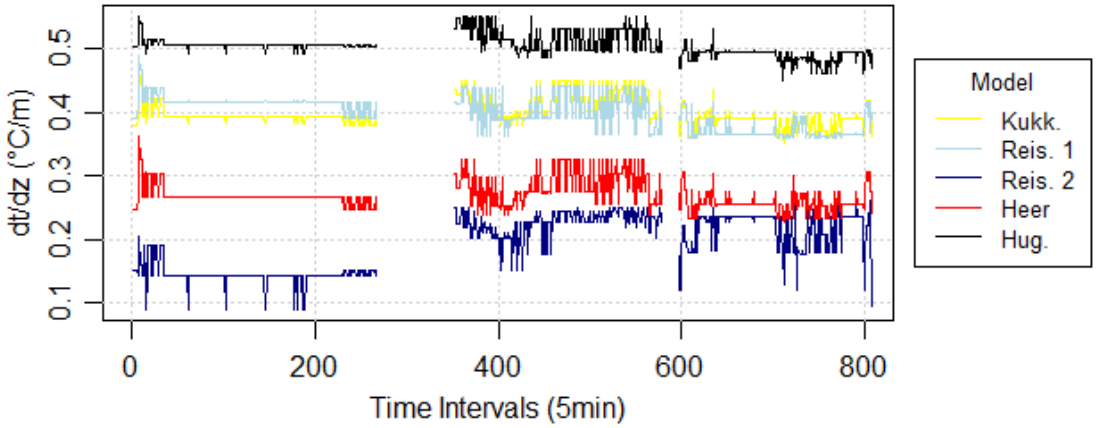

Figure 4.29 The temperature gradient of the fitted models for the indoor experimental test at 25m.

4.3.2 Indoor Experimental Test at 50m

Table 4.21 shows a summary of the goodness of fit measures of the 5 temperature height models with respect to the air temperature measurements of the indoor experimental test at 50m. Kukkamaki's height function did not manage to fit the data and converge.

Model	Pass	σ
Kukkamaki	0%	-
Huggershoff	100%	±0.12°C
Reissmann1	30%	±0.13°C
Reissmann2	100%	±0.04°C
Heer	0%	±0.14°C

Table 4.21 Summary of the goodness of fit of the 5 models and the indoor experimental test at 50m.

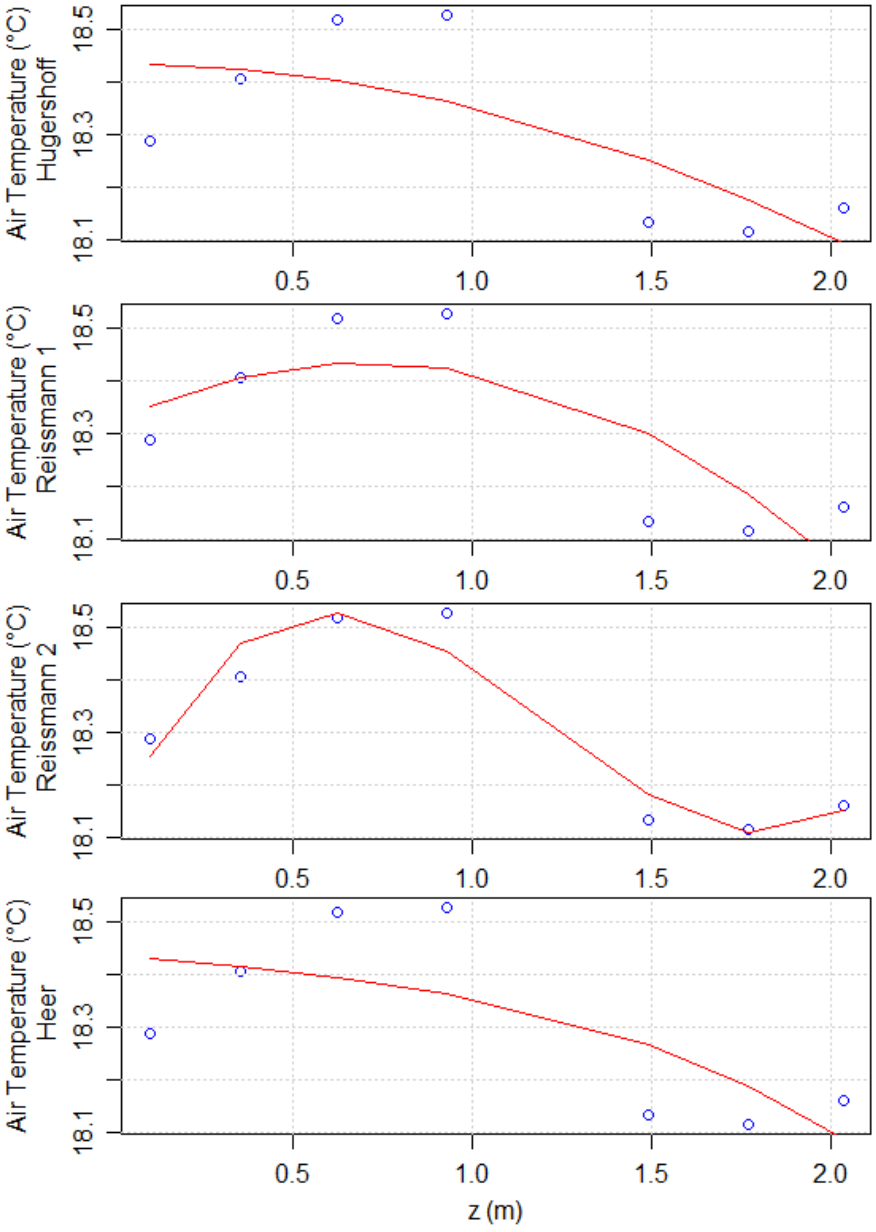

Figure 4.30 The fitted temperature height models at the 100 time interval of the indoor experimental test at 50m.

Moreover Heer's model failed to pass the test, while Reissmann 1 model failed to pass it at the majority of the measurements. The model Reissmann 2 seems to overfitting the data. The above figure 4.30 illustrates a screenshot of the air temperature measurements (at the 100 time interval) by using blue points and the fitted models by red lines.

This visual examination of the displayed fitted curves yields concave shapes except the Reissmann 2 model. Additionally all the models show a decreasing trend. The following figure 4.31 presents the residual standard error of the least squares data fitting among the models and along the time intervals.

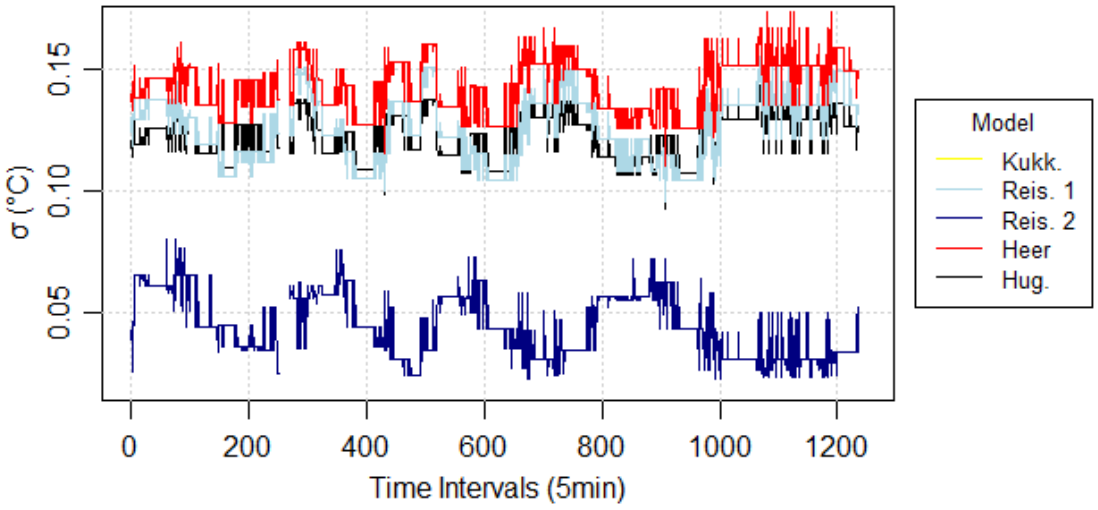

Figure 4.31 The residual standard error of the fitted models for the indoor experimental test at 50m.

Table 4.22 and figure 4.32 represent the statistics and the visualization of the temperature gradient respectively, by using the first derivative of the temperature height functions. Generally the temperature gradient is negative with respect to the mean height of the level's sighting line.

Model	Range	Mean	St. Dev.
Kukkamaki	-	-	-
Huggershoff	-0.23 - -0.15°C·m^{-1}	-0.20°C·m^{-1}	±0.01°C·m^{-1}
Reissmann1	-0.23 - -0.15°C·m^{-1}	-0.20°C·m^{-1}	±0.01°C·m^{-1}
Reissmann2	-0.67 - -0.45°C·m^{-1}	-0.54°C·m^{-1}	±0.05°C·m^{-1}
Heer	-0.21 - -0.18°C·m^{-1}	-0.18°C·m^{-1}	±0.01°C·m^{-1}

Table 4.22 The temperature gradient statistics of the fitted models for the indoor experimental test at 50m.

Thus, the temperature gradient amplitude differences between Reissmann2 and the other models occurred because of the slope variation at this particular height and due to the data overfitting.

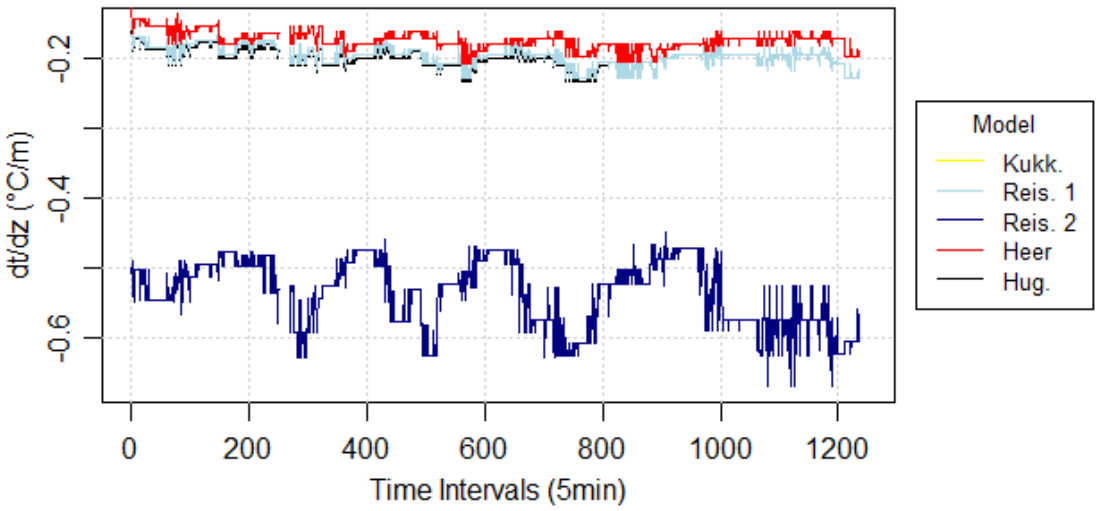

Figure 4.32 The temperature gradient of the fitted models for the indoor experimental test at 50m.

4.3.3 First Outdoor Experimental Test at 40m

Table 4.23 demonstrates the numerical statistics of the goodness of fit for the 5 temperature height models with respect to the air temperature measurements of the first outdoor experimental test at 40m.

Again, Huggershoff's and Reissmann's 2 models achieve the most passes on the statistical test of the parameters. Moreover the Reisssmann's 2 function seems to have the best fitting statistics but it is once again possible for overfitting the data.

Model	Pass	σ
Kukkamaki	21%	±0.14°C
Huggershoff	73%	±0.17°C
Reissmann1	20%	±0.15°C
Reissmann2	77%	±0.08°C
Heer	23%	±0.15°C

Table 4.23 Summary of the goodness of fit of the 5 models and the first outdoor experimental test at 40m.

Figure 4.33 illustrates a screenshot of the air temperature measurements at the 100 time interval. This visual examination of the displayed fitted curves indicates that Reissmann2 model achieves the best least square fitting. The other 4 temperature height curves form a convex shape with increasing trend.

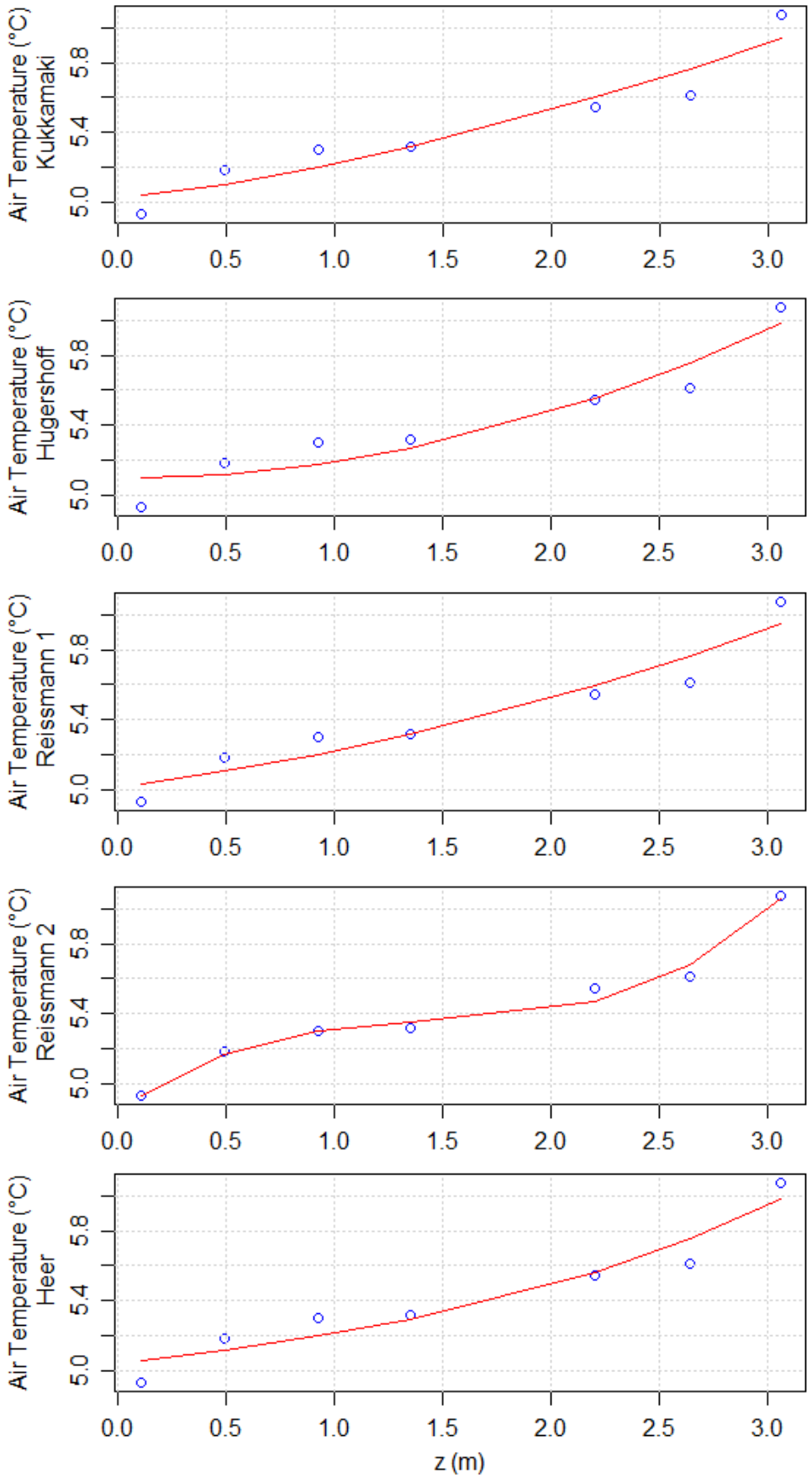

Figure 4.33 The fitted temperature height models at the 100 time interval of the first outdoor experimental test at 40m.

The following figure 4.34 shows the residual standard error of the least squares data fitting and the correlation coefficient over time and among the models.

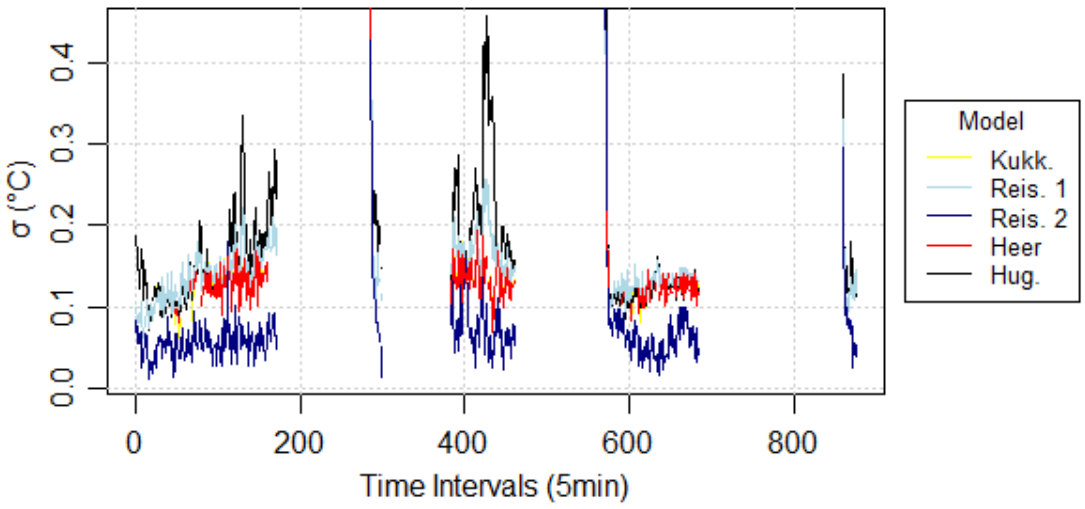

Figure 4.34 The residual standard error of the fitted models for the first outdoor experimental test at 40m.

Table 4.24 and figure 4.35 present the statistics and the visualization of the temperature gradient respectively. In general, the temperature gradient is positive with respect to the height of the level's telescope. The negative values of the temperature gradient were due to data trimming failure and occurred just after sunset and before sunrise.

Model	Range	Mean	St. Dev.
Kukkamaki	-0.01 - 0.76°C·m^{-1}	0.22°C·m^{-1}	±0.13°C·m^{-1}
Huggershoff	-0.06 - 1.36°C·m^{-1}	0.20°C·m^{-1}	±0.1°C·m^{-1}6
Reissmann1	-0.38 - 4.69°C·m^{-1}	0.32°C·m^{-1}	±0.46°C·m^{-1}
Reissmann2	-0.28 - 0.95°C·m^{-1}	-0.03°C·m^{-1}	±0.14°C·m^{-1}
Heer	-0.01 - 0.71°C·m^{-1}	0.17°C·m^{-1}	±0.11°C·m^{-1}

Table 4.24 The temperature gradient statistics of the fitted models for the first outdoor experimental test at 40m.

Hence, the range of Reissmann1 model is an outlier since the sensors could not compensate the temperature decrease which happened just after sunset. The overfitting of Reissmann2 model is obvious at the part of the time series around the 600 time interval.

At this period the temperature gradient had low values, which were not readable by the sensors measuring accuracy. Thus, the interpolation was computed close to the inflection point of the curve and so negative values appeared.

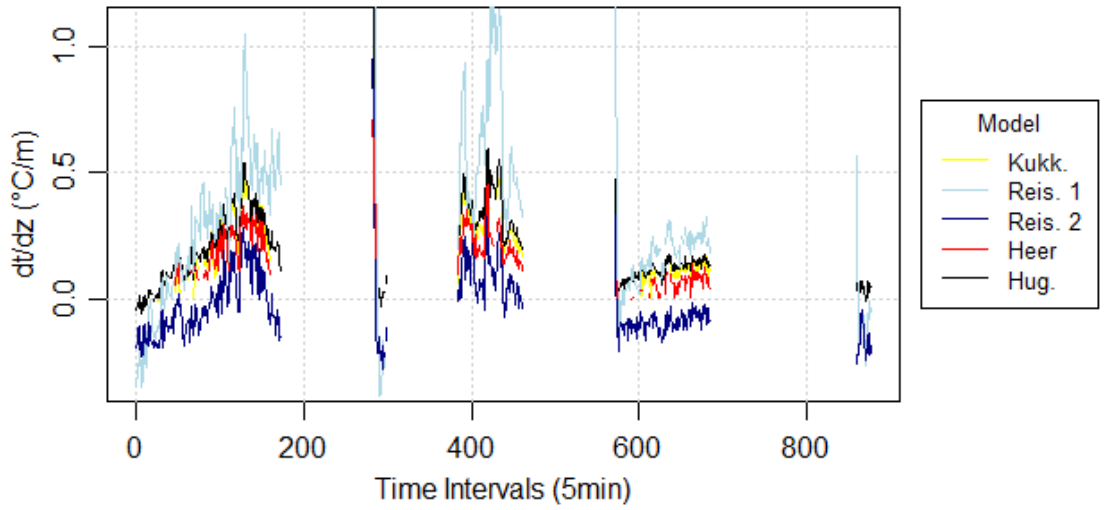

Figure 4.35 The temperature gradient of the fitted models for the first outdoor experimental test at 40m.

4.3.4 Second Outdoor Experimental Test at 40m

Table 4.25 presents the numerical measures of the goodness of fit for the 5 temperature height models with respect to the air temperature measurements of the second outdoor experimental test at 40m.

Again, Huggershoff's and Reissmann's 2 models achieve the most passes on the statistical test of the parameters. Despite the fact that Reisssmann's 2 model seems to have the best fitting statistics it is once again overfitting the data.

Model	Pass	σ
Kukkamaki	19%	±0.14°C
Huggershoff	85%	±0.16°C
Reissmann1	37%	±0.13°C
Reissmann2	90%	±0.06°C
Heer	21%	±0.13°C

Table 4.25 Summary of the goodness of fit of the 5 models and the second outdoor experimental test at 40m.

Figure 4.36 shows a screenshot of the air temperature measurements at the 100 time interval along with the fitted models. This visual examination of the displayed fitted curves is not able to distinguish the best least square fitting model. Generally the temperature height trendlines form a convex shape with increasing tendency.

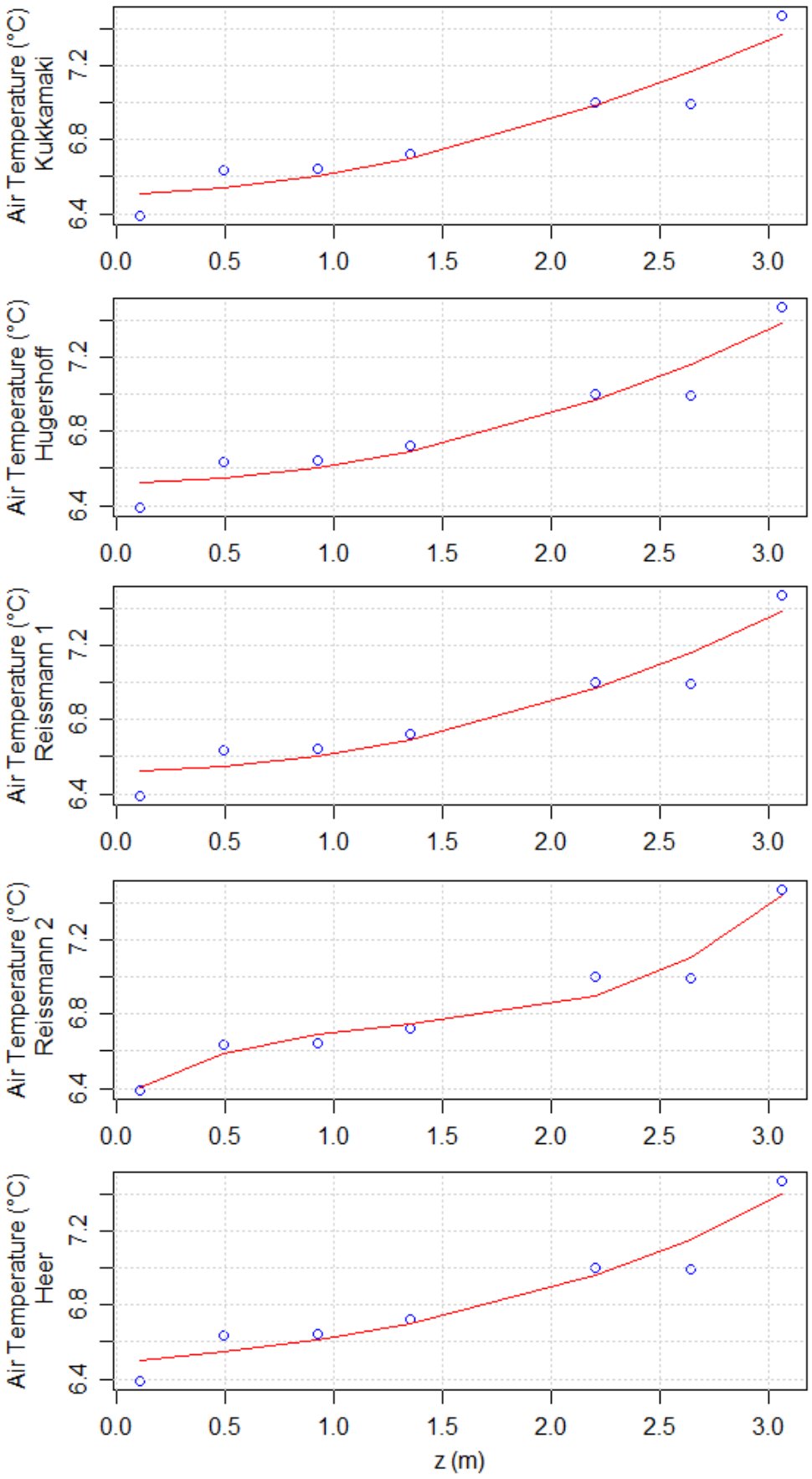

Figure 4.36 The temperature gradient of the fitted models for the second outdoor experimental test at 40m.

Additionally figure 3.37 represents the residual standard error of the models for every time interval.

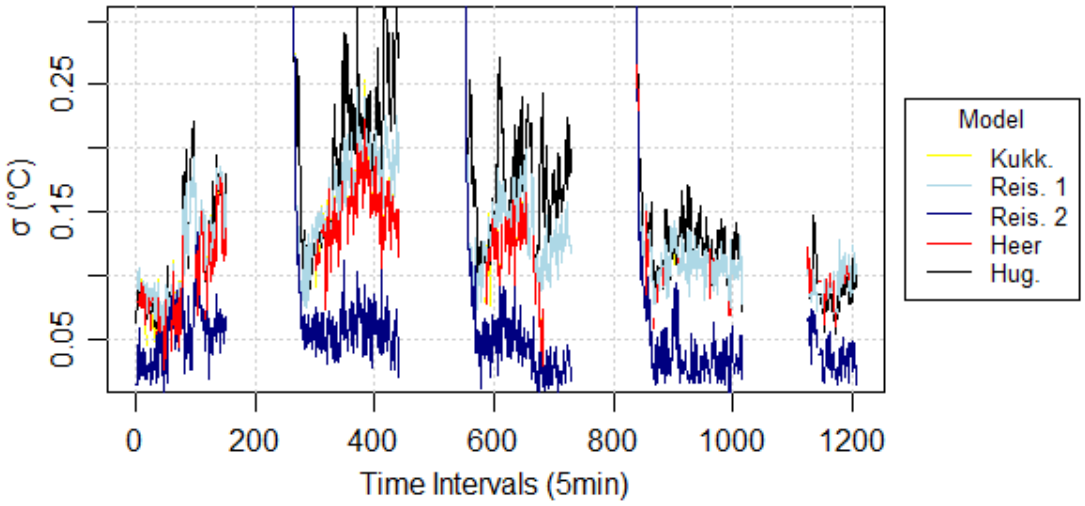

Figure 4.37 The correlation coefficient of the fitted models between the measured and the predicted values for the second outdoor experimental test at 40m.

Table 4.26 and figure 4.38 display the numerical statistics and the graphical visualization of the temperature gradient respectively. In general, the temperature gradient is positive with respect to the height of the level's telescope.

Model	Range	Mean	St. Dev.
Kukkamaki	-0.10 - 0.92	0.22	0.14
Huggershoff	-0.06 - 1.04	0.21	0.14
Reissmann1	-0.10 - 1.20	0.17	0.15
Reissmann2	-0,30 - 1.06	-0.05	0.12
Heer	-0.08 - 0.56	0.15	0.11

Table 4.26 The temperature gradient statistics of the fitted models for the second outdoor experimental test at 40m.

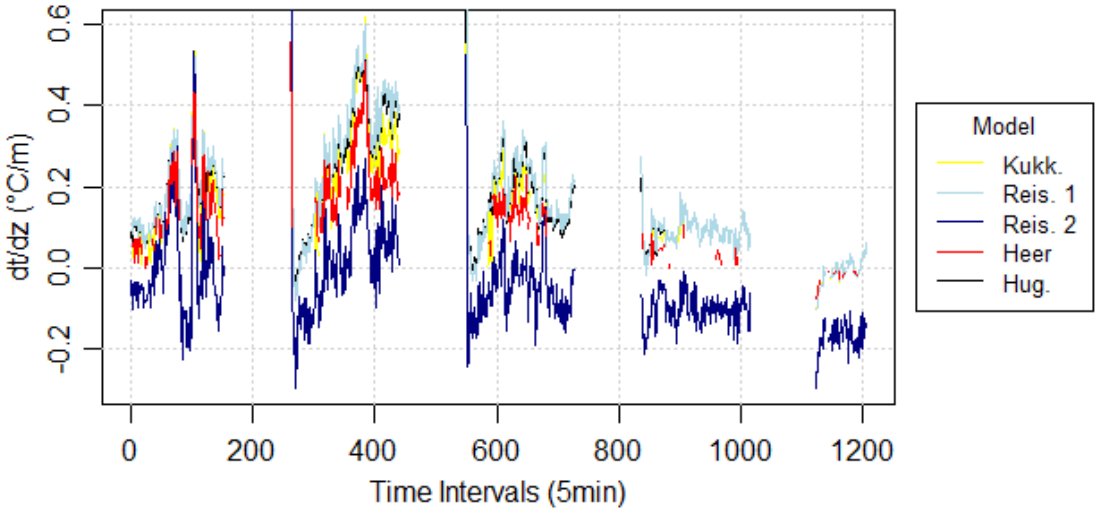

Figure 4.38 The fitted temperature height models at the 100 time interval of the second outdoor experimental test at 40m.

The negative mean value of the temperature gradient of the Reissmann2 model is due to overfitting and is obvious especially after the 400 time interval. This happens because the temperature gradient becomes smaller over time and gets values that are close to the measuring accuracy of the air temperature sensors.

4.4 Refraction Corrections Results

The levelling refraction corrections were computed by using the Kukkamaki's approach and equation 2.42 as it was pre-discussed on chapter 2. Thus, by integrating the temperature difference between the level and the staff with respect to the selected temperature height models, the following refraction correction equations hold:

Kukkamaki
$$C_R = -\frac{d \cdot s^2 \cdot b}{(z_b - z_I)^2} \cdot \left[\frac{1}{c+1} \cdot z_b^{c+1} - z_I^c \cdot z_b + \frac{c}{c+1} \cdot z_I^{c+1}\right] \tag{4.8}$$

Huggershoff
$$C_R = -\frac{d \cdot s^2 \cdot b}{(z_b - z_I)^2} \cdot \left[\frac{z_b^3}{3} - z_I^2 z_b + \frac{2 \cdot z_I^3}{3}\right] \tag{4.9}$$

Reiss.1
$$C_R = -\frac{d \cdot s^2}{(z_b - z_I)^2} \cdot \begin{bmatrix} -z_I \cdot z_b \cdot (b + c \cdot z_I) + \frac{b \cdot z_b^2}{2} + \frac{c \cdot z_b^3}{3} \\ +z_I^2 \cdot (b + c \cdot z_I) - \frac{b \cdot z_I^2}{2} - \frac{c \cdot z_I^3}{3} \end{bmatrix} \tag{4.10}$$

Reiss.2
$$C_R = -\frac{d \cdot s^2}{(z_b - z_I)^2} \cdot \begin{bmatrix} \left(-\frac{1}{12} z_b \left(12 z_I \left(b + z_I (c + f z_I)\right) - 6 b z_b - 4 c z_b^2 - 3 f z_b^3\right)\right) \\ -\left(-\frac{1}{12} Z_I \left(12 z_I \left(b + z_I (c + f z_I)\right) - 6 b z_I - 4 c z_I^2 - 3 f z_I^3\right)\right) \end{bmatrix} \tag{4.11}$$

Heer
$$C_R = -\frac{d \cdot s^2 \cdot b}{(z_b - z_I)^2} \cdot \left[\frac{e^{c \cdot z_b}}{c} - z_b \cdot e^{c \cdot z_I} - \frac{e^{c \cdot z_I}}{c} + z_I \cdot e^{c \cdot z_I}\right] \tag{4.12}$$

Then, the refraction corrections can be interpreted and quantified as geodetic refraction coefficient values k, by reforming equation 2.14 as it is demonstrated in equation 4.13. The negative sign of the equation cannot hold since it is not referred to a target position and the correct height reading of the bar code has to be determined with respect to the apparent position.

$$k = \frac{C_R \cdot 2 \cdot R}{s^2} \tag{4.13}$$

In order to follow the above methodology the following assumptions have to be taken under consideration:

- The meteorological conditions are considered stable.

- The scale factor error between the level and the staff as long as the correction due to earth curvature are considered as constants and thus negligible.
- The inclination of the floor is considered constant and that the air is stratified to isothermal layers parallel to it.

For cross reference reasons, the geodetic refraction coefficient k is also calculated by using the local geodetic refraction coefficient k as it was introduced in equation 2.26.

4.4.1 Indoor Experimental Test at 25m

The following table 4.27 represents the refraction corrections statistics among the 5 used temperature height functions of the first indoor experimental test at 25m. The differences occurred in the results is because of the models least square fitting. Additionally figure 4.39 illustrates the refraction corrections of every time interval and model.

Model	Min	Max	Mean	St. Dev.
Kukkamaki	99μm	134μm	113μm	±6μm
Huggershoff	130μm	159μm	146μm	±5μm
Reissmann1	103μm	141μm	115μm	±8μm
Reissmann2	30μm	75μm	57μm	±12μm
Heer	65μm	105μm	78μm	±7μm

Table 4.27 The refraction corrections statistics of the 5 temperature height models and the indoor experimental test at 25m.

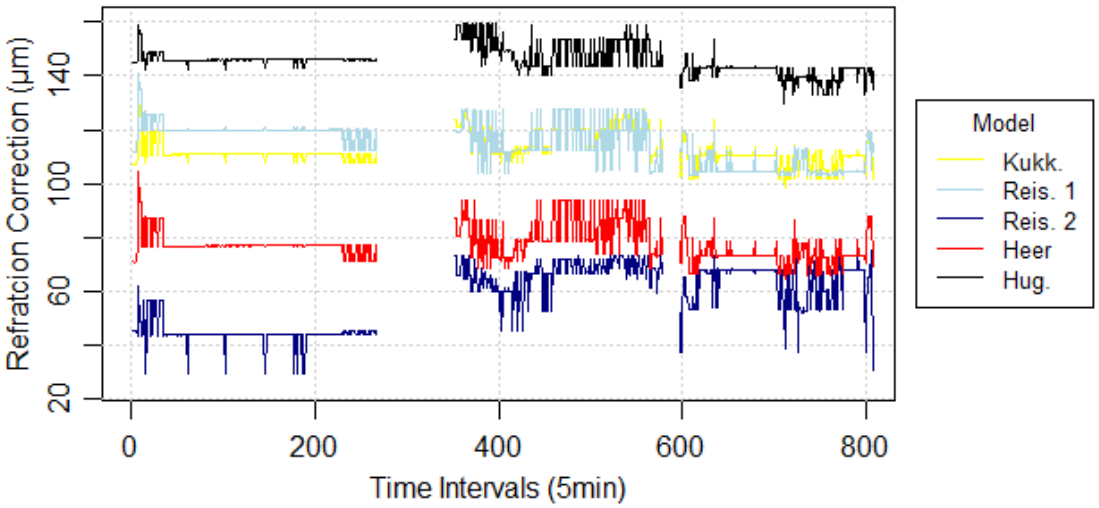

Figure 4.39 The refraction corrections of the 5 temperature height models and the indoor experimental test at 25m.

Figure 4.40 contains the initial height readings as grey line as long as the corrected height readings time series as red lines for the 5 used temperature height functions and the first indoor experimental test at 25m. None of the following charts seems to smooth out the height readings trendline but are just shift them up because of the noise that is included therein the data. Even though, the sign of the corrections is correct.

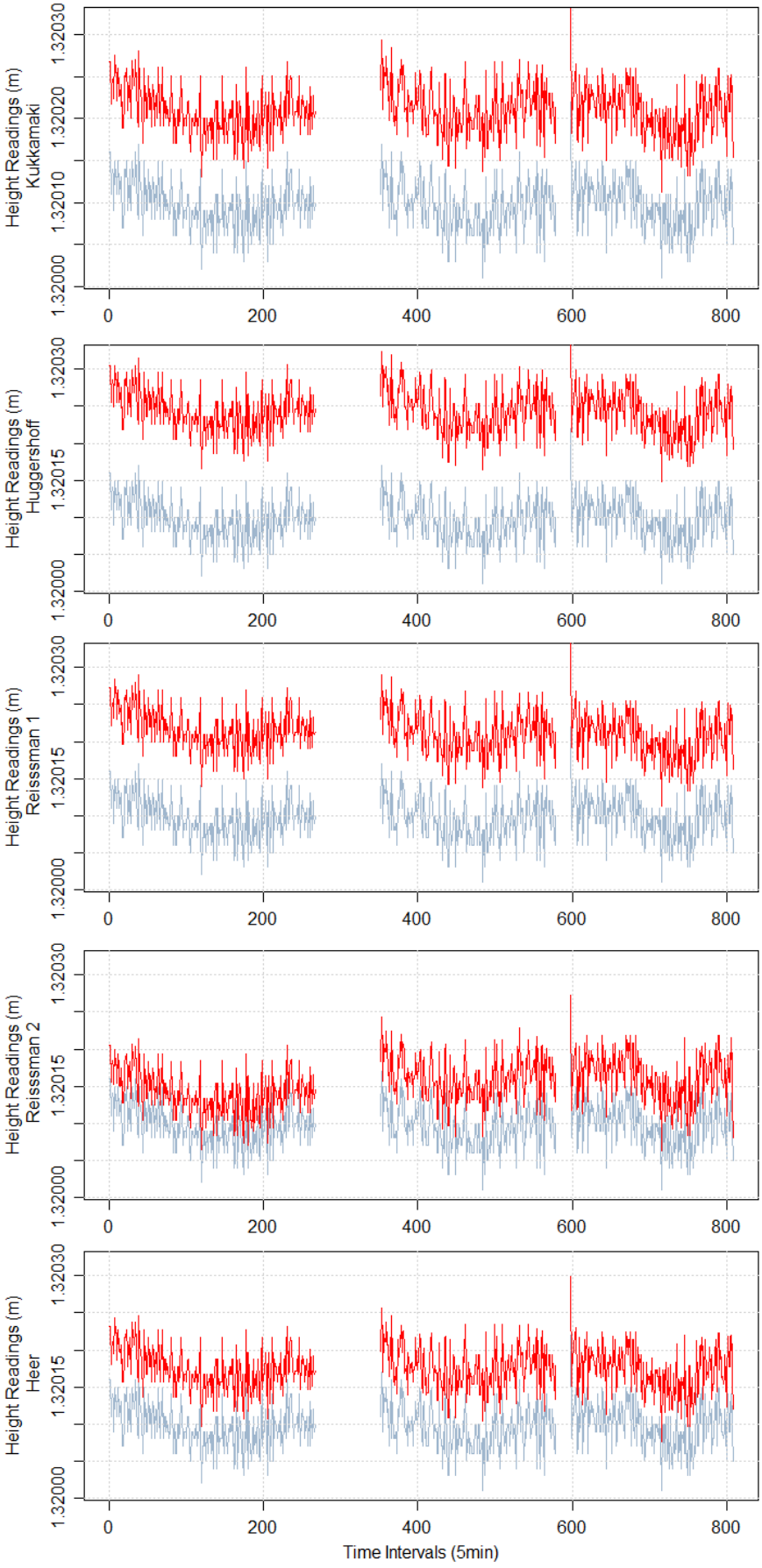

Figure 4.40 The initial (grey lines) and the corrected height readings time series (red lines) of the five temperature height functions and the indoor experimental test at 25m.

Table 4.28 demonstrates the statistics of the interpretation of the refraction corrections as geodetic refraction coefficient values k by using the Kukkamakis approach. Moreover it contains the corresponding statistics of k values by using the local geodetic refraction coefficient equation. The amplitude of the values indicates that the two methods are in agreement while the local values are always slightly bigger.

	k Kukkamaki				k Local			
Model	**Min**	**Max**	**Mean**	**St. Dev.**	**Min**	**Max**	**Mean**	**St. Dev.**
Kukkamaki	1.96	2.67	2.24	±0.12	2.17	2.86	2.44	±0.12
Huggershoff	2.58	3.17	2.90	±0.10	2.73	3.31	3.04	±0.10
Reissmann1	2.05	2.81	2.28	±0.16	2.22	2.96	2.45	±0.15
Reissmann2	0.59	1.50	1.14	±0.24	0.70	1.66	1.27	±0.25
Heer	1.29	2.08	1.55	±0.13	1.14	2.25	1.72	±0.13

Table 4.28 The geodetic refraction coefficient statistics of the 5 temperature height models and the indoor experimental test at 25m.

Additionally figures 4.41 and 4.42 represent graphically the computed values of the geodetic refraction coefficient k between the two methods. The differences of the k values among the two graphs are so small that they cannot be distinguished.

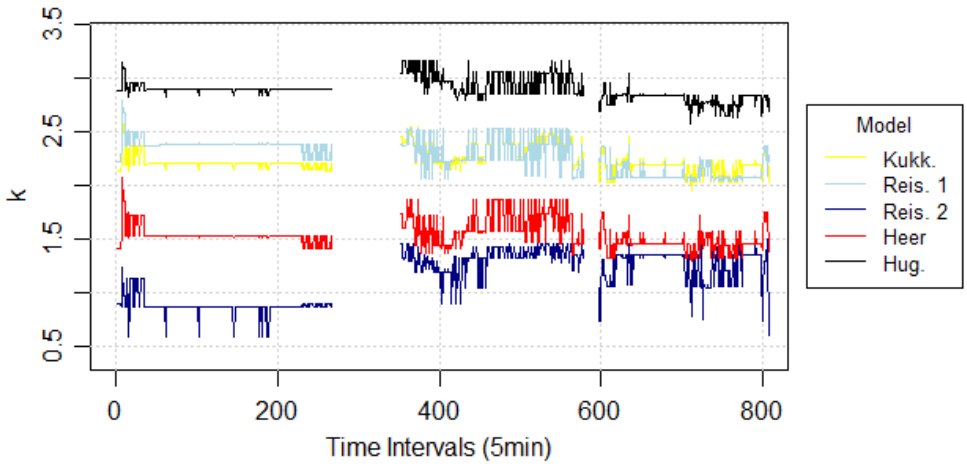

Figure 4.41 The geodetic refraction coefficient of the 5 temperature height models and the indoor experimental test at 25m by using the Kukkamaki's approach.

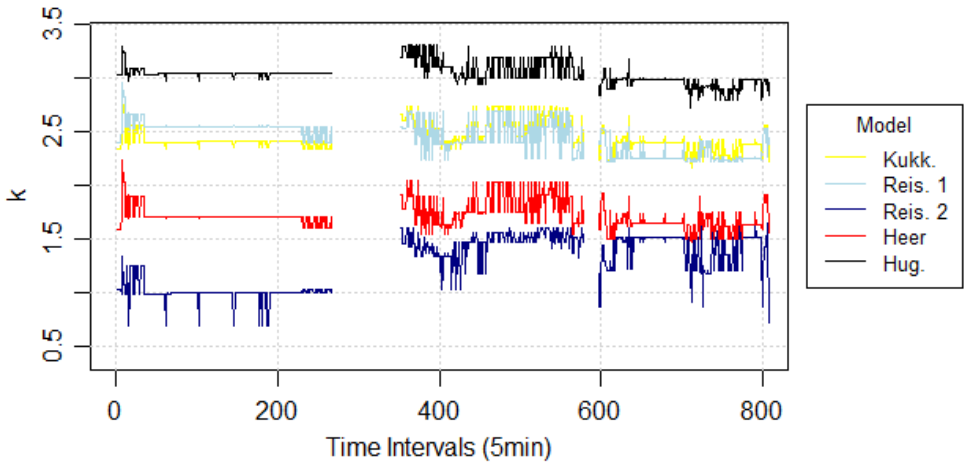

Figure 4.42 The geodetic refraction coefficient of the 5 temperature height models and the indoor experimental test at 25m by using the local geodetic refraction coefficient equation.

4.4.2 Indoor Experimental Test at 50m

Table 4.27 shows the refraction corrections statistics among the 4 selected and used models of the second indoor experimental test at 50m. In general the refraction corrections are negative as it was expected. This happens because of the negative temperature gradient values.

Model	Min	Max	Mean	St. Dev.
Kukkamaki	-	-	-	-
Huggershoff	-295μm	-193μm	-254μm	±18μm
Reissmann1	-315μm	-209μm	-276μm	±18μm
Reissmann2	-755μm	-529μm	-617μm	±46μm
Heer	-266μm	-163μm	-224μm	±17μm

Table 4.29 The refraction corrections statistics of the 4 temperature height models and the indoor experimental test at 50m.

The refraction correction results of Reissmann 2 model are considered as outliers and appear due to data overfitting. The other three models despite the slight differences occurred they appear to be in accordance with each other. Additionally figure 4.43 gathers the refraction corrections results in a single chart.

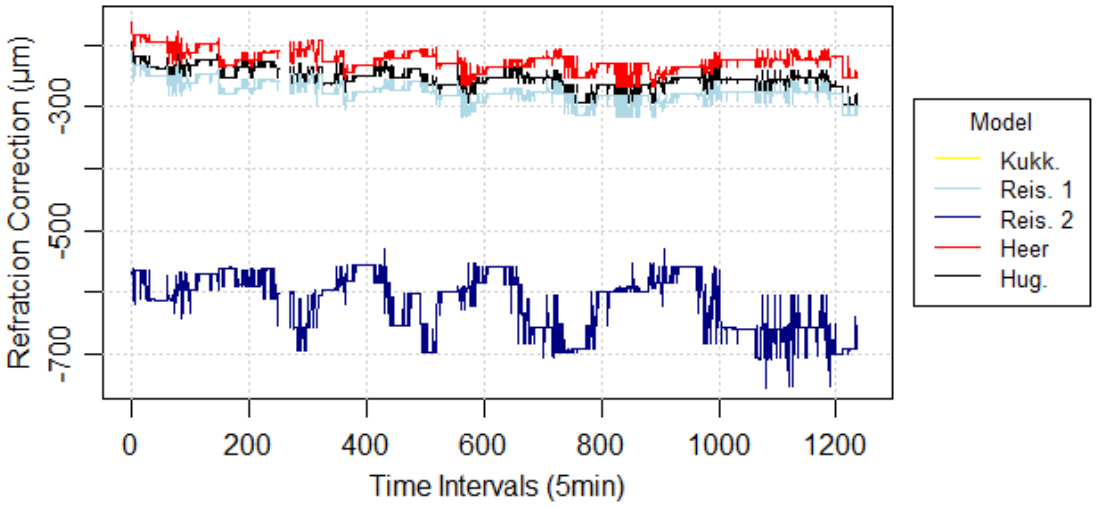

Figure 4.43 The refraction corrections of the 4 temperature height models and the indoor experimental test at 50m.

The charts of figure 4.44 illustrate the initial height readings as grey line as long as the corrected height readings time series as red lines for the 4 used temperature height functions and the second indoor experimental test at 50m. Again, none of the following charts seems to smooth out the height readings trendline but are just shift them down.

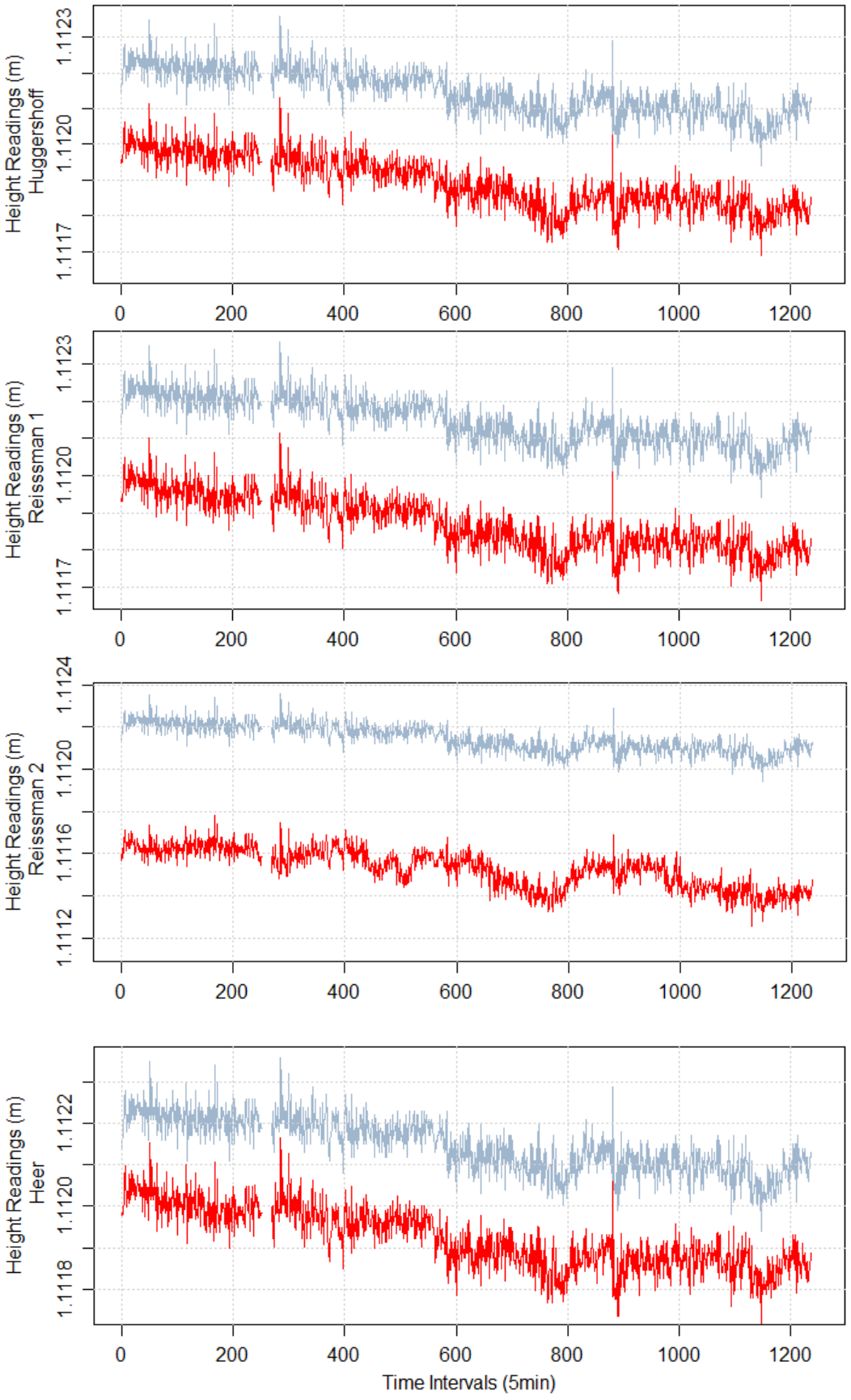

Figure 4.44 The initial height readings (grey lines) and the corrected height readings time series (red lines) of the 4 temperature height functions and the indoor experimental test at 50m.

Table 4.30 shows the statistics of the quantification of the refraction corrections as geodetic refraction coefficient values k by using the Kukkamakis approach and the corresponding results by using the local geodetic refraction coefficient. Again the amplitude of the values indicates that the two methods are in agreement while the local values are always slightly bigger.

	k Kukkamaki				k Local			
Model	**Min**	**Max**	**Mean**	**St. Dev.**	**Min**	**Max**	**Mean**	**St. Dev.**
Kukkamaki	-	-	-	-	-	-	-	-
Huggershoff	-1.53	-1.00	-1.32	±0.09	-1.19	-0.71	-0.98	±0.08
Reissmann1	-1.64	-1.08	-1.43	±0.09	-1.17	-0.69	-0.97	±0.09
Reissmann2	-3.92	-2.75	-3.21	±0.24	-3.78	-2.46	-2.96	±0.28
Heer	-1.38	-0.85	-1.17	±0.09	-1.03	-0.56	-0.84	±0.08

Table 4.30 The geodetic refraction coefficient statistics of the 4 temperature height models and the indoor experimental test at 50m.

The following figures 4.45 and 4.46 show the values of the geodetic refraction coefficient k respectively for the two methods. Again the differences of the two charts are intractable by using this visual examination.

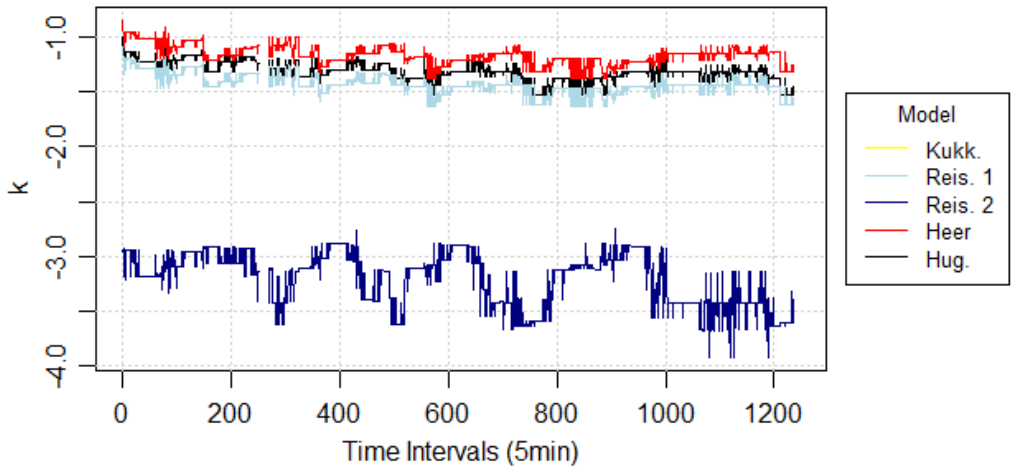

Figure 4.45 The geodetic refraction coefficient of the 4 temperature height models and the indoor experimental test at 50m by using the Kukkamaki's approach.

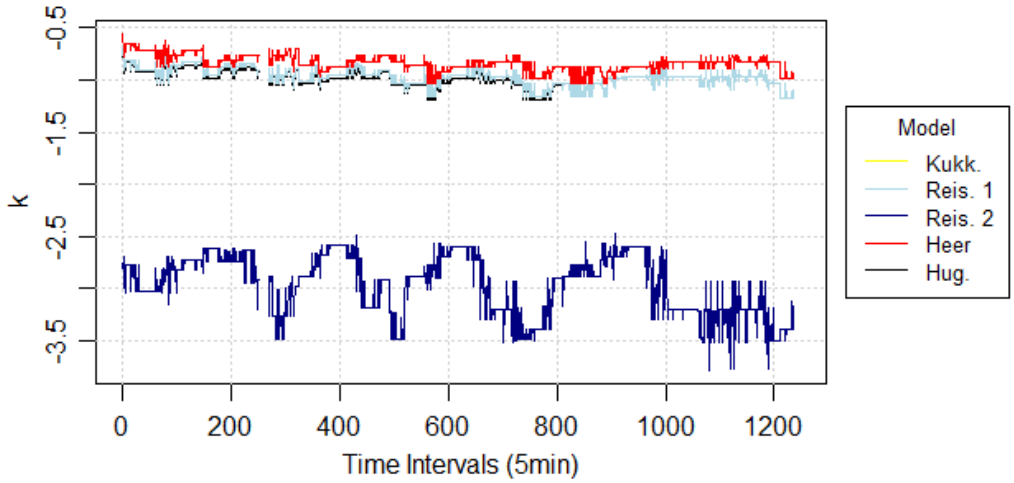

Figure 4.46 The geodetic refraction coefficient of the 4 temperature height models and the indoor experimental test at 50m by using the local geodetic refraction coefficient equation.

4.4.3 First Outdoor Experimental at 40m

Table 4.31 represents the refraction correction computations statistics of the five used models for the first outdoor experimental test at a sighting distance of 40m. At this case since the test was carried out outdoors the fluctuations of the measured parameters is bigger and more intense.

Model	Min	Max	Mean	St. Dev.
Kukkamaki	-5μm	517μm	154μm	±95μm
Huggershoff	-40μm	934μm	144μm	±116μm
Reissmann1	-270μm	3178μm	226μm	±319μm
Reissmann2	-197μm	643μm	-18μm	±98μm
Heer	-8μm	594μm	126μm	±84μm

Table 4.31 The refraction corrections statistics of the 5 temperature height models and the first outdoor experimental test at 40m.

Hence, the measured range is fruitless at this point and is more profitable to consider the mean value and the standard deviation instead. This fact happens either due to data trimming failure, or poor data fitting or overfitting.

Thus, the Reissmann1 model results are out of bounds and considered as outliers while Reissmann2 are completely wrong. Figure 4.47 aggregates these refraction corrections.

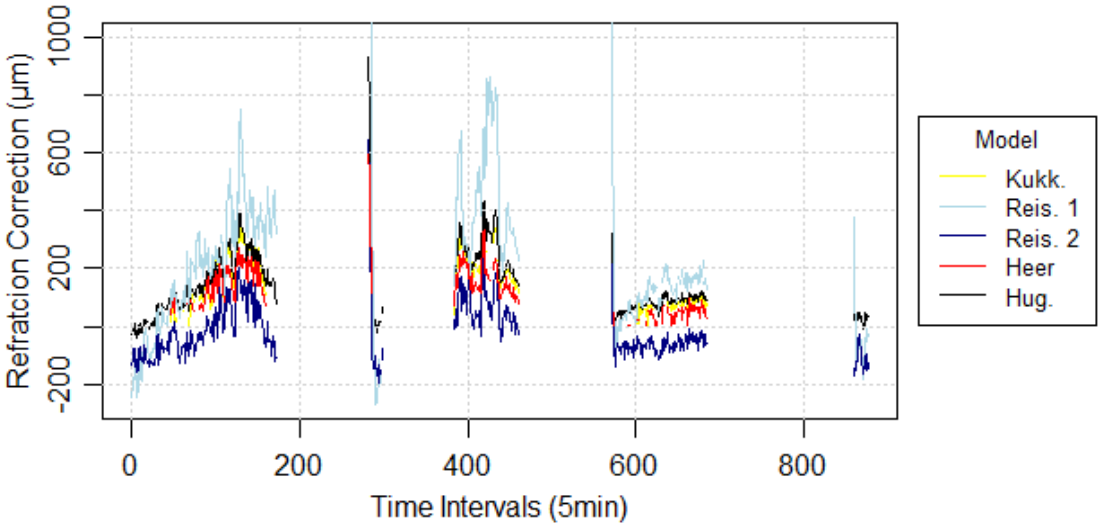

Figure 4.47 The refraction corrections of the 5 temperature height models and the first outdoor experimental test at 40m.

The following charts (figure 4.48) illustrate the initial height readings as grey line as long as the corrected height readings time series as red lines for the 5 used temperature height functions and the first outdoor experimental test at 40m. Again, the following charts do not seem to smooth out the height readings time series.

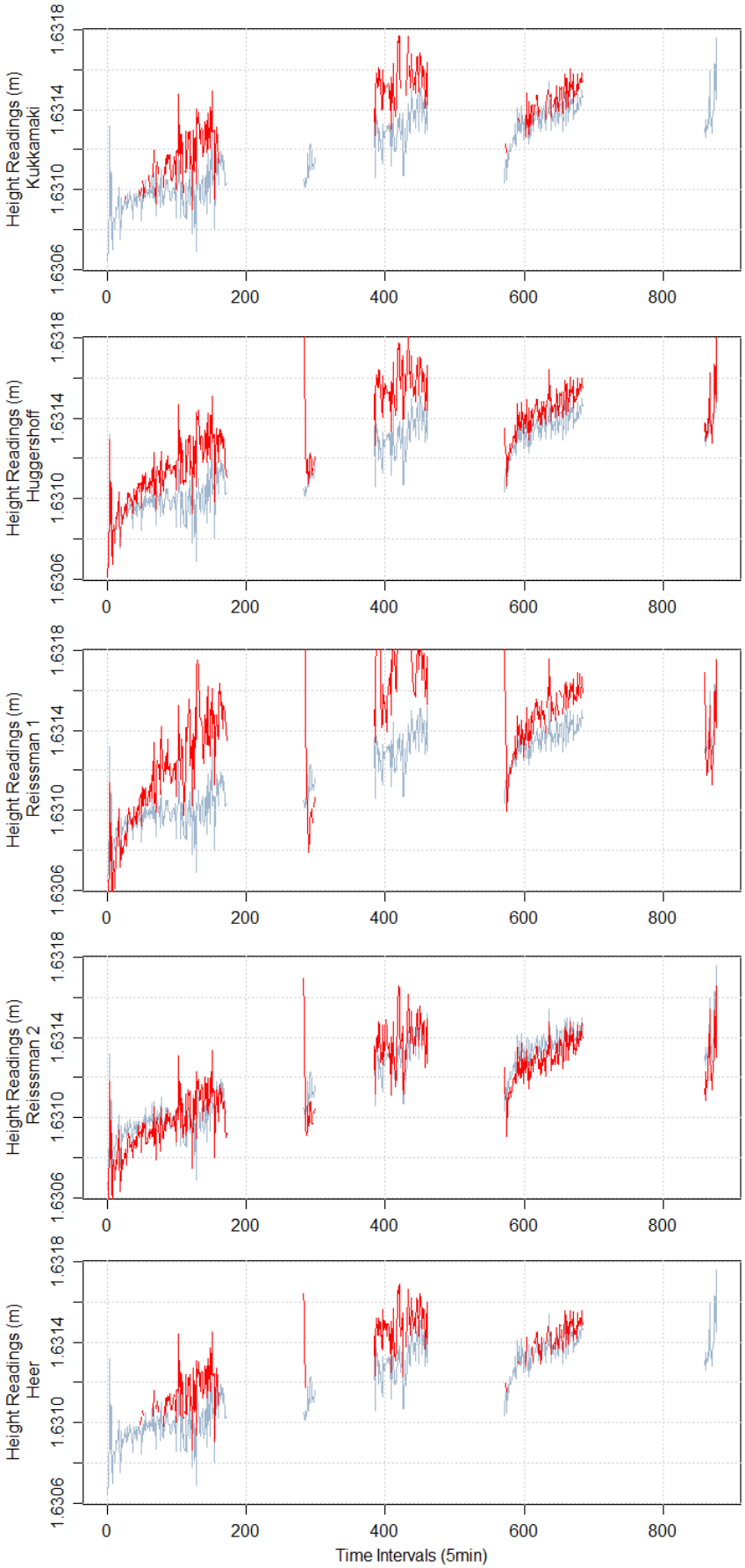

Figure 4.48 The initial (grey lines) and the corrected height readings time series (red lines) of the five temperature height functions and the first outdoor experimental test at 40m.

Table 4.32 demonstrates the statistics of the interpretation of the refraction corrections as geodetic refraction coefficient values k by using both the Kukkamaki's approach and the corresponding results by using the local geodetic refraction coefficient. Again the amplitude of the values indicates that the two methods are in agreement while the local values are always slightly bigger. What needs to be highlighted is that the coefficient values inherit the previously discussed failures and outliers.

	k Kukkamaki				k Local			
Model	**Min**	**Max**	**Mean**	**St. Dev.**	**Min**	**Max**	**Mean**	**St. Dev.**
Kukkamaki	-0.05	4.63	1.38	±0.85	0.17	4.86	1.60	±0.86
Huggershoff	-0.36	8.36	1.28	±1.03	-0.15	8.50	1.50	±1.03
Reissmann1	-2.41	28.43	2.02	±2.85	-2.23	28.77	2.24	±2.87
Reissmann2	-1.76	5.75	-0.16	±0.88	-1.57	6.14	0.05	±0.89
Heer	-0.07	5.32	1.13	±0.75	0.14	5.85	1.35	±0.78

Table 4.32 The geodetic refraction coefficient statistics of the 5 temperature height models and the first outdoor experimental test at 40m.

The following figures 4.49 and 4.50 illustrate the values of the geodetic refraction coefficient k respectively for the two methods and over time. Again the differences of the two charts are intractable by using this graphical examination.

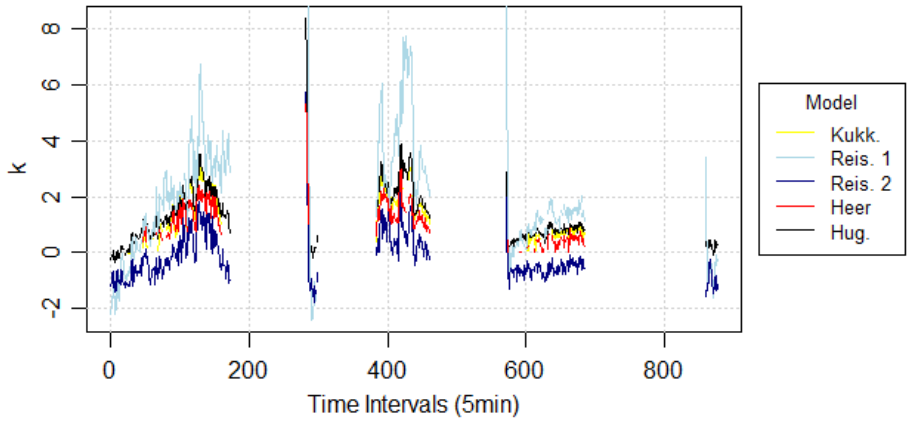

Figure 4.49 The geodetic refraction coefficient of the 5 temperature height models and the first outdoor experimental test at 40m by using the Kukkamaki's approach.

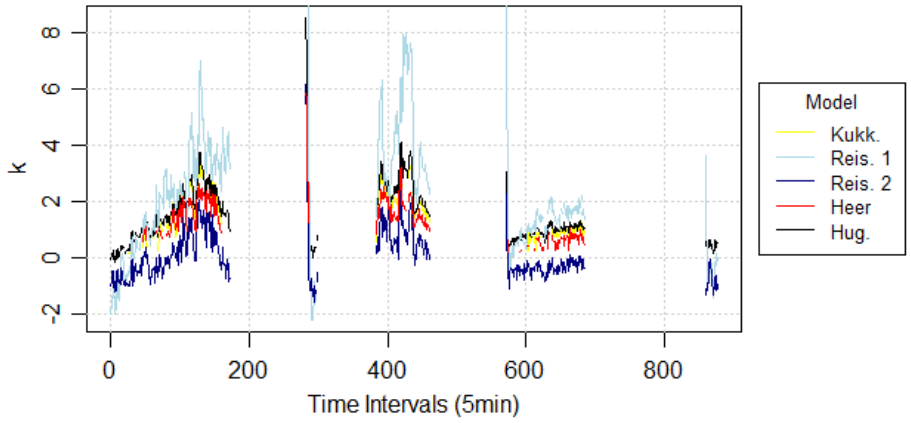

Figure 4.50 The geodetic refraction coefficient of the 5 temperature height models and the first outdoor experimental test at 40m by using the local geodetic refraction coefficient equation.

4.4.4 Second Outdoor Experimental at 40m (b)

Table 4.33 gathers the refraction correction computations statistics of the five used models for the second outdoor experimental test at a sighting distance of 40m. Once again, it is more profitable to consider the mean value and the standard deviation instead, due to the same blunders. Moreover Reissmann2 corrections are in majority wrong because of data overfitting.

Model	Min	Max	Mean	St. Dev.
Kukkamaki	-71μm	620μm	155μm	±103μm
Huggershoff	-67μm	721μm	118μm	±101μm
Reissmann1	-69μm	801μm	122μm	±106μm
Reissmann2	-205μm	702μm	-32μm	±87μm
Heer	-53μm	473μm	113μm	±83μm

Table 4.33 The refraction corrections statistics of the 5 temperature height models and the second outdoor experimental test at 40m.

Figure 4.51 illustrates the computed corrections of all selected height temperature models of the second outdoor experimental test. The positive conclusion that comes out of this graph is that the refraction corrections are decreasing (as does the temperature gradient) while the height readings are increasing. At the same time the spread and the amplitude among the readings and the corrections are in agreement.

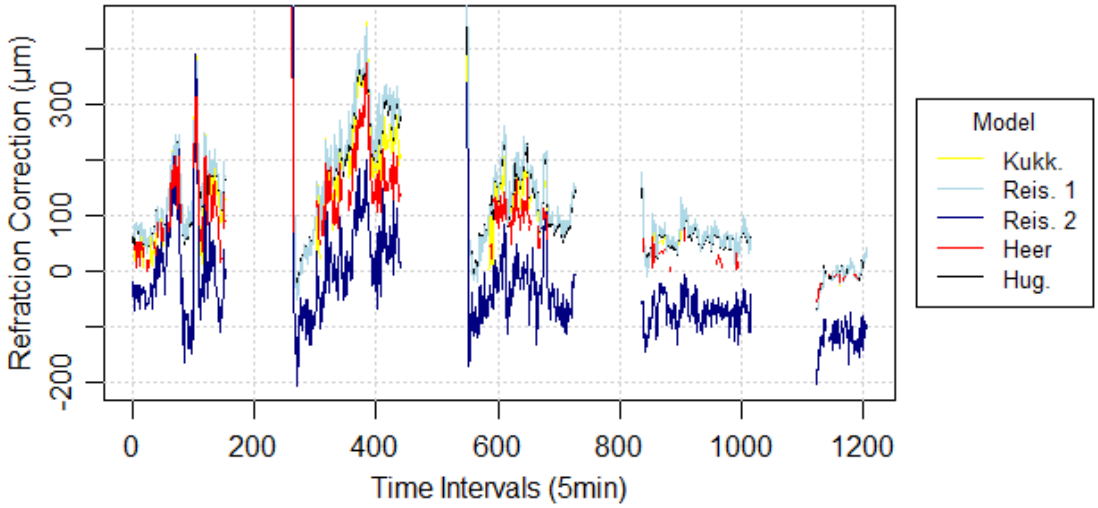

Figure 4.51 The refraction corrections of the 5 temperature height models and the second outdoor experimental test at 40m.

The charts of figure 4.52 show the initial height readings as grey line and the corrected height readings time series as red lines for the 5 used temperature height functions and the second outdoor experimental test at 40m. Again, the following charts do not contribute to height readings smoothing since the noise of the data is still a limiting factor.

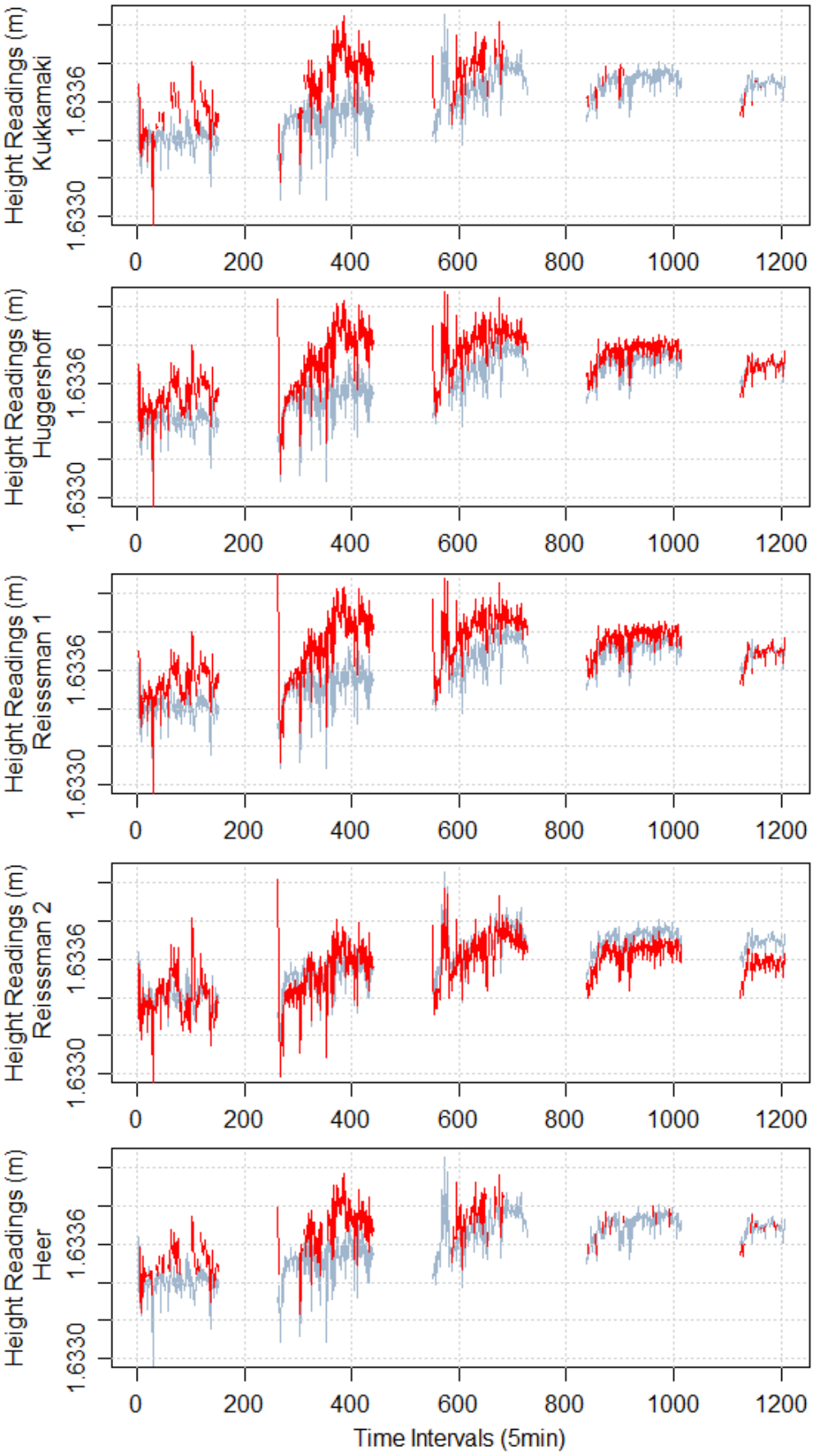

Figure 4.52 The initial (grey lines) and the corrected height readings time series (red lines) of the five temperature height functions and the second outdoor experimental test at 40m.

Table 4.32 demonstrates the statistics of the interpretation of the refraction corrections as geodetic refraction coefficient values k by using both the Kukkamaki's approach and the corresponding results by using the local geodetic refraction coefficient, while figures 4.53 and 4.54 illustrate these values.

Again the coefficient values indicate that the two methods are in agreement with a small shift, since the local geodetic refraction coefficient equation also encompasses the influence of the pressure gradient.

	k Kukkamaki				k Local			
Model	**Min**	**Max**	**Mean**	**St. Dev.**	**Min**	**Max**	**Mean**	**St. Dev.**
Kukkamaki	-0.63	5.48	1.37	±0.91	-0.42	5.73	1.59	±0.92
Huggershoff	-0.60	6.38	1.04	±0.89	-0.14	6.51	1.53	±0.88
Reissmann1	-0.62	7.08	1.08	±0.93	-0.41	7.54	1.30	±0.95
Reissmann2	-1.81	6.21	-0.28	±0.77	-1.65	6.66	-0.77	±0.78
Heer	-0.47	4.18	1.00	±0.73	-0.26	4.67	1.21	±0.74

Table 4.34 The geodetic refraction coefficient statistics of the 5 temperature height models and the second outdoor experimental test at 40m.

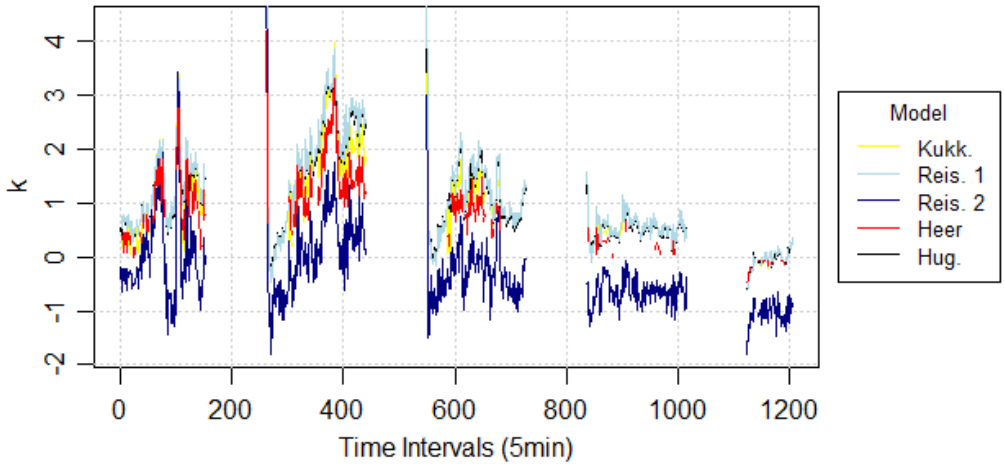

Figure 4.53 The geodetic refraction coefficient of the 5 temperature height models and the second outdoor experimental test at 40m by using the Kukkamaki's approach.

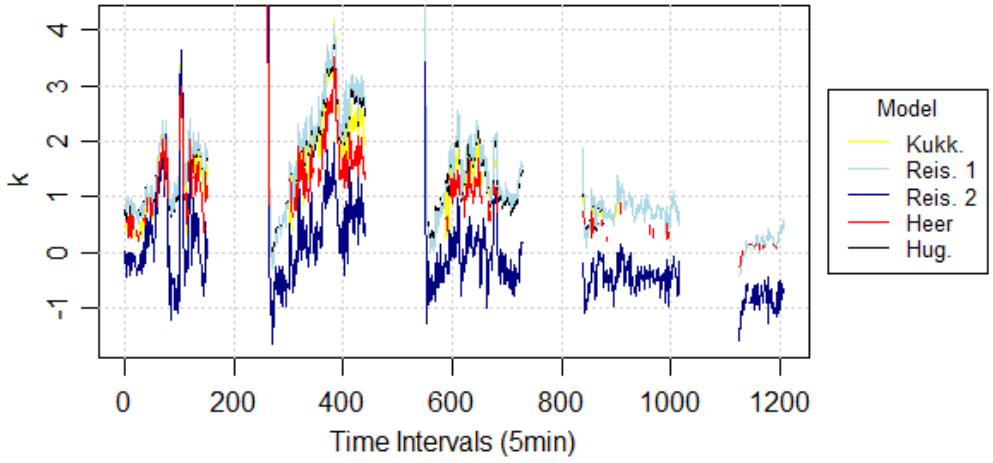

Figure 4.54 The geodetic refraction coefficient of the 5 temperature height models and the second outdoor experimental test at 40m by using the local geodetic refraction coefficient equation.

Figures 4.53 and 4.54 present the values of the geodetic refraction coefficient k respectively for the two methods and over time. Again the differences of the two charts cannot be distinguished graphically.

CHAPTER 5
CONCLUSIONS AND RECOMMENDATIONS

5.1. Conclusions

The need of high accuracy geodetic measurements is nowadays extended for the needs of dimensional metrology, monitoring, deformation and engineering surveying. In spite of the intense technological improvement, the accuracy of geodetic observations is still limited due to terrestrial refraction.

Thus, the aiming of this master thesis was to address an applicable method, in terms of instrumentation and computations, in order to overcome and treat the error of levelling refraction. Hence, both indoor and outdoor experimental tests were carried out, by acquiring repeatable short term height readings by using a stand-alone set up of a high accuracy digital level.

At the same time the direct measurement of the vertical temperature gradient, which is the main influential factor of refraction effects, was conducted by using air temperature sensors nodes mounted on discrete positions of the bar-coded invar staff. Also the air temperature sensors were calibrated by using a climate chamber.

Based on the previously discussed investigations, the following conclusions can be extracted:

- Initially, the data acquisition process is optimized since the air temperature sensor nodes can be controlled wirelessly and the digital level by using a serial online mode, with extreme reliability.
- The calibration of the air temperature sensors improves their measuring discretion ability since the measurements are converted to the same reference scale. The measuring accuracy and repeatability of the air temperature sensors were then considered at ±0.1°C.
- At the first indoor experimental test at a sighting distance of 25m, the measured parameters were completely stationary as the height readings density plot indicated one main value and the air temperature measurements of the sensors were illustrated by horizontal lines.
- The other three experimental tests had more intense fluctuations of the measured parameters and moderate positive linear correlations occurred between the temperature and the height readings time series.
- The temperature height functions seem to work properly when the temperature gradient takes the value of about $0.4°C \cdot m^{-1}$ except the model Reissmann1, like the first indoor experimental test. On all other cases, in which the temperature gradient was limited to values of $0.2°C \cdot m^{-1}$, meaning close to the measuring accuracy of the sensors, only Huggershoff's model managed to pass the statistical test at the majority of the measurements. Additionally, the other models failed to pass the test or fit the data while Reissmann2 model was

overfitting the data as it was expected since polynomials greater than second order fail to work properly.

- None of the computed height corrections manage to contribute to the smoothing of the height readings time series since there is a lot of noise in the measurements that is inherited to the corrections.
- The most promising and positive proof conclusion is referred to the second outdoor experimental test, where the refraction corrections are decreasing while the height readings are increasing with the corresponded spread.
- However all the refraction corrections computations signs and amplitudes were in line with the expected values from the theoretical overview and literature. Additionally the geodetic refraction coefficient k took accepted values from 0 to +2.4 in the outdoor tests and from -1.6 to +3.2 in the indoor tests.
- Lastly the values of the geodetic refraction coefficient k values that were computed with the Kukkamaki's approach and the local geodetic refraction coefficient seem to be in agreement. The slight deviation of about 0.2 justifies the fact that the local equation also encompasses the pressure gradient influence.

5.2. Recommendations

The following recommendations are made as regard to future studies of levelling refraction:

- Firstly a thorough uncertainty analysis has to be made in order assess the instrumentation measuring accuracy in order to succeed corresponding results.
- Then additional experimental tests have to be implemented taking into account the following terms:
    - the limitation of the air temperature measuring accuracy needs to be better than ±0.005°C and so the evaluation of the goodness of fit will be improved
    - the air temperature sensors vertical configuration has to be carried out in more horizontal segments of the sighting distance and not only at the staff, thus the fluctuations of the temperature gradient along the sighting line will be taken under consideration
    - if the above upgrades fail to improve the results then the assumptions of the method have to be reassessed
- Lastly the parallel combination of temperature gradient measurements, height readings and reciprocal and simultaneous zenith angle observations as long as with the heat flux calculations would be fruitful

REFERENCES

AHLBORN, (1999). Operating Instructions Data Logger ALMEMO 2290-8 V5. AHLBORN Mess- und Regelungstechnik GmbH. Holzkirchen.

Angus-Leppan, P. V. (1969). Surface effects on refraction in precise leveling. in REF-EDM Conference on Refraction Effects in Geodesy & Conference on Electronic Distance Measurement.(pp. 74–89). Univ. of N. S. W., Sydney, N. S. W., Australia.

Angus-Leppan, P. V. (1984). Refraction in geodetic levelling. In Geodetic Refraction (pp. 163-180). Springer, Berlin, Heidelberg.

Apodoulianakis, L. N. (2011). Investigation of the measurement's change (repeatability) of digital levels at different conditions. Diploma Thesis. Laboratory of General Geodesy. SRSE. NTUA. Athens. (in Greek)

Bahnert, G. (1972): Bestimmung und Verwendung vertikaler Temperaturgradienten. In: Vermessungstechnik, Vol. 5.

Bahnert, G. (1987). Zur Bestimmung lokaler Refraktionskoeffizienten. Vermessungstechnik, 35(1), 14-17.

Baselga, S., García-Asenjo, L., & Garrigues, P. (2013). Practical formulas for the refraction coefficient. Journal of Surveying Engineering, 140(2), 06014001.

Böckem, B., Flach, P., Weiss, A., & Hennes, M. (2000, September). Refraction influence analysis and investigations on automated elimination of refraction effects on geodetic measurements. In Paper to XVI IMEKO World Congress (pp. 25-28).

Bomford, G. (1980), Geodesy, 4th ed., Clarendon, Oxford, U.K.

Breznikar, A., & Aksamitauskas, Č. (2012). Atmospheric effects in geodetic levelling. Geodesy and Cartography, 38(4), 130-133.

Brocks, K. (1939). Vertikaler Temperaturgradient und terrestrische Refraktion, insbesondere im Hochgebirge. Veröff. d. Meteorol. Inst. d. Univ. Berlin.

Brocks, K. (1948). Über den täglichen und jährlichen Gang der Höhenabhängigkeit der Temperatur in den unteren 300 Metern der Atmosphäre und ihren Zusammenhang mit der Konvektion. Dt. Wetterdienst in der US-Zone.

Brocks, K. (1949). Die terrestrische Refraktion in polytropen Atmosphären. Deutsche Hydrografische Zeitschrift, 2(5), 199-211.

Brocks, K. (1950a). Die Lichtstrahlkrümmung in Bodennähe. Deutsche Hydrografische Zeitschrift, 3(3-4), 241-248.

Brocks, K. (1950b). Meteorologische Hilfsmittel für die geodätische Höhenmessung. Zeitschrift für Vermessungswesen,(3), 71-76.

Brunner, F. K. (1984). Modelling of atmospheric effects on terrestrial geodetic measurements. In Geodetic Refraction (pp. 143-162). Springer, Berlin, Heidelberg.

Brunner, F. K., & Angus-Leppan, P. V. (1976). On the significance of meteorological parameters for terrestrial refraction. Unisurv G, 25, 95-108.

Brunner, F. K., & Kukuvec, A. (2011). Utility of geodetic refraction. *Proc. INGEO, 2011*, 22-24.

Brunner, F., & Fraser, C. (1977). Application of the Atmospheric Turbulent Transfer Model (TTM) for the Reduction of Microwave FDM (Vol. No. 27). Unisurv G. Austral. J. Geodesy. Photogrammetry & Surveying.

Bureau International des Poids et Mesures (BIPM), (1990). Techniques for Approximating the International Temperature Scale of 1990.

Ciddor, P. E. (1996). Refractive index of air: new equations for the visible and near infrared. Applied optics, 35(9), 1566-1573.

Ciddor, P. E., & Hill, R. J. (1999). Refractive index of air. 2. Group index. Applied Optics, 38(9), 1663-1667.

Davis, (2018). Wireless Vantage Pro2 (6152, 6153) & Vantage Pro2 Plus (6162, 6163) Stations .Davis Instruments. Hayward. USA (https://www.davisnet.com).

Dodson, A. H., & Zaher, M. (1985). Refraction effects on vertical angle measurements. Survey Review, 28(217), 169-183.

Eschelbach, C. (2009). Refraktionskorrekturbestimmung durch Modellierung des Impuls- und Wärmeflusses in der Rauhigkeitsschicht. KIT Scientic Publishing.

European Association of National Metrology Institutes (EURAMET), (2011). Calibration of Thermocouples. Calibration Guide cg8. Version 2.1 .Braunschweig. Germany.

Flach, P. (2000). Analysis of refraction influences in geodesy using image processing and turbulence models (Doctoral dissertation, ETH Zurich).

Gaifillia, D. , Pagounis, V. , Tsakiri, M. , & Zacharis, V. (2016). Empirical Modelling of Refraction Error in Trigonometric Heighting Using Meteorological Parameters. Journal of Geosciences and Geomatics, 4(1), 8-14.

Georgakis, C., Santamouris, M., & Kaisarlis, G. (2010). The vertical stratification of air temperature in the center of Athens. Journal of Applied Meteorology and Climatology, 49(6), 1219-1232.

Giannakopoulos, L. (2007). Determination of the geodetic refraction coefficient k by using modern geodetic instrumentation Application: Likavittos-Kirou Pira. Diploma Thesis. Laboratory of General Geodesy. SRSE. NTUA. Athens. (in Greek)

Gottawald, R. (1985). Zur Genauigkeitssteigerung und Erstellung eines automatisierten Datenflusses beim trigonometrischen Nivellement mit kurzen Zielweiten (Vol. Nr. 37.). Aachen.

Heer, R. (1983). Application of different refraction models on measuring results of the levelling test loop Koblenz. In Contributions to the Workshop on Precise Leveling. Precise Leveling (pp. p251-281).

Heer, R., Niemeier, W., & Hannover, U. (1985). Theoretical models, practical experiments and the numerical evaluation of refraction effects in geodetic levelling. In Proceedings of the Third International Symposium on the North American Vertical Datum-NAVD Symposium'85 (pp. 321-342).

Hennes, M., Dönicke, R., & Christ, H. (1999). Zur Bestimmung der temperatur gradienteninduzierten Richtungsverschwenkung beim Tunnelvortrieb. VPK, 8/99, pp. 418-426.

Hirt, C., Guillaume, S., Wisbar, A., Bürki, B., & Sternberg, H. (2010). Monitoring of the refraction coefficient in the lower atmosphere using a controlled setup of simultaneous reciprocal vertical angle measurements. Journal of Geophysical Research: Atmospheres, 115(D21).

Hübner, E. (1977). Einfluss der terrestrischen Refraktion auf den Laserstrahl in bodennahen Luftschichten. Vermessungstechnik.–1977.–25 (10), 349-353.

Ingensand, H. (2008). Concepts and solutions to overcome the refraction problem in terrestrial precision measurement. Geodezija ir Kartografija, 34(2), 61-65.

International Electrotechnical Commission (IEC), (1995). Thermocouples, Part 1, Reference tables. EN IEC 60584-1. Geneva. Switzerland.

International Union of Geodesy and Geophysics (IUGG). (1999). Resolution 3 of the International Association of Geodesy. Comptes Rendus of the XXII General Assembly. (pp. 110-111). 19-30, July 1999. Birmingham.

Janes, H. W., Langley, R. B., & Newby, S. P. (1991). Analysis of tropospheric delay prediction models: comparisons with ray-tracing and implications for GPS relative positioning. Bulletin géodésique, 65(3), 151-161.

Jenne, D. E. (1957). Vertical temperature profiles in relation to other meteorological elements and to air pollution. Journal of the Air Pollution Control Association, 7(1), 31-35.

Joeckel, R., Stober, M., & Huep, W. (2008). Elektronische Entfernungs-und Richtungsmessung und ihre Integration in aktuelle Positionierungsverfahren, 5., neu bearbeitete und erweiterte Auflage.

Kabashi, I. (2003). Gleichzeitig-gegenseitige Zenitwinkelmessung über größere Entfernungen mit automatischen Zielsystemen. Ph. D. dissertation. 101 pp. Tech. Univ. Wien. Vienna.

Kahmen, H., & Faig, W. (1988). Surveying. Walter de Gruyter.

Kakkuri, J. (1984). About the future use of the Kukkamaki leveling refraction formula, in H. Pelzer (Ed.). Workshop Precise Levelling. Duemmlers Verlag, 235–241.

Katz, M. G., Schaps, D. M., & Shnider, S. (2013). Almost equal: The method of adequality from Diophantus to Fermat and beyond. Perspectives on Science, 21(3), 283-324.

Kharaghani, G. A. (1987). Propagation of refraction errors in trigonometric height traversing and geodetic leveling. Tech. Rep. 132. Dep. of Surv. Eng. Univ. of New Brunswick. Fredericton. New Brunswick. Canada.

Korritke, N. (1992). Horizontalrefraktion in langen Tunneln. XI. Internationaler Kurs für Ingenieurvermessung, 21, 26.

Kukkamaki T.J. (1938). Über die nivellitische Refraktion. Suomen geodeettinen laitos. Publications of Finnish Geodetic Institute. Helsinki. 25.

Kukkamaki T.J. (1939). Formeln und Tabel1en zur Berechnurg der nivellitischen Refraktion. Publications of Finnish Geodetic Institute. Helsinki. 27.

Lallemand, M. C. (1896). Note sur l'erreur de refraction dans le nivellment geometrique. Comptes Rendues des Seances de la Commission Permanente de L'association Geodesiques Internationale, Lausanne, 247-276.

Lambrou, E., Pantazis, G. (2010). Applied geodesy. Edition Ziti, Athens, Greece (in Greek)

Leica Geosystems, (2002). GSI ONLINE for Leica TPS and DNA. Leica Geosystems AG. Heerbrugg. Switzerland.

Leica Geosystems, (2006a). Leica DNA digital levels Advantages that move you ahead. Leica Geosystems AG. Heerbrugg. Switzerland.

Leica Geosystems, (2006b). Leica DNA03/DNA10 User Manual. Leica Geosystems AG. Heerbrugg. Switzerland.

Leica Geosystems, (2007). GPLE2N/GPLE3N GPCL2/GPCL3 User Manual. Leica Geosystems AG. Heerbrugg. Switzerland.

LORD MicroStrain, (2015a). LORD DATASHEET TC-Link 1CH-LXRS 1 channel Wireless Thermocouple Node. LORD Corporation MicroStrain Sensing Systems. Williston. USA.

LORD MicroStrain, (2015b). LORD USER MANUAL Node Commander Software Suite Wireless Sensor Network Data Acquistion and Utility Software. LORD Corporation MicroStrain Sensing Systems. Williston. USA.

Mavridis, L. N., & Papadimitriou, A. L. (1973). Study of terrestrial refraction in the area of Thessaloniki. Journal of Geophysical Research, 78(15), 2679-2684.

Mendes, V. B., & Pavlis, E. C. (2002, October). Atmospheric refraction at optical wavelengths: problems and solutions. In Proceedings of the 13th International Laser Ranging Workshop, Washington DC.

Molivas, Ch. (2007). Determination of the geodetic refraction coefficient k by using modern geodetic instrumentation Application: Labadario-Kirou Pira. Diploma Thesis. Laboratory of General Geodesy. SRSE. NTUA. Athens. (in Greek)

Moritz H. (1967). Application of the conformal theory of refraction. Osterr ZfV Sonderband 25:323-334.

Moritz, H. (1962). Zur Geometrie der Refraktion. Öst ZfV, 50, 3-13.

Moritz, H., & Hofmann-Wellenhof, B. (1993). Geometry, relativity, geodesy. Karlsruhe: Wichmann.

National Association of Testing Authorities (NATA), (2018). Temperature metrology. Specific Accreditation Criteria Calibration ISO/IEC 17025 Annex. NATA. Australia.

Nikolitsas, K. (2015). Development of laboratory methodologies for the calibration of digital geodetic instruments. Doctoral Thesis. Laboratory of General Geodesy. SRSE. NTUA. Athens. (in Greek)

Nikolitsas, K. (2018). Determination of the refraction corrections in precise levelling using the temperature gradient An application in the section 78 of the tunnel of LHC accelerator at CERN. Post-Doctoral Thesis. Laboratory of General Geodesy. SRSE. NTUA. CERN, Geneva. (under ellaboration)

Oke, T. R. (1981). Canyon geometry and the nocturnal urban heat island: comparison of scale model and field observations. International Journal of Climatology, 1(3), 237-254.

Pellegrinelli, A., Furini, A., Bonfé, M., & Russo, P. (2013). Motorised digital levels: development and applications. Survey Review, 45(330), 174-189.

Reissmann, G. (1954). Untersuchungen zur Ausschaltung des Einflusses der Vertikalrefraktion beim Präzisionsnivellement. Verlag Technik.

Reiterer, A. (2012). Modeling Atmospheric Refraction Influences by Optical Turbulences Using an Image-Assisted Total Station. Zeitschrift für Geodäsie, Geoinformation und Landmanagement (zfv), 137(3), 156-165.

Remmer, O. (1975). Levelling errors in statu nascendi. Geodætisk Institut. Meddelelse 51. Copenhagen.

Remmer, O. (1980a). Refraction in levelling. Geodætisk Institut. Meddelelse 54. Copenhagen.

Remmer, O. (1980b, May). Role and evaluation of refraction for the processing of levelling networks. In Proceedings NAD-Symposium, Ottawa (pp. 623-646).

Schofield, W., & Breach, M. (2007). Engineering surveying. 6th ed. CRC Press. Butterworth-Heinemann. Oxford. U. K.

Schuster, A. (1904). An introduction to the theory of optics. E. Arnold.

Shaw, R. H., & Smietana, P. J. (1983). Temperature stratification and refraction errors in geodetic leveling. Journal of Geophysical Research: Solid Earth, 88(B12), 10485-10494.

Sirůčková, H. (2016). Experimental levelling at the interface of optical environments. Acta Polytechnica 56(2):138–146. Department of Special Geodesy. Faculty of Civil Engineering Czech. Technical University in Prague.

Stober, M. (1995). Untersuchungen zum Refraktionseinfluss bei der trigonometrischen Höhenmessung auf dem grönländischen Inlandeis. Festschrift für Heinz Draheim, Eugen Kuntz und Hermann Mälzer, Geodätisches Institut der Universität Karlsruhe, 259-272. Karlsruhe. Germany.

Thomas, M. E., & Joseph, R. I. (1996). Astronomical refraction. Johns Hopkins apl technical digest, 17(3), 279.

Torge, W. (2001). Geodesy. Third completely revised and extended edition. Berlin. New York: Walter de Grayter.

Vötsch, (2016). Climate Test Chambers VC3 VCS3. Vötsch Industrietechnik GmbH Environmental Simulation. Balingen. Germany.

Wasmeier, P., & Foppe, K. (2006, October). A new CCD-based Technique for the Calibration of Leveling Rods. In Proceedings of the XXXIII International FIG Congress Commission (Vol. 5).

Weiss, A. (2002). Determination of thermal stratification and turbulence of the atmospheric surface layer over various types of terrain by optical scientillometry (Doctoral dissertation, ETH Zurich).

Wilhelm, W. (1994). Die Seitenrefraktion. Ein unbeliebtes Thema? Oder ein Thema nur für Insider. Vermessung, Photogrammetrie, Kulturtechnik, 2(94), 75-82.

Wunderlich, T. (1985). Die voraussetzungsfreie Bestimmung von Refraktionswinkeln. Institut für Landesvermessung und Ingenieurgeodäsie, Abteilung Ingenieurgeodäsie.

Young, A. T. (2006). Understanding astronomical refraction. The Observatory, 126, 82-115.